EMI Terminal Behavioral Modeling of SiC-based Power Converters

Bingyao Sun

Thesis submitted to the faculty of the Virginia Polytechnic Institute and State University in partial fulfillment of the requirements for the degree of

Master of Science
In
Electrical and Computer Engineering

Rolando Burgos, Chair
Dushan Boroyevich
Qiang Li

06/09/2015
Blacksburg, VA

Keywords: Silicon Carbide (SiC), Terminal model, Electro-magnetic Interference (EMI), Common Mode (CM), Differential Mode (DM)

© 2015, Bingyao Sun

EMI Terminal Behavioral Modeling of SiC-based Power Converters

Bingyao Sun

ABSTRACT

With GaN and SiC switching devices becoming more commercially available, higher switching frequency is being applied to achieve higher efficiency and power density in power converters. However, electro-magnetic interference (EMI) becomes a more severe problem as a result. In this thesis, the switching frequency effect on conducted EMI noise is assessed.

As EMI noise increases, the EMI filter plays a more important role in a power converter. As a result, an effective EMI modeling technique of the power converter system is required in order to find an optimized size and effective EMI filter.

The frequency-domain model is verified to be an efficient and easy model to explore the EMI noise generation and propagation in the system. Of the various models, the unterminated behavioral model can simultaneously predict CM input and output noise of an inverter, and the prediction falls in line with the measurement around 10 MHz or higher. The DM terminated behavioral model can predict the DM input or output noise of the motor drive higher than 20 MHz. These two models are easy to extract and have high prediction capabilities; this is verified on a 10 kHz-switching-frequency Si motor drive. It is worthwhile to explore the prediction capability of the two models when they are applied to a SiC-based power inverter with switching frequency ranges from 20 kHz to 70 kHz.

In this thesis, the CM unterminated behavioral model is first applied to the SiC power inverter, and results show that the model prediction capability is limited by the noise floor of the oscilloscope measurement. The proposed segmented-frequency-range measurement is developed and verified to be a good solution to the noise floor. With the improved impedance fixtures, the prediction from CM model matches the measurement to 30 MHz.

To predict the DM input and output noise of the SiC inverter, the DM terminated behavioral model can be used under the condition that the CM and DM noise are decoupled. With the system noise analysis, the DM output side is verified to be independent of the CM noise and input side. The DM terminated behavioral model is extracted at the inverter output and predicts the DM output noise up to 30 MHz after solving the noise floor and DM choke saturation problem.

At the DM input side, the CM and DM are seen to be coupled with each other. It is found experimentally that the mixture of the CM and DM noise results from the asymmetric impedance of the system. The mixed mode terminated behavioral model is proposed to predict the DM noise when a mixed CM effect exists. The model can capture the DM noise up to to 30 MHz when the impedance between the inverter to CM ground is not balanced. The issue often happens in extraction of the model impedance and is solved by the curving-fitting optimization described in the thesis.

This thesis ends with a summary of contributions, limitations, and some future research direction.

ACKNOWLEDGEMENTS

I would like to thank first and foremost my advisor, Dr. Rolando Burgos for this kind guidance and help during my two-year research. He could always point out my problems and lead me to the right direction. I appreciate his time on our personal or project weekly meeting, when he is so generous to give a lot of valuable suggestions and comments, and to teach me how to perform a nice research work. He is also gentle and friendly, and I can feel his support and trust always.

I would like to extend the thanks to my other committee members. Dr. Dushan Boroyevich always gives me professional comments, suggestions, and ideas during our discussion and meetings. He is also a humorous and enthusiastic person, who relieves my nervousness and brings me courage when I was in trouble. I would like to thank Dr. Qiang Li for his kindness and patience during my defense arrangement and evaluation of my research work.

This thesis would also not of been possible without the help of my fellow CPES colleagues. First I would like to thank Dr. Hemant Bishnoi. He taught me what is EMI modeling and how to perform a EMI test hand by hand. He followed and helped my work even when he left CPES. This research work is also significantly influenced by Dr. Xuning Zhang. When I have problems, he can always give me feasible advice and solutions. I would also thank Ting Ge, Bin Li, Shishuo, Zhao, Zichen, Miao, Ruiyang Qin, and Kai Li who not only give me a lot of professional suggestions, but also bring me a warm and happy memory during the two years in Blacksburg. I would appreciate Jun Wang, Qiong Wang, Chi Li, Fang Chen, Chao Fei, Alinaghi Marzoughi, Nidhi Haryani, Doubin Hou, Xiucheng Huang, Zhengyang Liu, Yuchen Yang, Han (Helen) Cui, Ming Lu, Lingxiao Xue, Yang Jiao, Shuilin Tian, Zhiyu Shen for their kind help. I would also like to thank other CPES staffs: David Gilham, Marianne Hawthorne, Linda Long, Trish Rose, and Teresa Shaw for their help with software and administrative affairs. In the end, I would also like to thank Regis Meuret and Houmam Moussa from Hispano-Suiza (SAFRAN Group) for their generous support to this research. It is honor of me to learn, talk and work with those talented and friendly people.

This research work has been funded by Hispano-Suiza (SAFRAN Group), France. I would like to thank them for their continued support and commitment towards research and education. All photos in the thesis are taken by author, 2015.

Last, but not the least, I will thank my dearest parents. They give me infinite love, support, patience and confidence even though they are thousands of miles away. Words cannot express how truly appreciative I am for all of their love and trust.

TABLE OF CONTENTS

Chapter 1 . Literature Review 1
1.1 Introduction 1
1.2 Lumped Modeling Approach 2
1.3 Behavioral Modeling Approach 3
1.4 Motivation 6
Chapter 2 . Assessment of Effect on EMI Emission from Different Switching Frequency and Different Switch Devices 7
2.1 Introduction 7
2.2 EMI emission comparison among different switching frequencies 8
2.2.1 Lumped circuit setup implemented in SABER® 8
2.2.2 EMI emission comparison among 20, 40, 70 and 100 kHz switching frequency in the simulated Si MOSFET inverter 14
2.2.3 EMI emission comparison among 20 and 70 kHz switching frequency in the simulated SiC JFET inverter 15
2.2.4 EMI emission comparison among 20 and 70 kHz switching frequency in experiment 20
2.3 EMI emission comparison among ideal switch, Si IGBT, Si MOSFET, and SiC JFET in simulation 22
2.4 Conclusion 24
Chapter 3 . CM Unterminated Behavioral Modeling for SiC Inverter 25
3.1 Introduction 25
3.2 UBM and Modeling procedure 28
3.2.1 Impedance identification 29
3.2.2 Noise source extraction 31
3.2.3 Optimized inverter impedance 31
3.3 Model extraction based on SiC MOSFET inverter with 20 kHz switching frequency 33
3.3.1 Inverter impedance measurement 34
3.3.2 Noise sources extraction in the choke case 35
3.3.3 Shunt case experiments 37
3.3.4 Optimization 39

3.4 Model extraction based on SiC MOSFET inverter with 70 kHz switching frequency 42
3.4.1 Model extraction in the 70 kHz switching frequency case 42
3.4.2 Evaluation of the EMI emission in different switching frequency based on UBM 45
3.5 Re-designed shunt impedance and improved measurement fixture 46
3.5.1 Improving the capacitance and the series resistance in the shunts 46
3.5.2 Measurement fixture improvement 48
3.5.3 Shunt PCB improvement 50
3.5.4 Improved shunt impedance and the updated UBM results 51
3.6 Noise floor issue and its developer 54
3.6.1 Origin of the noise floor issue and its effect on the UBM 54
3.6.2 Developer: segmented frequency range measurement with high-pass filter .. 57
3.7 Re-designed choke impedance in the high frequency 65
3.7.1 Choke design for higher impedance above 10 MHz 65
3.7.2 UBM re-extraction with the new choke impedances 68
3.8 Improved high frequency UBM 71
Chapter 4 . DM Terminated Behavioral Model of SiC Power Converter 72
4.1 Introduction 72
4.2 DM terminated behavioral modeling 72
4.3 System analysis of the CM and DM emission at input and output sides 74
4.3.1 Relationship between input and output noise in DM 75
4.3.2 Relationship between DM and CM noise at the output side 77
4.3.3 Relationship between DM and CM noise at the input side 79
4.4 DM output terminated behavioral model based on SiC inverter 86
4.4.1 DM output terminated behavioral model with 20 kHz switching frequency .. 86
4.4.2 DM output terminated behavioral model with 70 kHz switching frequency .. 90
4.5 Analysis of disturbance from CM noise source on DM noise in Mix Mode Model at the inverter input side 93
4.5.1 Extended modular terminated behavioral model 93
4.5.2 Mix mode terminated behavioral model 94
4.6 DM noise prediction with mixed CM noise 98

4.6.1 Mix mode terminated behavioral model extraction procedure 98
4.6.2 Mix mode model verification 99
4.7 Evaluation of the proposed mix-mode model 103
4.7.1 Issue: Unmeasurable parasitic capacitance from inverter to CM ground 103
4.7.2 Developer 103
4.7.3 DM noise prediction with unmeasurable parasitic capacitance 106
4.8 Conclusions 108
Chapter 5 . Summary and Future Work 109
5.1 Summary 109
5.2 Limitation 110
5.2.1 Local optimization results in the curve-fitting optimization 110
5.2.2 Insignificant DM effect on the CM noise 110
5.2.3 No effective CM models for asymmetric structure 110
5.3 Future work 110
5.3.1 Application of the mixed mode model in the asymmetric converter 111
5.3.2 EMI filter modeling 111
5.3.3 Effect of the switching speed on the EMI emission 111
References 112

INDEX OF FIGURES

Figure 1-1 Qian's Modular-terminal-behavioral (MTB) model from [49] under fair use 5
Figure 1-2 Andrew's Generalized Terminal Model (GTM) from [49] under fair use 5
Figure 2-1 General topology and setup diagram for motor drive 8
Figure 2-2 Conducted emission limits in DO-160E (Section 21) for L, M &H categories 8
Figure 2-3 Line impedance stabilization network 9
Figure 2-4 Per-unit length parasitic model of the Harness 10
Figure 2-5 Lumped circuit model of a single winding of the motor 10
Figure 2-6 SABER® model of three-phase motor drive with ideal switch 11
Figure 2-7 SABER® model of three-phase motor drive with SiC JFET 11
Figure 2-8 Inner model of SiC JFET in SABER® 12
Figure 2-9 SABER® model of three-phase motor drive with Si MOSFET 12
Figure 2-10 SABER® model of full motor drive system 13
Figure 2-11 Comparison among the CM input (upper) and the output (lower) current spectrums in the Si MOSFET inverter setup with 20 k, 40 k, 70 k and 100 kHz switching frequency 14
Figure 2-12 Comparison among the DM input (upper) and the output (lower) current spectrums in the Si MOSFET inverter setup with 20 k, 40 k, 70 k and 100 kHz switching frequency 15
Figure 2-13 Comparison among the CM input (upper) and the output (lower) current spectrums in the SiC JFET inverter setup with 20 k and 70 k Hz switching frequency 16
Figure 2-14 Comparison among the DM input (upper) and the output (lower) current spectrums in the SiC JFET inverter setup with 20 k and 70 k Hz switching frequency 17
Figure 2-15 Three-phase SiC MOSFET inverter setup schematic diagram 17
Figure 2-16 SiC MOSFET inverter setup 18
Figure 2-17 RL load 19
Figure 2-18 Probe placement in CM input (left)/ output (right) current measurement 20
Figure 2-19 Probe placement in DM input (left)/ output (right) current measurement 20
Figure 2-20 Comparison among the CM input (upper) and the output (lower) current spectrums in the SiC MOSFET inverter experimental setup with 20 k and 70 k Hz switching frequency 21

Figure 2-21 Comparison among the DM input (upper) and the output (lower) current spectrums in the SiC MOSFET inverter experimental setup with 20 k and 70 k Hz switching frequency 21
Figure 2-22 SABER® model of three-phase motor drive with Si IGBT 22
Figure 2-23 Comparison of the input (upper) and output (lower) CM emission with different switching devices. 23
Figure 2-24 Comparison of the input (upper) and output (lower) DM emission with different switching devices. 24
Figure 3-1 Motor drive set-up for unterminated CM model extraction 26
Figure 3-2 Comparison of measured and predicted CM currents for CM-DM filter inserted at the input side of the motor drive 26
Figure 3-3 Comparison of measured and predicted CM currents for DM EMI filter inserted in the output side of the motor-drive 27
Figure 3-4 General setup for an inverter system with CM ground 28
Figure 3-5 Unterminated behavioral model to be extracted 29
Figure 3-6 Equivalent unterminated behavioral model 29
Figure 3-7 CM propagation in the inverter 30
Figure 3-8 Equivalent CM inverter impedance 30
Figure 3-9 Inverter setup with CM chokes 31
Figure 3-10 Inverter setup with CM shunts 32
Figure 3-11 SiC inverter experimental setup 33
Figure 3-12 Probe placement in CM noise measurements 34
Figure 3-13 Impedance measurement method 34
Figure 3-14 Inverter impedance measurements 35
Figure 3-15 The input impedance and output impedance measurements with the inverter impedances 35
Figure 3-16 CM chokes 36
Figure 3-17 CM choke case input and output impedance with the inverter impedances 36
Figure 3-18 CM current spectrum in the 20kHz choke case Figure 3-19 Noise sources extracted in 20 kHz case 37
Figure 3-20 Comparison between the measurements and predictions for the validation case 37

Figure 3-21 Input shunt (left) and output shunt (right) impedance parameters and topologies ... 38
Figure 3-22 Total input and output impedances in the shunt case ... 38
Figure 3-23 Comparison between the measurements and predictions for the shunt case ... 39
Figure 3-24 Diagram for the optimization procedures ... 39
Figure 3-25 Comparison of the measured and optimized impedance in 20 kHz case ... 40
Figure 3-26 Comparison between the measurements and the predictions with the optimized inverter impedance in 20 kHz shunt case ... 41
Figure 3-27 Comparison between the measurements and the predictions with the optimized inverter impedance in the 20 kHz validation case ... 41
Figure 3-28 CM current spectrum in the 70 kHz choke case Figure 3-29 Noise sources extracted in 70 kHz case ... 43
Figure 3-30 Comparison between the measurements and the predictions with the measured inverter impedance in 70 kHz shunt case ... 43
Figure 3-31 Comparison between the measurements and the predictions with the optimized inverter impedance in 70 kHz shunt case ... 44
Figure 3-32 Comparison of the measured and optimized impedance in 70 kHz case ... 44
Figure 3-33 Comparison between the measurements and the ... 44
Figure 3-34 Z-matrix result after model extraction of 20 kHz and 70 kHz switching frequency cases. ... 45
Figure 3-35 Noise source results after model extraction of 20 kHz and 70 kHz switching frequency cases. ... 46
Figure 3-36 Output shunt impedances for the different output shunt topologies ... 47
Figure 3-37 Input shunt impedances for the different input shunt topologies ... 48
Figure 3-38 Input shunt measurement fixture schematic diagram ... 49
Figure 3-39 Input shunt measurement fixture ... 49
Figure 3-40 Banana conducting wire impedance ... 49
Figure 3-41 Designed short-circuit fixture ... 50
Figure 3-42 Designed short-circuit fixture impedance ... 50
Figure 3-43 Detailed input shunt PCB connection ... 50
Figure 3-44 Separation of the input shunt in one branch ... 51
Figure 3-45 Comparison between the original and new shunt impedance measurements ... 52

Figure 3-46 Comparison between the measurements and predictions for the 20 kHz shunt case with clarified shunt impedances 52
Figure 3-47 Comparison between the measurements and predictions after optimization for the 20 kHz shunt case with clarified shunt impedances 53
Figure 3-48 Comparison between the measurements and predictions for the 20 kHz validation case with clarified shunt impedances 53
Figure 3-49 Comparison between the measurements and predictions for the 70 kHz validation case with clarified shunt impedances 54
Figure 3-50 RTO 1014 effective bits with input frequency [48] 55
Figure 3-51 Vertical system noise floor of RTO oscilloscope 55
Figure 3-52 Comparison the spectrum measurements with different vertical scales on the same signal 56
Figure 3-53 Comparison of CM current spectrums in 20 kHz and 70 kHz shunt case 56
Figure 3-54 Topologies and parameters of 5 MHz (left) and 10 MHz (right) high-pass filter..... 57
Figure 3-55 Fabricated filters of 5 MHz (left) and 10 MHz (right) high-pass filter..... 57
Figure 3-56 Measured transfer gain for the high-pass filters..... 58
Figure 3-57 Comparison among the spectrum without filter, with 5 MHz and 10 MHz high-pass filter in the 20 kHz shunt case 59
Figure 3-58 Comparison among the spectrum without filter, with 5 MHz and 10 MHz high-pass filter in the 70 kHz shunt case 59
Figure 3-59 The connected spectrum based on the spectrum without filter, with 5 MHz and 10 MHz high-pass filter in the 20 kHz shunt case..... 62
Figure 3-60 The connected spectrum based on the spectrum without filter, with 5 MHz and 10 MHz high-pass filter in the 20 kHz validation case..... 62
Figure 3-61 Comparison between the measurements and predictions for the 20 kHz optimized shunt case with the connected spectrum 63
Figure 3-62 Comparison between the measurements and predictions for the 20 kHz validation case with the connected spectrum..... 63
Figure 3-63 The connected spectrum based on the spectrum without filter, with 5 MHz and 10 MHz high-pass filter in the 70 kHz shunt case..... 64

Figure 3-64 Comparison between the measurements and predictions for the 70 kHz optimized shunt case with the connected spectrum 64
Figure 3-65 Comparison between the measurements and predictions for the 70 kHz validation case with the connected spectrum..... 65
Figure 3-66 CM input chokes and their impedances-frequency curves 66
Figure 3-67 Comparison of the input impedance in the choke case between the original and new design 67
Figure 3-68 CM output chokes and their impedances-frequency curves 67
Figure 3-69 Comparison of the output impedance in the choke case between the original and new design 68
Figure 3-70 Choke case input and output impedances compared with the inverter impedances and the shunt case impedances after all improvements 69
Figure 3-71 Comparison between the measurements and predictions for the 20 kHz validation case with improved choke and shunt case impedances and segmented-frequency spectrums 70
Figure 3-72 Comparison between the measurements and predictions for the 70 kHz validation case with improved choke and shunt case impedances and segmented-frequency spectrums 70
Figure 4-1 DM noise models for a three-phase inverter 73
Figure 4-2 Choke-condition for input side DM model extraction 73
Figure 4-3 DM current measurement fixture 74
Figure 4-4 Measurement of DM currents (a) input side (b) output side 74
Figure 4-5 Relationship among the four sub-systems where CM input and output are coupled.. 75
Figure 4-6 Comparison of the DM input (upper) and output (lower) noise spectrum between the Case 1 and Case 2 in Table 4-1..... 76
Figure 4-7 Comparison of the DM input (upper) and output (lower) noise spectrum between Case 2 and Case 3 in Table 4-1 77
Figure 4-8 Relationship among the four sub-systems where CM input and output are coupled, DM input and output are decoupled 77
Figure 4-9 Comparison of the DM output noise spectrum between Case 1 and Case 2 in Table 4-2 78

Figure 4-10 Comparison of the CM output noise spectrum between Case 2 and Case 3 in Table 4-2 78
Figure 4-11 Relationship among the four sub-systems where output CM and DM are decoupled 79
Figure 4-12 Sub-system setting to find the relationship between DM and CM noise at the input side corresponding to Table 4-3..... 80
Figure 4-13 Comparison of the CM input noise spectrum among the four cases in Table 4-3.... 81
Figure 4-14 Comparison of the DM input impedances among the four cases in Table 4-3..... 81
Figure 4-15 Comparison of the DM input noise spectrum among the four cases in Table 4-3.... 82
Figure 4-16 Comparison of the equivalent DM input noise sources among the four cases in Table 4-3 83
Figure 4-17 Sub-system setting to find the relationship between DM and CM noise at the input side corresponding to Table 4-4..... 84
Figure 4-18 Comparison of the CM input noise spectrum among the four cases in Table 4-4.... 84
Figure 4-19 Comparison of the DM input noise spectrum among the four cases in Table 4-3.... 85
Figure 4-20 Comparison of the equivalent DM input noise sources among the four cases in Table 4-3 85
Figure 4-21 Final relationship among the four sub-systems..... 86
Figure 4-22 Inverter with DM chokes 87
Figure 4-23 DM output terminated behavioral model 87
Figure 4-24 Comparison between the output impedance (green) and the output inverter impedance (red)..... 87
Figure 4-25 Comparison among the DM output noise spectrum without filter, with 5 MHz and 10 MHz high-pass filter in the 20 kHz validation case..... 88
Figure 4-26 The connected segmented-frequency DM output spectrum based on the spectrum without filter, with 5 MHz and 10 MHz high-pass filter in the 20 kHz validation case 89
Figure 4-27 Comparison between the measurements and predictions for the 20 kHz validation case for DM output validation case 89
Figure 4-28 Saturated (left) and unsaturated (right) DM output chokes 90
Figure 4-29 Comparison between the measurements and predictions for the 20 kHz validation case for DM output validation case when the DM chokes are saturated..... 90

Figure 4-30 Comparison among the DM output noise spectrum without filter, with 5 MHz and 10 MHz high-pass filter in the 70 kHz validation case 91
Figure 4-31 The connected segmented-frequency DM output spectrum based on the spectrum without filter, with 5 MHz and 10 MHz high-pass filter in the 70 kHz validation case 91
Figure 4-32 Comparison between the measurements and predictions for the 70 kHz validation case for DM output validation case 92
Figure 4-33 Extended modular terminated behavioral model for the inverter 93
Figure 4-34 Mix-mode terminated behavioral model 94
Figure 4-35 Mix-mode terminated behavioral model with CM and DM chokes 95
Figure 4-36 Input CM choke impedance model 95
Figure 4-37 Input DM choke impedance model 96
Figure 4-38 DM spectrum in cases with and without CM choke (a): balanced impedances, (b): unbalanced impedances 97
Figure 4-39 Balanced Case: Equivalent noise source extraction in the mix mode model with extra capacitor from the inverter to CM ground 99
Figure 4-40 Extracted noise sources of the mix mode model 100
Figure 4-41 Impedance measurement in MM model 100
Figure 4-42 Impedance measurement result in MM model with Cpg = 0.47uF, Cng = 2uF 101
Figure 4-43 Diagram of the new unbalanced inverter with CM choke with Cpg = 0.47uF, Cng = 2uF 101
Figure 4-44 Comparison between the measurement of the case in Figure 4-43 and its prediction in MM model 102
Figure 4-45 Diagram of the new unbalanced inverter with DM choke with Cpg = 0.47uF, Cng = 2uF 102
Figure 4-46 Comparison between the measurement of the case in Figure 4-45 and its prediction in MM model 102
Figure 4-47 Diagram of the new unbalanced inverter with CM and DM choke with Cpg = 0.47uF, Cng = 2uF 103
Figure 4-48 Comparison between the measurement of the case in Figure 4-47 and its prediction in MM model 103

Figure 4-49 Diagram of the new unbalanced inverter without CM or DM choke with Cpg = 0.47uF, Cng = 2uF 104
Figure 4-50 The comparison between the optimized Zpg , Zng and the measurements 105
Figure 4-51 Comparison between the measurement of the case in Figure 4-43 and its prediction in MM model with the optimized Z_{pg} and Z_{ng}..... 105
Figure 4-52 Comparison between the measurement of the case in Figure 4-45 and its prediction in MM model with the optimized Z_{pg} and Z_{ng} 105
Figure 4-53 Comparison between the measurement of the case in Figure 4-47 and its prediction in MM model with the optimized Z_{pg} and Z_{ng} 106
Figure 4-54 Comparison between the initial value and optimized results of C_{pg} and C_{ng}..... 107
Figure 4-55 Comparison between the measurement and the prediction of the case without chokes in the original SiC inverter setup 107
Figure 4-56 Comparison between the measurement and the prediction of the case with CM and DM chokes in the original SiC inverter setup..... 108
Figure 4-57 Comparison between the measurement and the prediction of the case with DM chokes in the original SiC inverter setup 108

INDEX OF TABLES

Table 2-1 The differences between the ideal switch, Si IGBT, Si MOSFET, and SiC JFET in the simulation 22
Table 3-1 SiC inverter setup configuration for 20 kHz switching frequency 33
Table 3-2 The oscilloscope configuration 34
Table 3-3 SiC inverter setup configuration for 70 kHz switching frequency 42
Table 3-4 Different output shunt topologies with different capacitances 47
Table 3-5 Different input shunt topologies with different resistance 48
Table 3-6 Comparison of the measurement for different parts of the input shunt in one branch . 51
Table 3-7 Design characteristics of the high-pass filter 58
Table 3-8 Vertical scale in the oscilloscope during different experiments 60
Table 4-1 Sub-system setting to find the relationship between input and output noise in DM 76
Table 4-2 Sub-system setting to find the relationship between DM and CM noise at the output side 78
Table 4-3 Sub-system setting to find the relationship between DM and CM noise at the input side 79
Table 4-4 Sub-system setting to find the relationship between DM and CM noise at the output side in second experiments 83

Chapter 1 . Literature Review

1.1 Introduction

Silicon carbide (SiC) switching power devices, in conjunction with SiC diodes for high voltage, have currently become more commercially utilized thanks to their distinct advantages, which include a higher switching speed and lower switching losses, especially in comparison with silicon (Si) insulated gate bipolar transistors (IGBTs). With SiC devices, a higher switching frequency can be applied in the power converter to achieve more complex inverter architectures, more precise control, and higher density integrated power converters. However, the electromagnetic interference (EMI) generation tends to have increasingly negative effects on the operation of the inverter-fed electrical machine systems as the switching frequency increases. As a result, it is essential to analyze the EMI noise propagation path and noise distribution in the system, and design EMI filters to attenuate and contain EMI noise.

According to existing literature, there are several modeling methods used to imitate the EMI behavior of the power converter system. These methods include lumped circuits and frequency-domain models. The lumped models, implemented in simulation software, can generally give an accurate prediction of EMI noise up to 2 MHz. However, in order to extract the model, all the parasitic parameters in the setup must be determined, including detailed switching device models. Adding to the difficulty in the model extraction, the lumped model requires lengthy simulation software run time, which may also not converge in some cases. In order to avoid extraction issues in the lumped model, the behavioral model is proposed to provide a faster extraction processes and a comparable prediction capacity. The behavioral model in is a 'black box' modeling technique, requiring no detail in the converter. The model will use the noise sources in the frequency domain to simulate the switching parts and use measured impedances to conclude the noise propagation path. The conducted EMI noise can be predicted by the calculation within the equivalent noise sources and the impedances in the propagation path. Most of the existing work on the behavioral model focuses on the EMI noise prediction at the input side. With the models, an input filter can be designed to reduce the EMI noise below some EMI standards; the output sides are usually ignored. Note that some EMI standards, like DO-160, have a requirement for the conducted EMI noise at all the bundles and cables in the system. Take, for example, the application of a motor drive, where there needs to be an EMI filter between the motor drive and the motor, which the terminated model cannot address.

The unterminated behavioral model (UBM) is proposed in [47] to assess EMI emission at both the input and output sides simultaneously in frequency domain. Therefore, the EMI filter at the input and output sides can be designed by the UBM in one step. In [47], the UBM exhibits an accurate match between the model prediction with the experimental CM noise measurement to 20 MHz at the input and output sides. The unterminated behavioral model will be explained in detail in Chapter 2.

1.2 Lumped Modeling Approach

The detailed lumped circuit modeling approach is based on the physics of the circuit and is the classical way to model any electronic circuit. The interconnects, such as wires and printed circuit board (PCB) traces, are modeled using passive RLC equivalents. Other passive components like resistors, capacitors and inductors can be directly measured for their impedance using an impedance analyzer. The equivalent circuit models for the PCBs are usually extracted by electromagnetic numerical tools like Q3D®, and finite element method (FEM) tools like Ansoft® Maxwell. Other tools based on partial element equivalent circuit (PEEC) like InCa® can also be used in cases where RL equivalents are sufficient to model the interconnects [15]. The switches in power converters are modeled using semiconductor device models. These device models are non-linear and are based on higher order differential equations.

For simple converters, such models may be suitable [1] and could provide the most versatile solutions for EMI predictions. The main benefits of lumped circuit models are adaptability and scalability, as everything is based on physics. The gate drive, control, power stage etc. can be modeled separately and then included in the final time domain simulation model of the power converter. Parametric analysis is very easy, as the effects of using different devices or components can be easily evaluated by simply replacing their models in the simulation with new ones.

The lumped circuit model, however, gets very complex with the increase in number of semiconductor devices and the highest frequency of interest. Even with all the details, the model may not work, as the simulator can have convergence issues. The accuracy of such models for complicated topologies has been found to be good only up to around 10 MHz [2, 3]. Thus, in theory, detailed lumped circuit models provide the most versatile solution to EMI modeling. But in practice, their use is limited. The development time is long and requires a great deal of experience. In addition, the device models themselves may not be easily available. Sometimes manufactures provide them, but they may be encrypted or have to be otherwise developed separately.

In order to simplify the models' extraction processes and increase model robustness, engineers started using reduced order models. In such models, the devices are replaced by voltage or current sources. Since the devices are used as switches, the voltage across them has an approximately squared shape. However, it has been shown that [4] such an approximation is not accurate and finite rise/fall time must be included for better representation of the switched voltage (or current) [5, 6, 7, 8, 9]. The robustness of such models has been demonstrated in handling complex systems [10, 11, 12, 13]. However, results have shown that the accuracy is only good up to several MHz. In [4] it was shown that approximation of the voltage (or current) switching characteristics with a trapezoidal waveform might not be very accurate either. Attempts have been made to use piece wise linear approximation of the voltage and current though the devices [14]. However, this kind of modeling then becomes specific to the device in use, and accuracy was not shown to be any better than the previous models. Simplified models of IGBT for EMI analysis have also been developed in [15, 16]. Here the IGBT is modeled with an ideal switch, an ON resistance, and a

few capacitances. The accuracy of results was found to be good up to only several MHz, most likely because of the limitations of other lumped circuit models that were used to model the system.

The problem of accurately reproducing the switching slope (of voltage and/or current) can be solved by directly measuring the voltage across the switches and then representing them as noise sources in the EMI model [17, 18, 19]. This method has been shown to be more accurate than assuming the switched voltages to have a trapezoidal state [18, 19]. These methods do not remove the burden of extracting the complete lumped circuit model of the converter, and their advantage lies in simplifying the complexity of semiconductor device models only.

1.3 Behavioral Modeling Approach

The discussion of lumped circuit models points to an important limitation of the technique itself. It is not suitable for doing system level EMI simulations. Simulating several converters with detailed lumped circuit equivalents would require large computational resources and time, not to mention that the chances of convergence are severely diminished. Moreover, in design of power distribution network inside aircrafts, power converters supplied by several different manufacturers require integration. These manufactures seldom provide any internal information about their products, as it is proprietary. In such cases, the lumped circuit modeling technique cannot be used, as no details of the layout and devices are available. In order to tackle this dual problem of system level EMI simulations and lack of layout information, researchers started to develop black-box modeling techniques, also called behavioral modeling techniques.

These techniques model the power converters using a one-port or a two-port network with independent sources [20,21]. A one-port network with an independent source is nothing but a Thevenin (or Norton) equivalent of the circuit. Extension of the Thevenin theorem to multi-terminal networks is also possible [22, 23]. The impedances of multi-terminal Thevenin-equivalents can be easily represented as multi-port networks with independent sources, so there is no fundamental difference between the two. In time domain, the existence of Thevenin (or Norton) equivalents is not restricted by linearity or time-variance [24, 25]. That is, the Thevenin models exist even for the non-linear and time-variant circuit. However, they are restricted in the frequency domain by linearity and time-variance. This is because the 'impedances' are defined only for linear and time-invariant circuits. Thus, Thevenin (or Norton) models in frequency domain require the circuit to be approximately linear and time-invariant.

In [26], a simplified two-terminal model is developed for a motor-drive system using Thevenin-equivalent. Both the noise source (Thevenin source) and the noise impedance (Thevenin impendence) were measured directly. The accuracy was not good, mostly due to the inaccuracy of the noise source itself. The DM noise source was directly measured across the DC-link capacitor and the CM noise was measured by disconnecting the ground wire. In [27, 28], the CM noise in the motor-drive is directly measured and modeled as voltage sources. The parts of the motor-drive that are passive, such as cable (harnesses), motor, line impedance stabilization network (LISN), etc. are modeled as two-port networks. The main limitation of this method is the over-simplification of the motor-drive model. Only one noise source is used to describe the CM

equivalent of the motor-drive, and the impedance of the motor-drive is modeled with only one capacitor to ground. This leads to inaccuracy beyond a few MHz; however, the technique is fairly easy to implement and the model can even be run in a math tool, as the system is modeled with two-port networks, which facilitates calculations by using only the network equations.

Another class of behavior modeling technique indirectly calculates the noise source and noise impedances by using two or more conditions and then simultaneously solving network equations. This technique uses more generic models of noise sources rather than assuming a particular topology as the given topology. Thus, the models are more complete in the sense of minimum required number of voltage/current sources and the number of impedances necessary for a complete description of a multi-terminal network [22]. The earliest attempt of EMI modeling of power converters using this technique was seen in [29]. The technique, however, had limitations regarding the identification of noise-source impedance. A resonant method was used to estimate the input impedance of the converter in which a known external impedance was tuned to resonate with the input impedance of the converter. This technique is not easy to use, as tuning impedance is not easy to begin with, and at higher frequency the input impedance may have several resonances within the same decade, so extremely precise tuning is needed.

Qian Liu et. al published several papers on extraction of a three-terminal model of a phase-leg, called the Modular-Terminal-Behavioral (MTB) model. A phase-leg is one of the most redundant topologies within switched power converters and forms a basic switching cell. The goal was to obtain an EMI model of one phase-leg and then use as many instances as necessary, depending on the type of converter, to predict the total EMI from the power supply. Figure 1-1 shows the MTB model and the chopper-circuit that was used for the model extraction by Qian. Although the idea was novel, it was difficult to extract such a model in practice. The model itself had an issue in that it had only two impedances, although three are required for description of a minimum-sized model of a three-terminal network [22]. Another issue was that the model was validated in conditions that were very close to the ones used during model extraction; in other words, no understanding was developed regarding the boundary where the model starts to fail. The cross talk between the phase-leg was not taken into consideration either. The best results for EMI prediction were obtained when only one phase-leg was used [30]. With the addition of another phase-leg [31] and with AC operations [32] the accuracy of prediction worsened. Another limitation of the MTB model was in the understanding of the model itself. It was claimed that the extracted model was of the phase-leg, but no observations that could possibly support that contention were provided. Very little discussion was provided with regards to the model's impedances. The extracted model impedances seemed to be changing with the operating point, which is un-natural and hence worthy of more explanation.

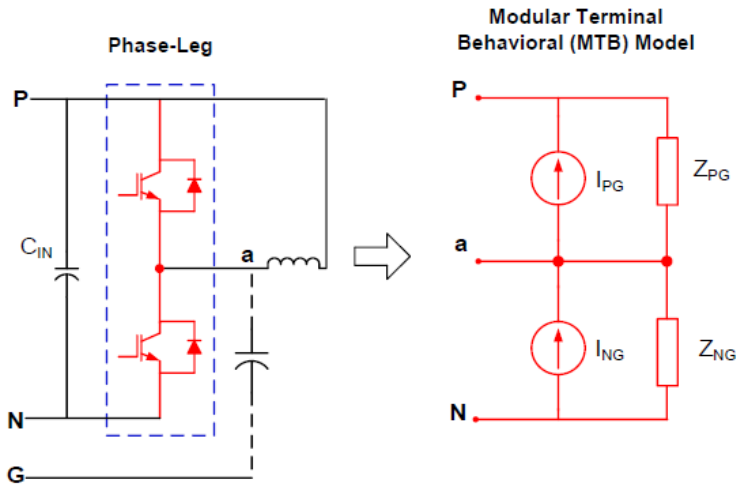

Figure 1-1 Qian's Modular-terminal-behavioral (MTB) model from [49] under fair use

Andrew C. Baisden et al. made several improvements over Qian's MTB model with his generalized-terminal-model (GTM). The major difference is that the entire converter is modeled as a black-box with a three-terminal Norton equivalent and not just a phase-leg. This is shown in Figure 1-2. Another important contribution was the selection of external network impedances (or conditions) for accurate extraction of noise sources and noise impedances [33, 34]. This helped in establishing boundaries on the maximum and minimum impedance at the terminals of the model to ensure that it produced accurate results. From Figure 1-1 and Figure 1-2, it can be seen that the MTB model was modified and that three impedances in delta connection were used instead of two to describe a three-terminal network. The model was validated for a 400W boost converter [35] only; however, it was experimentally shown to have accuracy up to almost 100 MHz, which is beyond the upper frequency of 30 MHz prescribed in conducted emission standards. These results established the advantages of behavioral models over lumped-circuit models. The three-terminal Norton model was also used in [36]. In [37] the three-terminal Norton-equivalent was used to predict the net EMI for two boost converters connected in parallel (on the same dc bus).

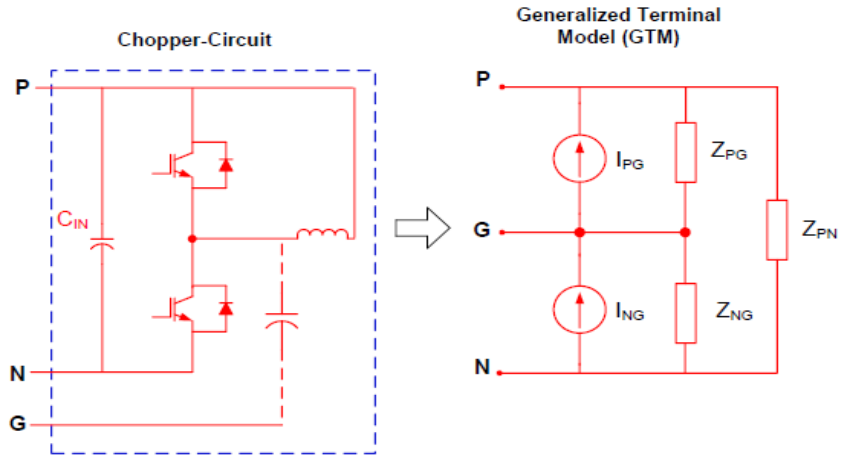

Figure 1-2 Andrew's Generalized Terminal Model (GTM) from [49] under fair use

In addition to these major attempts, several others have published similar ideas over the last decade. In [38, 39] a three-terminal Thevenin equivalent is used for modeling an ac-dc converter. Instead of two sources, the model here has three sources, which are characterized in two different setups. The accuracy was found to be reasonable. In [40, 41], a three-terminal Thevenin equivalent is used to model electronic equipment. The model impedances are extracted by first measuring the complete two-port S-parameters of the system using a vector-network-analyzer (VNA) while it is in operation. This is a limitation, as such measurements are not possible for high power applications. In [42, 43], a similar model was developed without using the VNA.

1.4 Motivation

As higher switching frequency is applied to the SiC switching device, it produces a higher EMI noise emission, thereby challenging the prediction capacity of the EMI behavioral models.

In order to assess the effect on the EMI emission from the higher switching frequency, the common mode (CM) and differential mode (DM) EMI noises are measured in experiments on a three-phase SiC MOSFET inverter with 300 V DC voltage and 3 kW, running at 20 kHz and 70 kHz switching frequency respectively. The corresponding behavioral models in CM and DM for the two switching frequency cases are extracted to evaluate the prediction capacity with the higher switching frequency. The noise floor, which is the main factor limiting the UBM prediction above 10 MHz, is explained and the corresponding development is proposed to extend the UBM prediction capacity to 30 MHz. A detailed explanation of how the higher switching frequency works with the UBM using the proposed improved high frequency UBM extraction procedures is provided in the following chapters.

Chapter 2 . Assessment of Effect on EMI Emission from Different Switching Frequency and Different Switch Devices

With power devices such as SiC or GaN MOSFETs becoming more commercially applied in the industry of power electronics, higher switching frequency is increasingly employed due to its higher precision control in power converters. However, the EMI noise in the system will increase as a result of the higher switching frequency, requiring greater EMI noise reduction. Therefore, it is essential to assess the effects from the switching frequency and different switch devices on the EMI emission.

2.1 Introduction

Increasing switching frequency is an increasingly important trend in power electronics used to shrink total size and volume of passive components in the wake of high power density. The development of new devices, such as GaN and SiC, further drives the growing reality of this trend[44]. However, this faster speed switching action means that the system EMI emission is different, and the existing EMI modeling and filter design process may not be adaptable to this change. It is essential to find out how the switching frequency influences the EMI emission in common mode (CM) and differential mode (DM).

Motor drive is one kind of inverter with serious standards for EMI emission, whose general topology is exhibited in Figure 2-1. The switch devices can be IGBT, MOSFET, and so on. On the DC side of the drive, the EMI noise should be limited below the input EMI standard as in DO-160[45] (Figure 2-2). On the output, DO-160 has requirement on the output cables and bundles (Figure 2-2). In addition, CM noise in the motor needs to be reduced due to its negative effect on the motor's working conditions. In this section, simulations and experiments are performed on the three-phase DC-AC inverter, and the DC and AC side EMI noise are measured in CM and DM. The CM and DM current (noise) is defined in (4.1) and (4.2).

$$i_{CMi} = \frac{i_p + i_n}{2} \qquad i_{CMo} = \frac{i_a + i_b + i_c}{3} \tag{2.1}$$

$$i_{DMi} = \frac{i_p - i_n}{2} \qquad i_{DMo} = \frac{2i_a - i_b - i_c}{3} \tag{2.2}$$

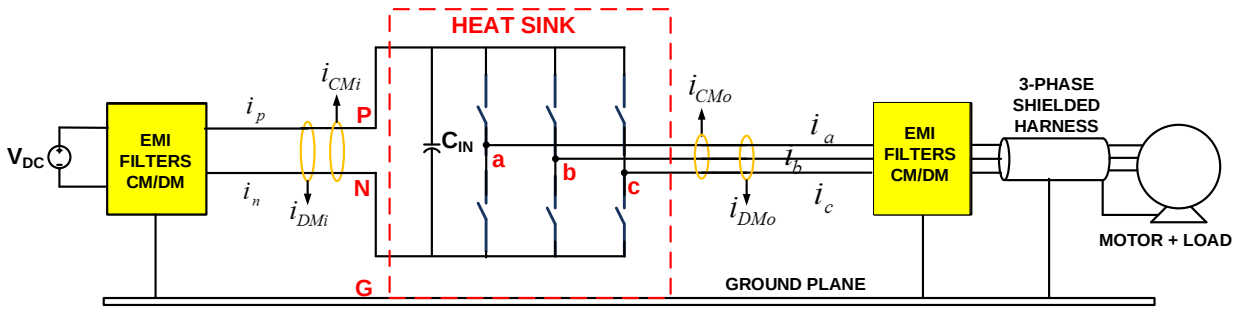

Figure 2-1 General topology and setup diagram for motor drive

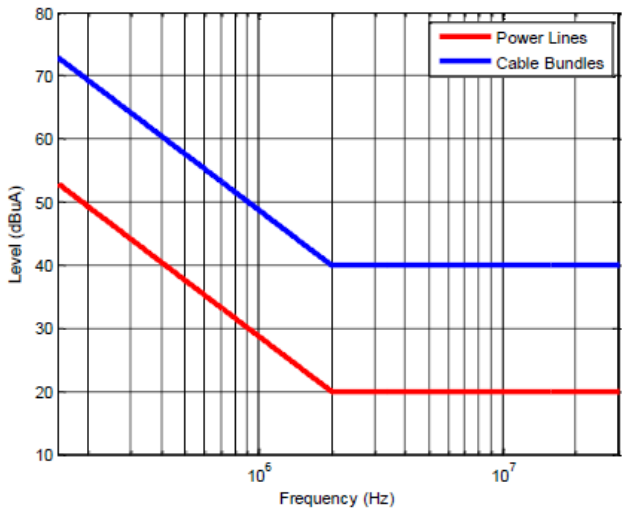

Figure 2-2 Conducted emission limits in DO-160E (Section 21) for L, M &H categories

2.2 EMI emission comparison among different switching frequencies

In this section, the EMI emission of a SiC JFET motor drive is analyzed in a simulation implemented in SABER® Schematics with four different switching frequencies: 20 kHz, 40 kHz, 70 kHz and 100 kHz. The simulation mode is based on the lumped circuit model built in the 2012 SAFRAN project. The corresponding experiments on a SiC MOSFET three-phase inverter are performed with 20 kHz and 70 kHz switching frequency separately to validate the conclusion from the simulation. The new experimental setup is tested first and fixed on the test bench for CM and DM EMI current spectrum measurements.

2.2.1 Lumped circuit setup implemented in SABER®

The lumped inverter model is defined in different parts in Figure 2-1, and will be used in SABER® simulation for assessment of the EMI emission for different working conditions. The sub-model for the LISN (Figure 2-3), the harness (Figure 2-4) and the permanent magnet motor (Figure 2-5) were built as the previous work[46]. The motor drive motor model (Figure 2-6) used in the previous work, which considered all the possible parasitics in the connection, utilizes the ideal switch in SABER® as the switch device in order to have a stable model that can converge faster.

In this section, a SiC JFET model, developed by CPES, replaces the ideal switch as the switch device in the motor drive model (Figure 2-7), with all the parasitic parameters the same as in the original model. The SiC JFET model, whose inner model is shown in Figure 2-8, imitates the normal switching behavior of SiCED — on SiC JFET, bearing 100 more kHz switching frequency and 16 A more current with 1200 kV. The switch is chosen here because it is one of only a few SiC devices that has a SABER model for kW power and works with 300 Vdc.

In addition, a second simulation setup is built with Si MOSFET, which analyzes the effects of different switching frequencies on the EMI emission for a MOSFET inverter. The MOSFET IPB60R125CP (25 A, 600 V) from Infineon has its own physical model in Pspice®. In order to apply it to SABER®, the key parameters, such as on-resistance, and turn-on time, are set in SABER® in accordance with Pspice®. Apart from the switch device, the motor drive model (Figure 2-9) is the same as the original ideal-switch model. This device is chosen here for its application with kW power and 300 Vdc, it's switching frequency of an additional 100 kHz, and the available physical simulation model.

The gate driver for the switches (SiC JFET and Si MOSFET) is chosen as the ideal voltage-control voltage source. Because the EMI emission from different switch devices will be analyzed further, the model requires the same gate driver in the comparison. To avoid requiring extra effect from the gate drivers, the general setting for the gate drivers are chosen. As a result, the total lumped circuit can be combined with the separate parts as shown in Figure 2-10.

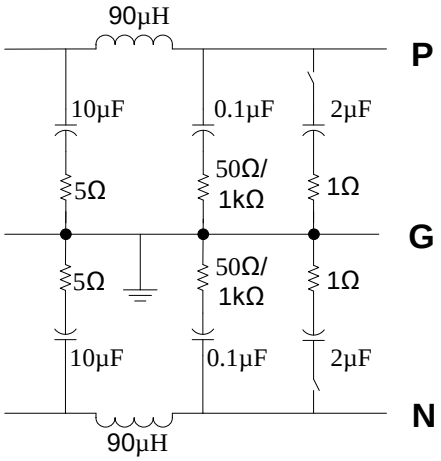

Figure 2-3 Line impedance stabilization network

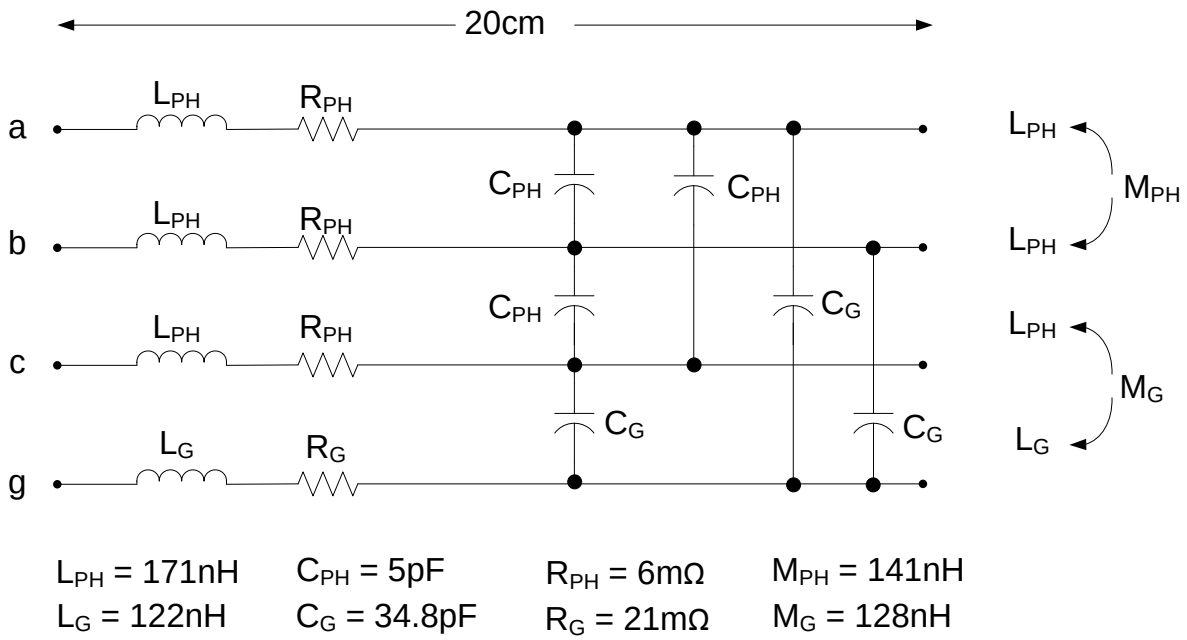

Figure 2-4 Per-unit length parasitic model of the Harness

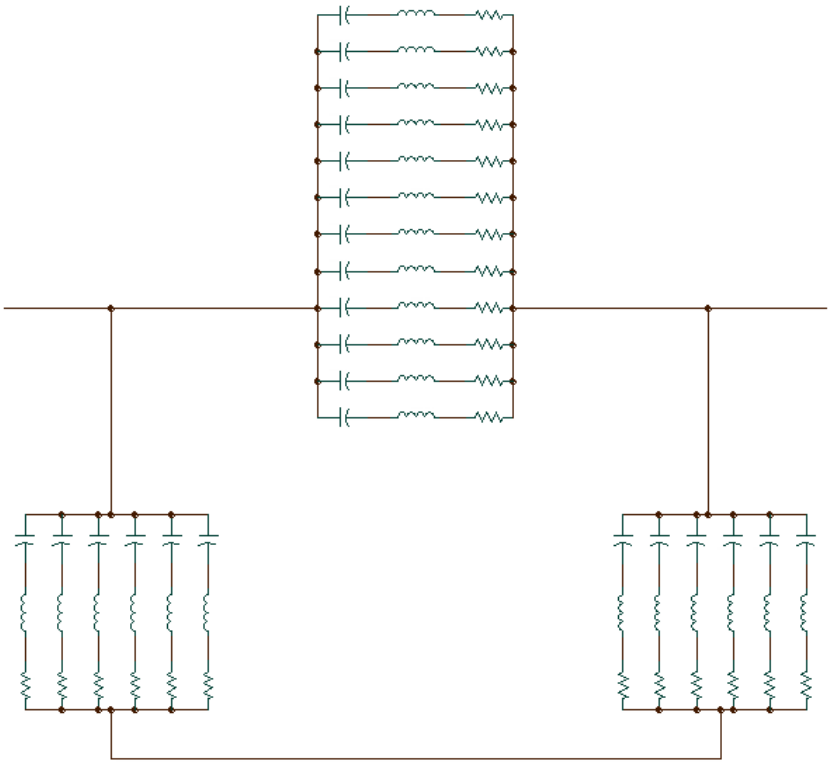

Figure 2-5 Lumped circuit model of a single winding of the motor

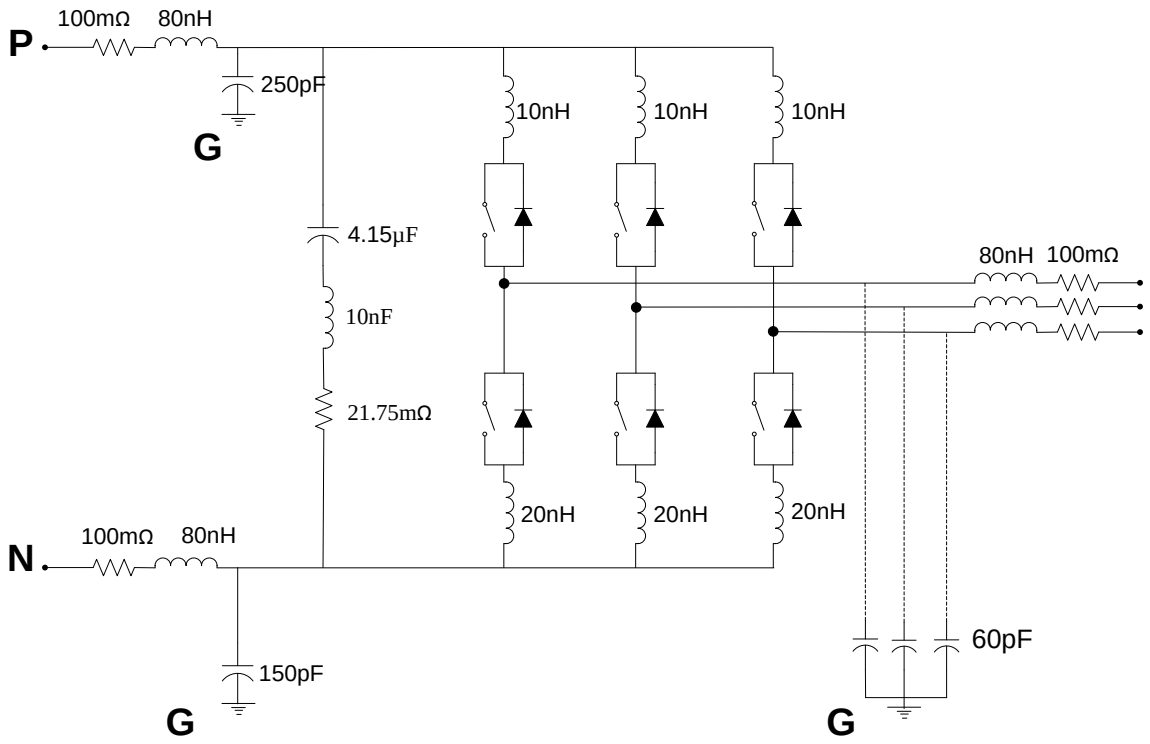

Figure 2-6 SABER® model of three-phase motor drive with ideal switch

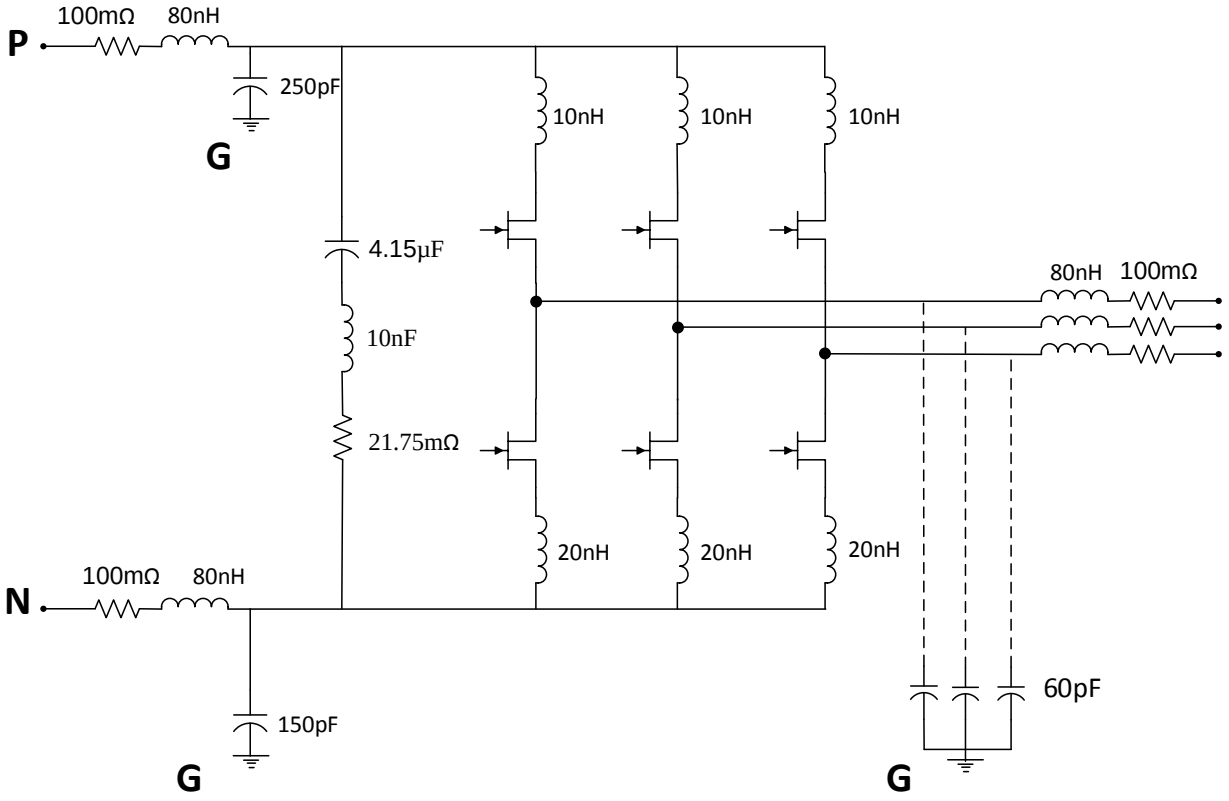

Figure 2-7 SABER® model of three-phase motor drive with SiC JFET

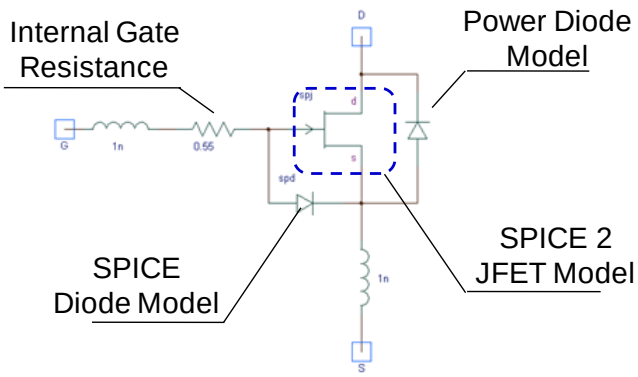

Figure 2-8 Inner model of SiC JFET in SABER®

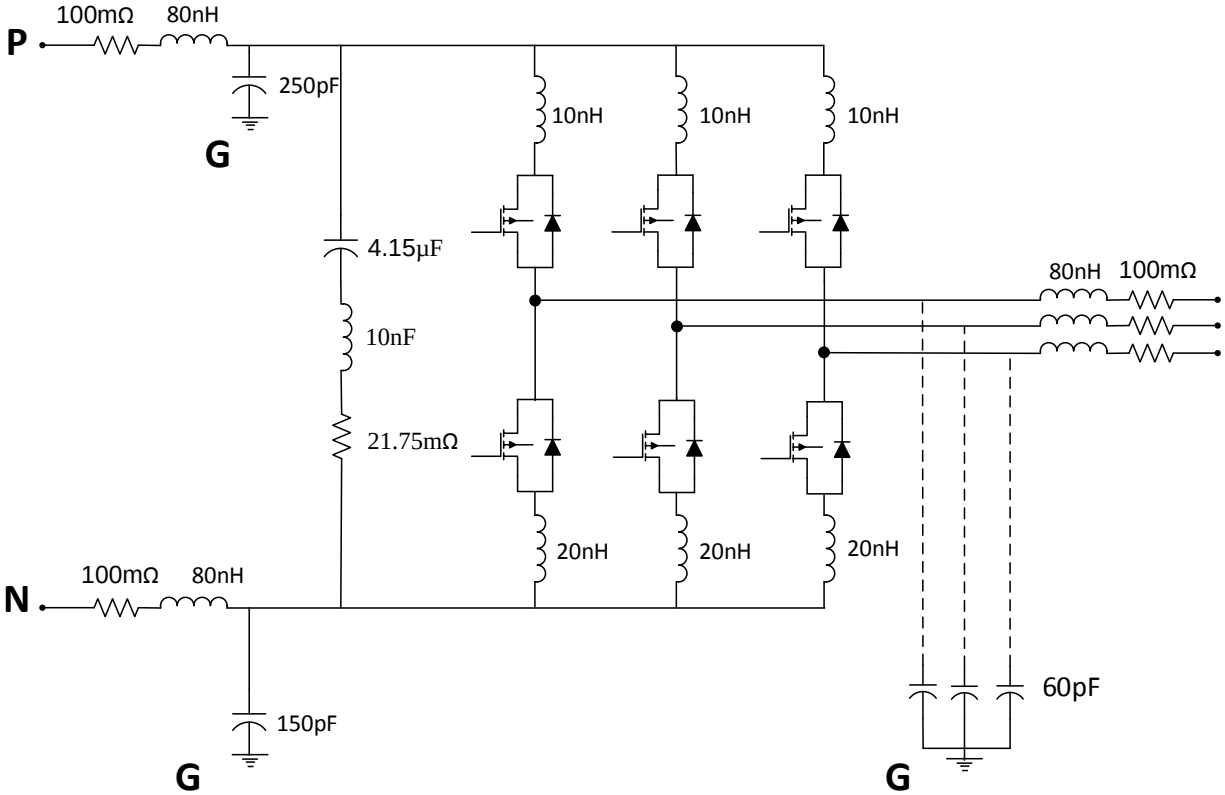

Figure 2-9 SABER® model of three-phase motor drive with Si MOSFET

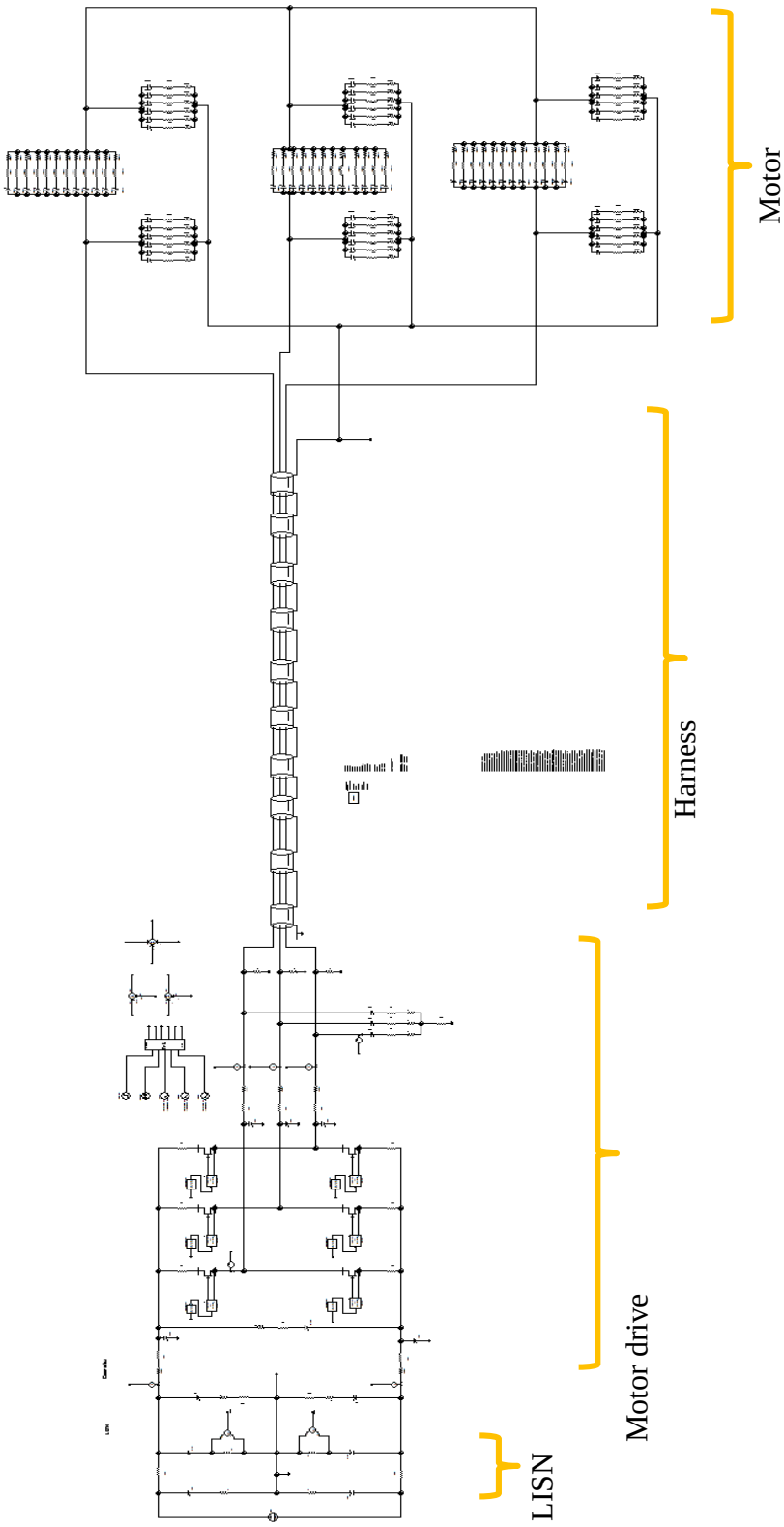

Figure 2-10 SABER® model of full motor drive system

The control strategy applied is the three-phase centered space vector pulse width modulation (SVPWM 3Φ-C). The time-domain CM and DM currents at input and output sides are calculated during the simulation process based on (4.1) and (4.2). The frequency domain spectrums are calculated with FFT for further analysis.

2.2.2 EMI emission comparison among 20, 40, 70 and 100 kHz switching frequency in the simulated Si MOSFET inverter

The CM current spectrums for the 20, 40, 70 and 100 kHz switching frequency cases in the input and output sides are calculated and exhibited in Figure 2-11.

For the input and output current spectrums in the four cases, the first peak of the spectrums are located at the switching frequency, which is also the highest peak among all the frequency components. Comparing the first peaks in the input (or output) spectrums of the four cases, the larger the switching frequency is, the higher frequency the first peak is located and the higher the first peak is. In the MHz range, the noise will be larger with the increased switching frequency. As a result, the CM EMI filter needs a larger attenuation ratio at the same frequency point when the switching frequency is higher. The CM filter designed for the 20 kHz case cannot apply to the 100 kHz case. But the 100 kHz case CM filter can reduce the 20 kHz case CM noise below the EMI standard.

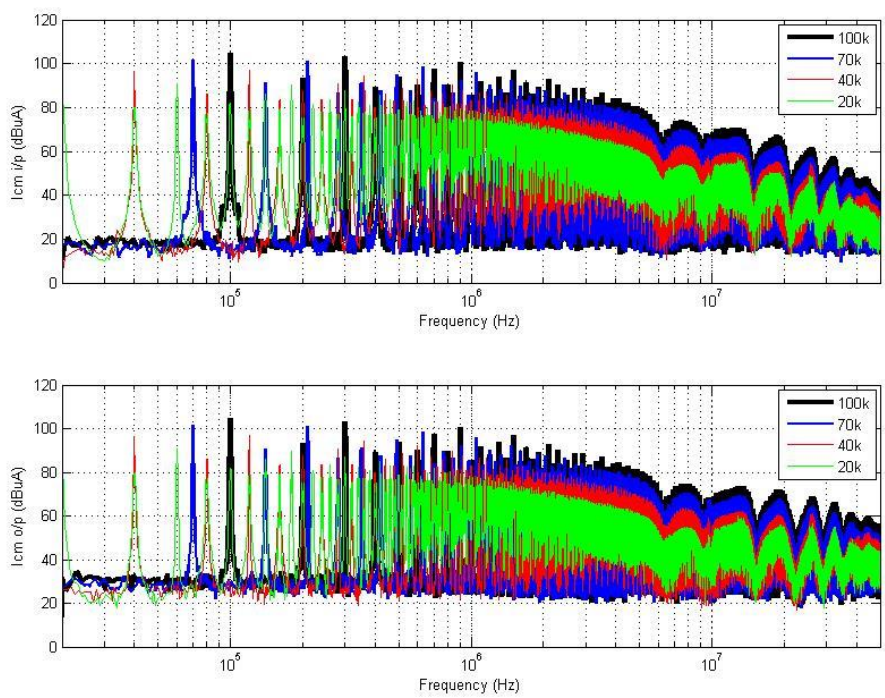

Figure 2-11 Comparison among the CM input (upper) and the output (lower) current spectrums in the Si MOSFET inverter setup with 20 k, 40 k, 70 k and 100 kHz switching frequency

The DM current spectrums for the 20, 40, 70 and 100 kHz switching frequency cases in the input and output sides are calculated and exhibited in Figure 2-12. Similarly to the CM, the first peaks are located at the switching frequency. But at the input side, the first peak is not the highest among all the frequency components. As a result, at the low-frequency (below MHz) DM input side, the EMI filter design should not be dependent on the first peak, but should rather include the other harmonics. For the output DM noise at low-frequency range, the first peaks have almost the same magnitude for different switching frequencies. Therefore in the DM output filter design, the higher switching frequency case needs a filter with a larger attenuation. This is due to the fact that the EMI standard (as in DO-160) at low frequency range requires smaller noise than the higher switching frequency component. As for the noise above MHz, the higher the switching frequency is, the larger the input and output EMI noises are, as was the case with CM. The corresponding filter design for this range should have larger attenuation when the switching frequency is higher.

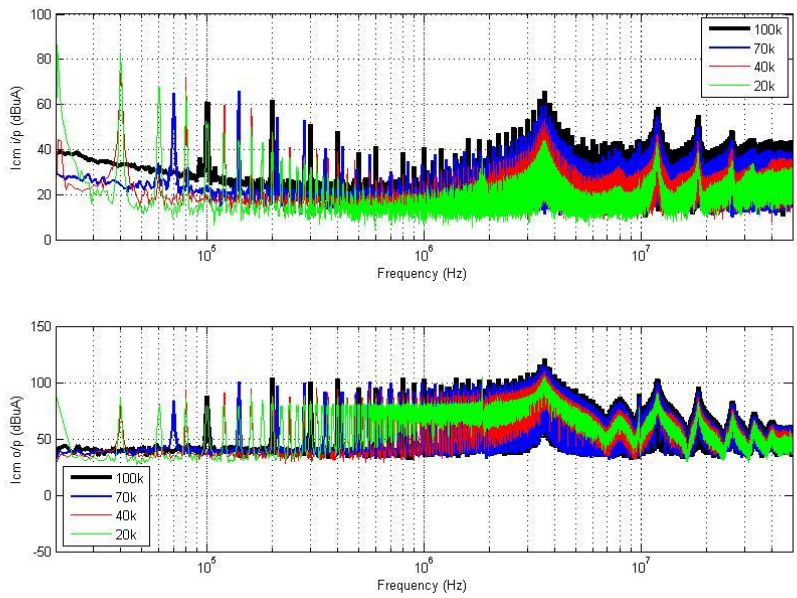

Figure 2-12 Comparison among the DM input (upper) and the output (lower) current spectrums in the Si MOSFET inverter setup with 20 k, 40 k, 70 k and 100 kHz switching frequency

2.2.3 EMI emission comparison among 20 and 70 kHz switching frequency in the simulated SiC JFET inverter

A similar comparison is performed with the SiC JFET inverter with 20 kHz and 70 kHz switching frequency, whose circuit is shown in Figure 2-7. Figure 2-13 exhibits the CM input and output current spectrums in the two switching frequency cases, and Figure 2-14 illustrates the DM input and output current spectrums.

For CM spectrums, the conclusion drawn from the comparison is the same as that for MOSFET. The first peak located at the switching frequency will be higher for the higher switching frequency. Above MHz, the higher switching frequency causes higher noise.

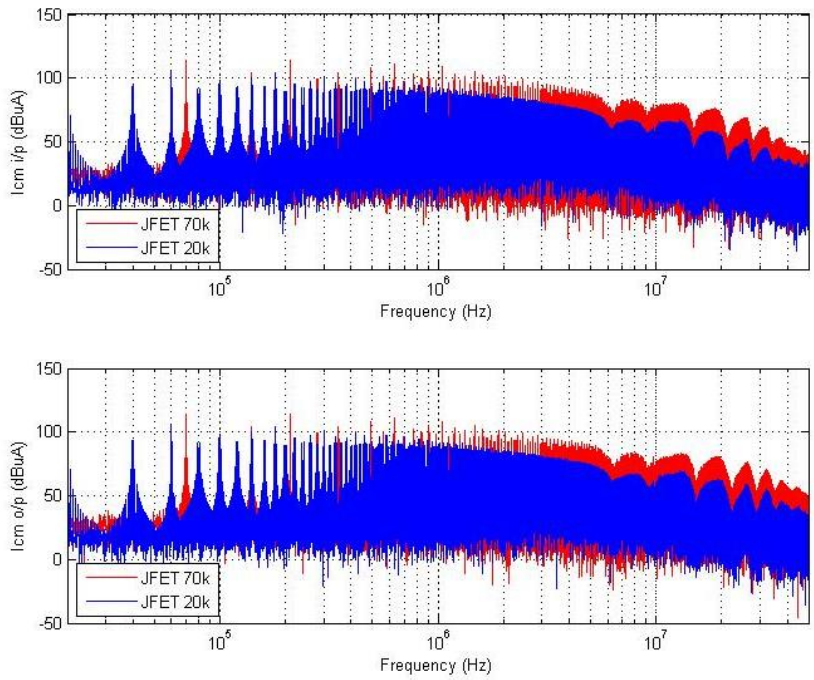

Figure 2-13 Comparison among the CM input (upper) and the output (lower) current spectrums in the SiC JFET inverter setup with 20 k and 70 k Hz switching frequency

The DM current spectrums in the two switching frequency cases are compared in Figure 2-14. In the DM input or output spectrum, the second peak located at the switching frequency is the largest, and will be larger with increased switching frequency. At MHz range, similarly to CM, the DM emission will be larger in the higher switching frequency cases. The effect on the DM EMI filter design from the switching frequency is the same as that of the CM.

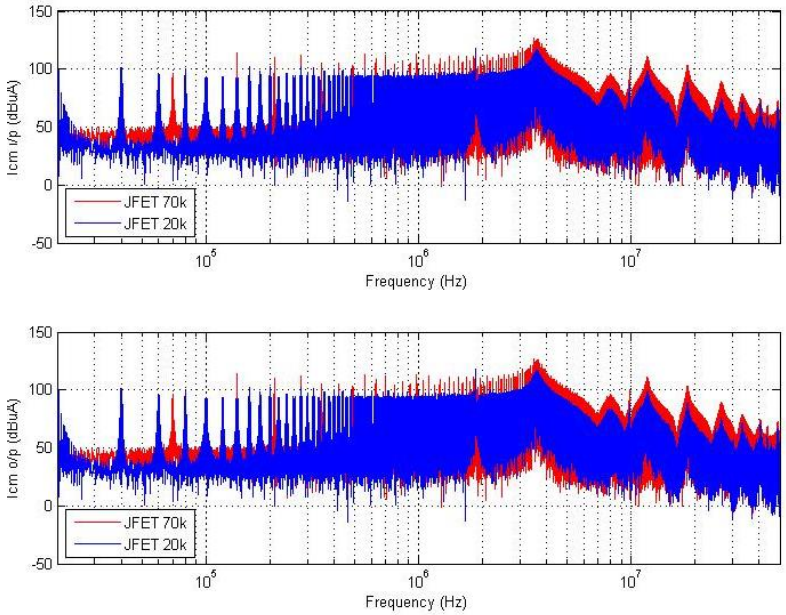

Figure 2-14 Comparison among the DM input (upper) and the output (lower) current spectrums in the SiC JFET inverter setup with 20 k and 70 k Hz switching frequency

A. SiC MOSFET inverter setup

The experiments are performed to validate the conclusion in the simulation. The three-phase SiC MOSFET inverter and its setup are built as shown in Figure 2-15.

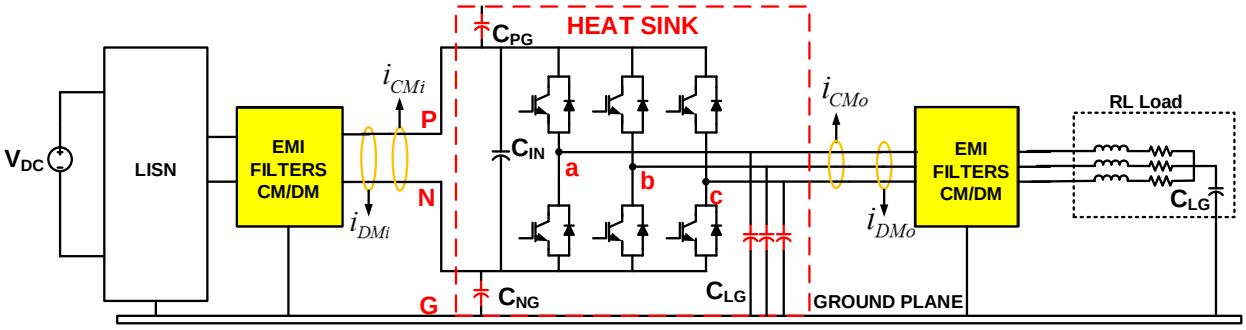

Figure 2-15 Three-phase SiC MOSFET inverter setup schematic diagram

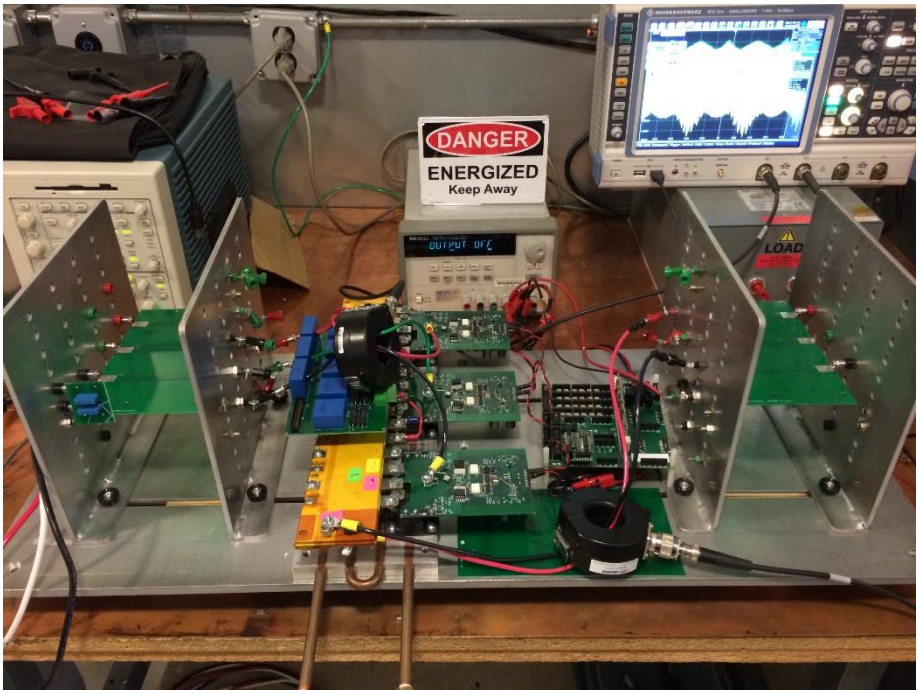

Figure 2-16 SiC MOSFET inverter setup

There are three SiC MOSFET half-bridge modules from CREE utilized (model CAS100H12AM1) and six ceramic capacitors with 15 μF at DC bus. This CREE model can hold 100 A and 1.2 kV. The DC bus capacitors can afford 900 Vdc. The heat sink is fully in contact with the three switch modules.

The gate driver designed for the switch modules is placed on top of the module, which has two second-stage drivers with a Mill clamp circuit and a desaturation protection circuit. In addition, the dead time between the two signals of one module can be set on the gate driver.

The control board for the inverter is placed next to the inverter. On the board, a DSP is responsible for PWM generation based on the 3Φ-C SVPWM strategy. A CPLD controls protection based on the information from another board measuring the real-time DC bus voltage and three output current. Once the DC bus voltage or the current is over high, the CPLD will give a shut-down order for the PWM signal to the gate drivers.

Another DC source is used to power the control board and voltage/current measurement board. This auxiliary source will actually cause an extra propagation path from the inverter to the CM ground, influencing the EMI emission of the system. However, the EMI emission from the auxiliary source is 50 dB smaller than the one from the inverter. So in the assessment of EMI noise for this setup, we can ignore the effect from the extra source.

The whole inverter setup is fixed on a steel frame, which can place EMI filters at the input and output sides of the inverter. The heat sink of the inverter is in full contact with the steel frame. The frame is placed on a copper sheet on the test bench and connected to the CM ground of LISN. Therefore, the steel frame can be seen as the CM ground in the experiment. There will be some

parasitic capacitive components from the inverter terminals to the steel frame, which mainly compose the CM propagation path.

A. LISN and DC source

The LISN No. on the test bench is FCC-LISN-50-32-2-MS461E DC-60Hz/480V/32Arms.

The DC source is from Magna-power electronics, generating 600 Vdc/ 20 Adc.

B. RL Load

The load of the inverter (Figure 2-17) is chosen to be a resistor-inductor-in-series combination. Each phase has 3.3 Ω resistance and 30 mH inductance. At the end of each phase, two cables connect the three-resistor-end terminals as one neutral point. Due to the large size and weight of the RL load, the load has to be placed on the ground of the lab, separated from the test bench. In order to complete the CM loop, a 5 nF capacitor will be placed between the neutral point and the CM ground. Though the load is simply connected, there will be complex parasitics on all the connected cables and the connectors, which is hard to express using a lumped circuit.

Figure 2-17 RL load

C. Current measurement

In the experiment, the CM and DM input/output current are directly measured by two current probes. The probe ETS LINDGREN 95510 can measure the pass-through current from 20 Hz to 100 MHz. In order to measure CM current, the input (and output) wires should go through the probes in the same direction as Figure 2-18 in accordance with (3.1). As for the DM current measurement, according to (3.2), at the input side, the positive and negative wire should be in opposite directions (left side of Figure 2-19) and the output three-wire should be twisted as shown in the right side of Figure 2-19.

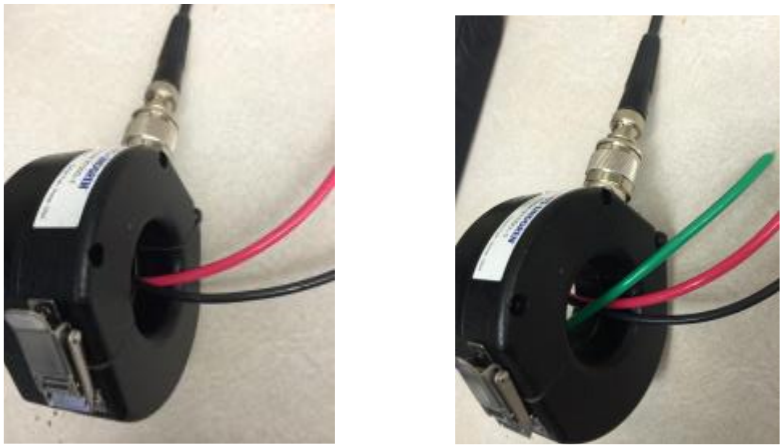

Figure 2-18 Probe placement in CM input (left)/ output (right) current measurement

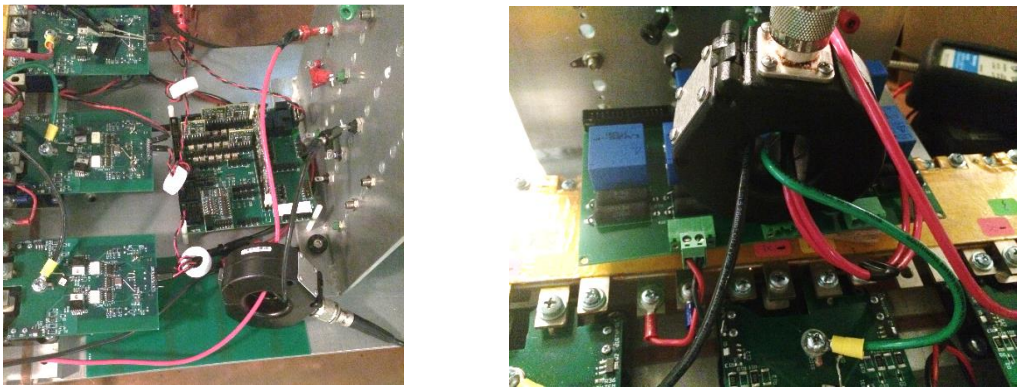

Figure 2-19 Probe placement in DM input (left)/ output (right) current measurement

2.2.4 EMI emission comparison among 20 and 70 kHz switching frequency in experiment

The experiment results (Figure 2-20 and Figure 2-21) in this section are the same as those in the simulation (Figure 2-13 and Figure 2-14).

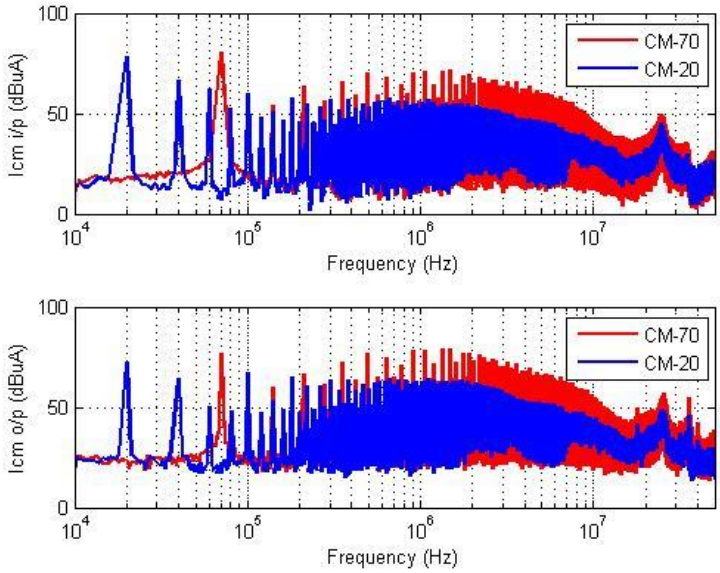

Figure 2-20 Comparison among the CM input (upper) and the output (lower) current spectrums in the SiC MOSFET inverter experimental setup with 20 k and 70 k Hz switching frequency

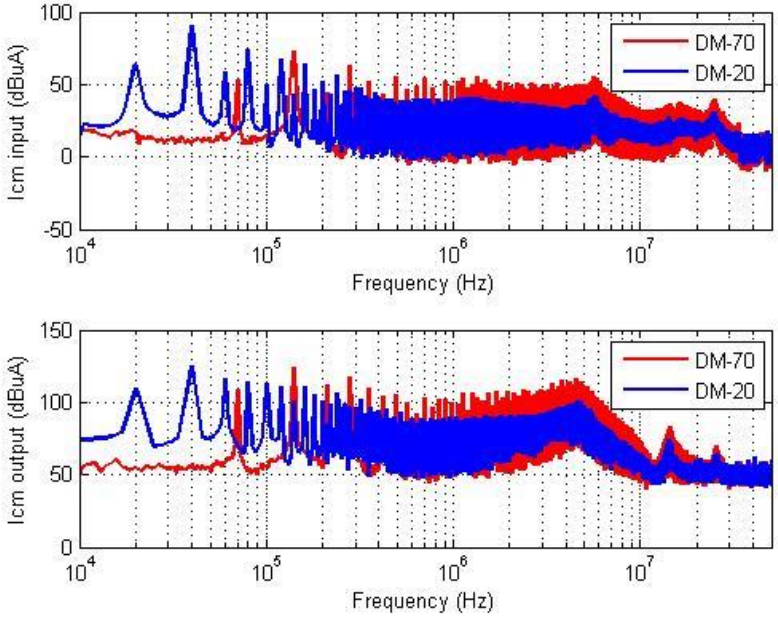

Figure 2-21 Comparison among the DM input (upper) and the output (lower) current spectrums in the SiC MOSFET inverter experimental setup with 20 k and 70 k Hz switching frequency

2.3 EMI emission comparison among ideal switch, Si IGBT, Si MOSFET, and SiC JFET in simulation

The inverter lumped simulation models with the ideal switch, MOSFET and JFET have been illustrated above. The model with Si IGBT is shown in Figure 2-22. The main differences between those four switch devices in the simulation are listed in Table 2-1, including the switching speed and on-resistance. The CM and DM emissions of the four inverters with the same load are measured in Figure 2-23 and Figure 2-24. It is shown that the EMI emission in CM or DM is quite independent of the switching device below 10 MHz, when the dead time of the PWM strategy is considered based on the slowest switching speed (the ideal switch). However, above 10 MHz, the MOSFET case tends to have larger CM and DM noise because it has the smallest on-resistance.

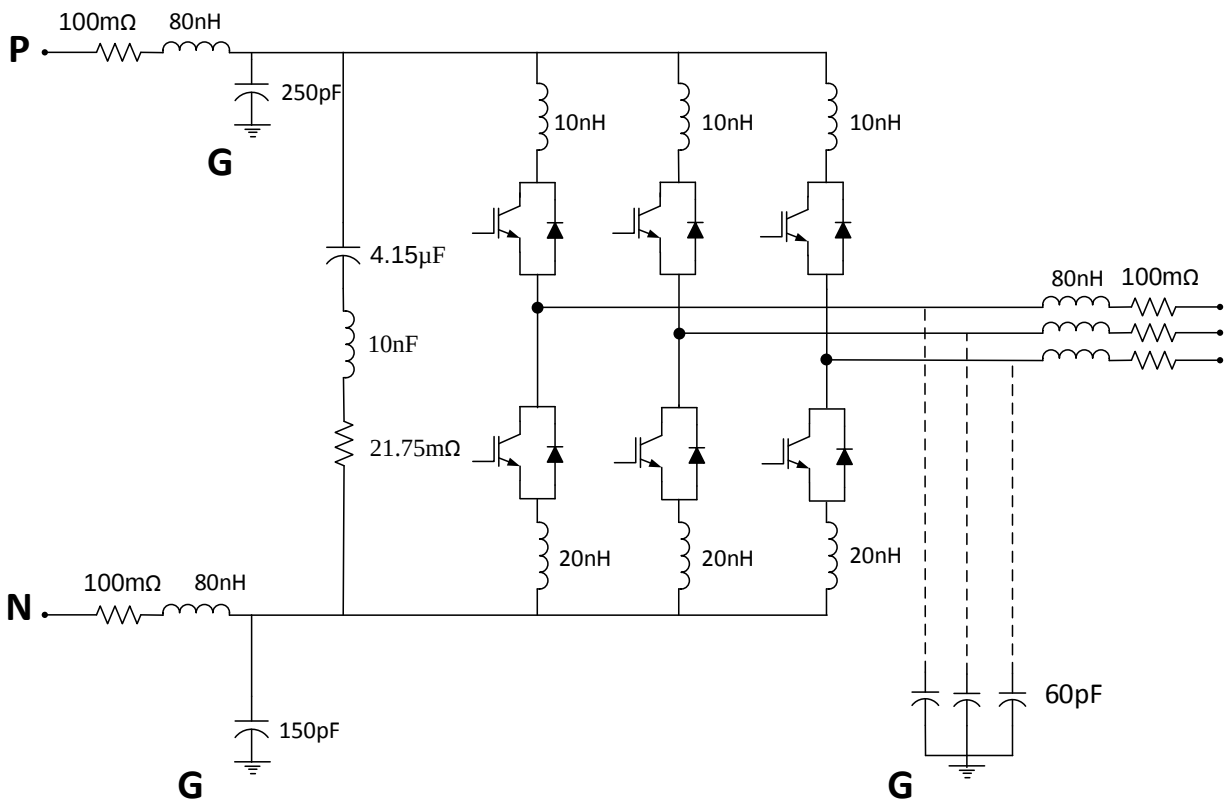

Figure 2-22 SABER® model of three-phase motor drive with Si IGBT

Table 2-1 The differences between the ideal switch, Si IGBT, Si MOSFET, and SiC JFET in the simulation

Switch	Ideal switch	IGBT: HGTG30NG60B3	MOSFET: IPB60R125CP	JFET:
Company	--	Fairchild	Infineon	

Operating condition	--	30A, 600V	25A, 600V	5A, 1200V
Switching Frequency	--	<50kHz	>100kHz	>70kHz
R_{on}/Ω	0.01	0.0483	0.11	0.025
t_{on}/ns	100	36	15	--
t_{off}/ns	100	137	50	--
R_g/Ω	--	3	1	--
Available simulation model		SABER	Pspice	SABER

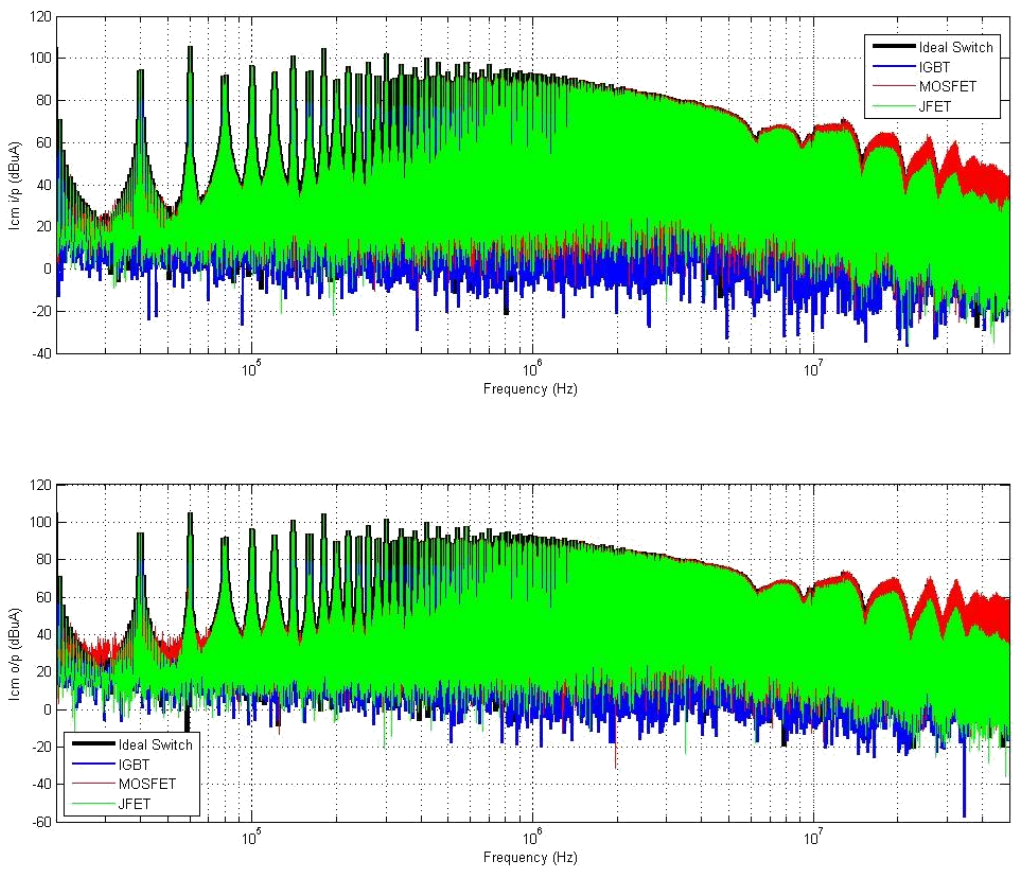

Figure 2-23 Comparison of the input (upper) and output (lower) CM emission with different switching devices.

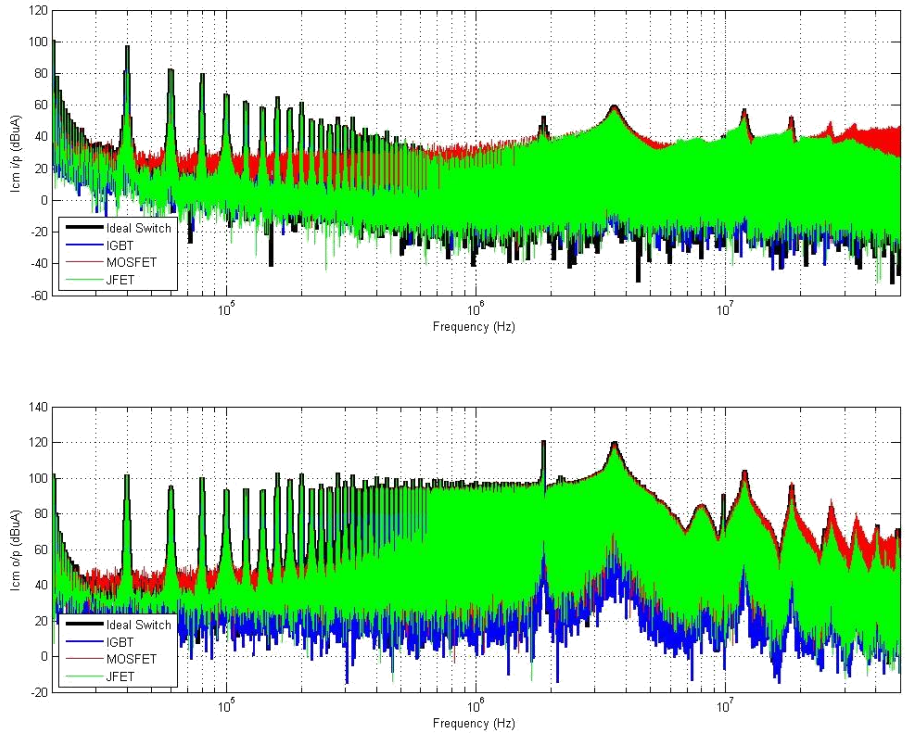

Figure 2-24 Comparison of the input (upper) and output (lower) DM emission with different switching devices.

2.4 Conclusion

In conclusion, with the higher switching frequency, the EMI noise will be larger, and necessitates having effective EMI filters, which can be easily designed based on an effective EMI model in the high frequency. When the on-resistance of the switching devices is smaller, the CM and DM noise will be larger above 10 MHz.

Chapter 3 . CM Unterminated Behavioral Modeling for SiC Inverter

There are generally two kinds of EMI noise: radiative and conducted noise. The latter is transferred along the wire and finally to components such as the radio and motor, where it will have a negative effect. CM noise will cause the voltage drop from the rotor to stator causing the motor to run out of order. So it's essential to reduce the conducted EMI. Use of an EMI filter is the most common way to suppress the conductive EMI noise. However, the complexity of EMI-related issues, which involves all the possible parasitic components in the system, makes it difficult to design an EMI filter. EMI modeling will provide an analysis of the system's EMI emission and can predict the EMI emission with a designed EMI filter to check the feasibility of the solution.

With the terminal behavioral model, input filters can be implemented between the source and the model and then the appropriate filter parameters can be calculated. However, if an output filter is inserted between the model and load, the input EMI emission will be changed due to the coupling at the input and output sides. Therefore, the input filters will need to re-designed, as they may not reduce the noise below the requirement or may become oversized with over suppression.

The unterminated behavioral model (UBM) will predict the EMI noise emission at both the input side and output side. As a result, the UBM can help with the EMI filter design at both sides at the same time, thereby avoiding the filter re-design issue.

Adding to design considerations, standards such as DO-160 will mean that there are requirements for all the cables and bundles, including the connection between the converter and load. It's therefore also necessary to find the output EMI emission when the load loop changes.

3.1 Introduction

The unterminated model is proposed in [47] and [48] based on a commercial motor drive system as shown in Figure 3-1. This test set-up consists of a standard LISN terminated with 25 Ω resistance, a 2kW motor-drive, a three-phase shielded cable (32 feet), and a 5hp (3.73 kW) motor with a blower acting as a constant load. The entire set-up is kept on a copper sheet, except for the motor. The input voltage to the drive is 300V (VDC). The line frequency is set to 40 Hz and the switching frequency of the drive with Si IGBT as switch devices is 10 kHz.

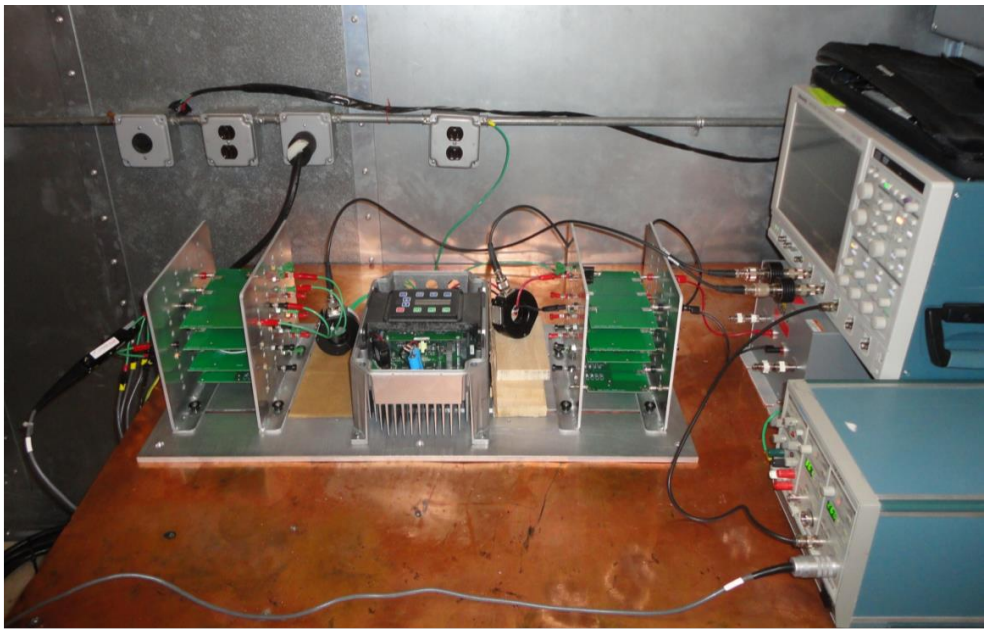

Figure 3-1 Motor drive set-up for unterminated CM model extraction

The CM UBM extraction and validation are finished with the modeling procedures demonstrated in the next section. The final results for one of the validation cases is shown in Figure 3-2. It can be seen that the model is able to accurately predict the conducted emission up to 20 MHz. With another validation case in Figure 3-3, the predictions are good up to at least 30 MHz.[47] As a conclusion for the UBM motor, the model shows accurate prediction capacity in almost every EMI range. But for some cases, the prediction capacity will be reduced to a lower range due to the noise floor issue.

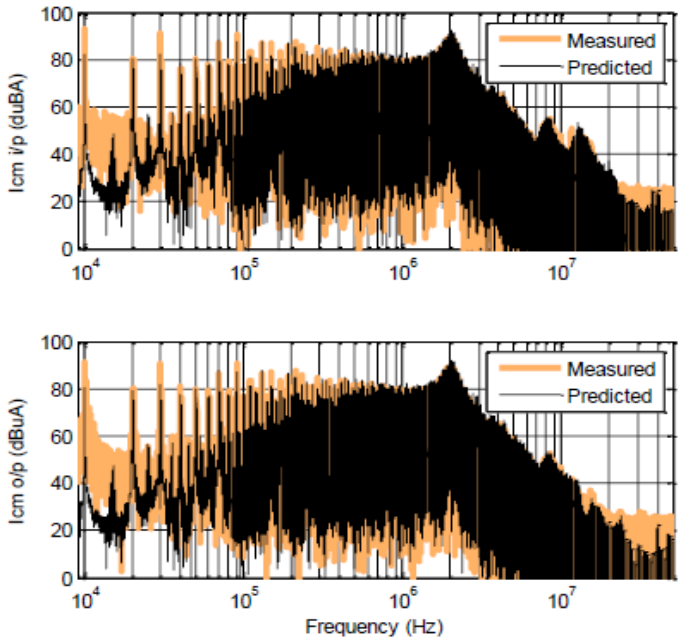

Figure 3-2 Comparison of measured and predicted CM currents for CM-DM filter inserted at the input side of the motor drive

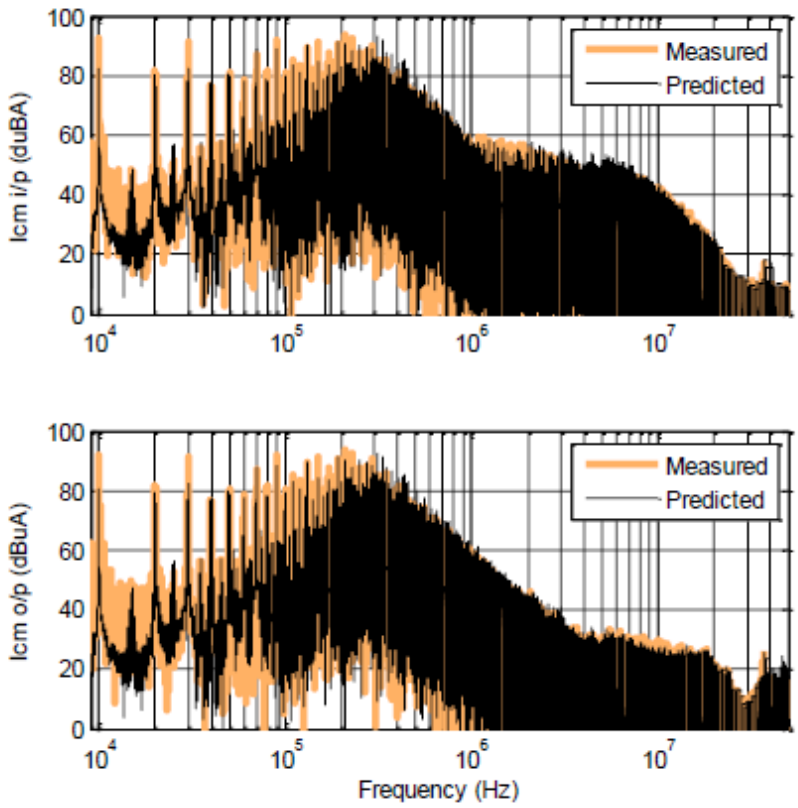

Figure 3-3 Comparison of measured and predicted CM currents for DM EMI filter inserted in the output side of the motor-drive

Generally, there will be a noise floor issue when the noise in the propagation path is so loud that the measurement tool cannot capture the smaller noise component above 10 MHz. In Chapter 7, we found that the CM and DM EMI noise will be larger when higher switching frequency is adopted into the system. In addition, an inverter with MOSFET switch performing high di/dt and dv/dt will have larger EMI noise in the system. Also, for some cases, the CM propagation has larger capacitive components from the inverter to the CM ground. These cases above will tend to have serious noise floor phenomena due to the larger EMI noise.

In this chapter, the detailed procedure to extract UBM is first illustrated with corresponding physical meanings. Then the model is adapted to a SiC MOSFET three-phase inverter with switching frequency of 20 kHz and 70 kHz. The comparison between the model predictions and the experiment measurements will show the UBM prediction capacity in these cases. The noise floor issue, which limits the UBM application scope, will be explained in detailed with an effective developer. Moreover, at high frequency range above 10 MHz, an improved high frequency UBM will be proposed with an improved impedance fixture design. The improved model will show the accurate prediction in the whole EMI range in all conditions.

3.2 UBM and Modeling procedure

Figure 3-4 shows a general setup for an inverter system with CM ground, which illustrates the possible CM propagation from the inverter to the CM ground. C_{PG} , C_{NG} and C_{LG} represent the parasitic capacitors between the inverter (positive input, negative input, output terminals) and the CM ground plane. The common mode current and the differential mode current are defined as (5.1) and (5.2). i_p and i_n are input current at the positive and negative terminal. i_a, i_b and i_c are separate three-phase output currents.

$$\begin{aligned} i_{CMi} &= (i_p + i_n)/2 \\ i_{CMo} &= (i_a + i_b + i_c)/3 \end{aligned} \tag{3.1}$$

$$\begin{aligned} i_{DMi} &= (i_p - i_n)/2 \\ i_{DMo} &= (2i_a - i_b - i_c)/3 \end{aligned} \tag{3.2}$$

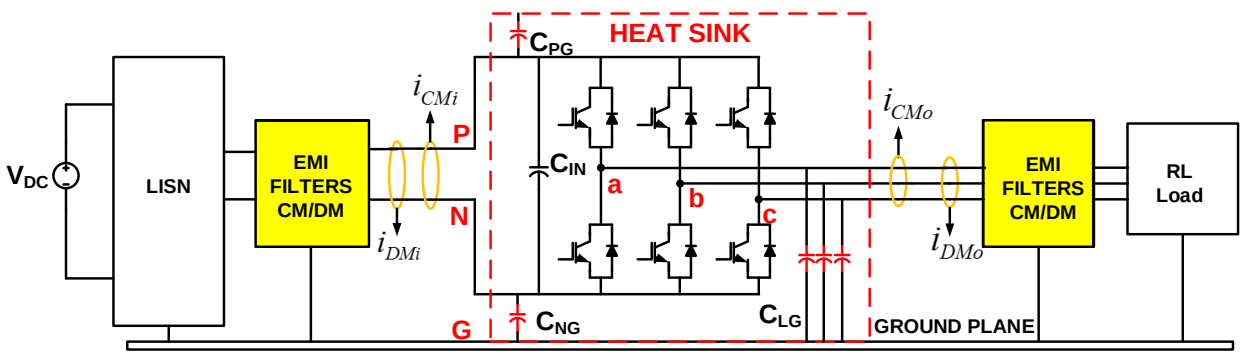

Figure 3-4 General setup for an inverter system with CM ground

The CM unterminated behavioral model characterizes the three-phase inverter in the red dashed square in Figure 3-4 with two noise sources (V_{N1} and V_{N2}) and an impedance matrix (Z_{11} , Z_{12} , Z_{21} and Z_{22}) as Figure 3-5 exhibits. Z_i is the total CM input impedance before the inverter, including the DC source, LISN, and the input side EMI filter. Z_o, the total CM output impedance, consists of the load and the output EMI filter impedance in CM. Due to the symmetric structure of an inverter system, we will have:

$$Z_{21} = Z_{21} \tag{3.3}$$

The aim of this section is to identify the two noise sources and three impedance parameters, which have the relationship of (5.4). Figure 3-6 is equivalent to Figure 3-5 if we clarify the Z-matrix arrangement.

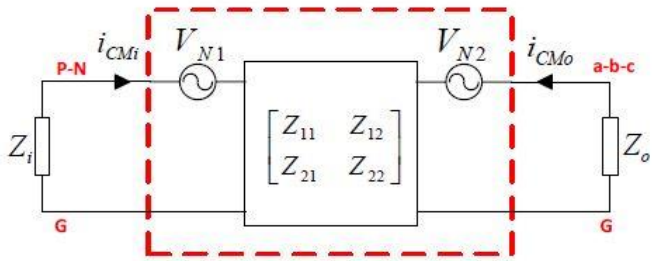

Figure 3-5 Unterminated behavioral model to be extracted

$$\begin{bmatrix} -i_{CMi}Z_i \\ -i_{CMo}Z_o \end{bmatrix} = \begin{bmatrix} Z_{11} & Z_{12} \\ Z_{21} & Z_{22} \end{bmatrix} \begin{bmatrix} i_{CMi} \\ i_{CMo} \end{bmatrix} + \begin{bmatrix} V_{N1} \\ V_{N2} \end{bmatrix} \tag{3.4}$$

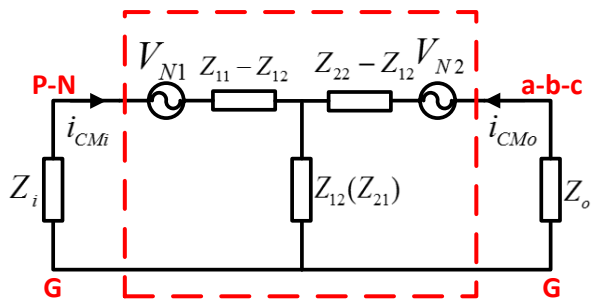

Figure 3-6 Equivalent unterminated behavioral model

3.2.1 Impedance identification

First, methods for measuring the CM impedance should be clarified. From the CM point of view, the CM current flows through at the same time, and the corresponding CM input inverter impedance is the total impedance from the input positive and negative terminal to the ground. In order to find the total impedance with the impedance analyzer, the input positive and negative terminal should be short circuited as one terminal. The input CM impedance Z_i can then be measured from this short-circuit terminal to the CM ground. Similarly, the output impedance Z_o is measured from the short-circuit 3-phase output terminals to the CM ground. During measurement, there is no power in the system. All impedance measurements with the impedance analyzer should be made without power. In addition, the setup for input Z_i and output Z_o should not be changed after the measurement, or a new measurement should be performed to include all the parasitic components in the propagation.

In order to analyze the inverter's impedance (Z_{11} , Z_{12} and Z_{22}), we can refer to the CM propagation in the inverter in Figure 3-7. In Figure 3-7, some of the CM current i_{CMi} flows to the ground through C_{PG} and C_{NG} , then the rest transfers to i_{CMo} through the six switches and three C_{LG} filters. This propagation can be extracted into Figure 3-8.

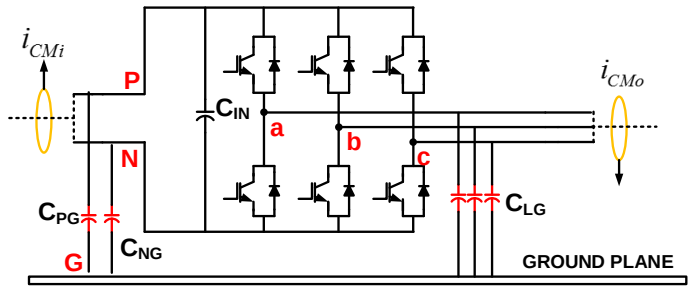

Figure 3-7 CM propagation in the inverter

In Figure 3-8, C_{IG} describes the total effect of C_{PG} and C_{NG}, which can be seen as the parallel impedance of C_{PG} and C_{NG}. Similarly, C_{OG} refers to the parallel results of the three output capacitors C_{LG}. C_{SW} and R_{SW} represent the effect from the six switches. When the inverter is working, one of the two switches is always in one phase leg on, through which most of the CM noise goes. Therefore, it can be seen approximately as a short circuit between P-N to a-b-c terminal for CM noise. As a result, R_{SW} will be much smaller compared with the impedances of C_{IG} and C_{OG} as seen in (5.5). We will get an approximation of (5.6), which can be compared with the equivalent circuit in Figure 3-6. Furthermore, the inverter impedances Z_{11} and Z_{22} can be measured at power-off condition. This is because the switches can be seen as big impedances without switching behavior. The impedance at the inverter input side, shown in the impedance analyzer with the CM impedance measurement method demonstrated above, should be $Z_{C_{IG}}$. The output inverter impedance measurement is equivalent to $Z_{C_{OG}}$. These impedance measurements are close to the real condition with power-on. Hence, in UBM, Z_{11} and Z_{22} can be measured in the power-off condition with the impedance analyzer. Z_{12} can be measured with a network analyzer, or is approximately equivalent to $\frac{Z_{11}Z_{22}}{Z_{11}+Z_{22}}$.

$$\begin{aligned} Z_{C_{SW}\|R_{SW}} &\ll Z_{C_{IG}} \\ Z_{C_{SW}\|R_{SW}} &\ll Z_{C_{OG}} \end{aligned} \tag{3.5}$$

$$Z_{11} \approx Z_{12} \approx Z_{22} \approx Z_{C_{IG}\|C_{OG}} = \frac{Z_{C_{IG}} Z_{C_{OG}}}{Z_{C_{IG}} + Z_{C_{OG}}} \tag{3.6}$$

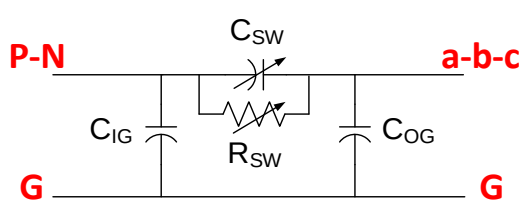

Figure 3-8 Equivalent CM inverter impedance

3.2.2 Noise source extraction

There is no direct way to measure the two noise sources (V_{N1} and V_{N2}) as the inverter impedances. One experiment at the standard working condition is performed by measuring i_{CMi} and i_{CMo} simultaneously. In the setup, two CM chokes are inserted into the input and output sides (Figure 3-9) to acquire high impedance for Z_i and Z_o.

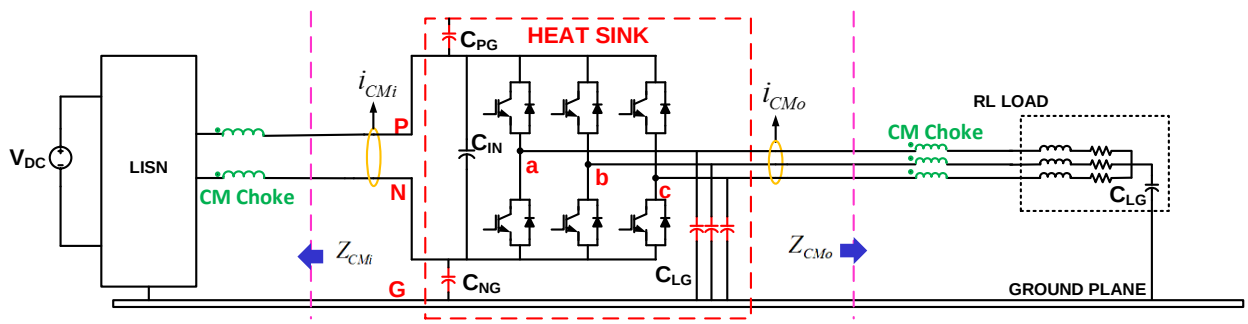

Figure 3-9 Inverter setup with CM chokes

The noise sources can then be calculated with (5.7) after FFT of the measured currents in the time domain. However, Z_{11}, Z_{12} and Z_{22} are only approximate results, causing extra error in the equivalent noise sources. In order to avoid using imprecise impedance, the chokes should be fabricated with the assumption that the input impedance Z_i and the output impedance Z_o are much larger (20dB) than the inverter impedances 5.8). Then equation (5.7) will be simplified to (5.9), avoiding the inverter impedances. Hence the equivalent noise sources are extracted.

$$\begin{bmatrix} V_{N1} \\ V_{N2} \end{bmatrix} = -\begin{bmatrix} i_{CMi} Z_i \\ i_{CMo} Z_o \end{bmatrix} - \begin{bmatrix} Z_{11} & Z_{12} \\ Z_{21} & Z_{22} \end{bmatrix} \begin{bmatrix} i_{CMi} \\ i_{CMo} \end{bmatrix} \tag{3.7}$$

$$\begin{aligned} Z_i &\gg Z_{11}, Z_{12} \\ Z_o &\gg Z_{22}, Z_{12} \end{aligned} \tag{3.8}$$

$$\begin{bmatrix} V_{N1} \\ V_{N2} \end{bmatrix} = -\begin{bmatrix} i_{CMi} Z_i \\ i_{CMo} Z_o \end{bmatrix} \tag{3.9}$$

3.2.3 Optimized inverter impedance

With the impedance measured in Section 3.2.1 and the equivalent noise sources discussed in Section 3.2.2, the elementary model can be used to predict the EMI noise with a different Z_i and Z_o. However, compared with experimental measurement and the model prediction, this method

shows obvious errors in the whole frequency range. One of the reasons for the mismatch is the approximate inverter impedance. At any rate, the real impedance cannot be measured with the impedance analyzer when the inverter is working with power. Therefore, another experimental case is performed to optimize the inverter's impedances.

In this case, two CM shunts are inserted into the system as in Figure 3-10. As a result, Z_i and Z_o are much smaller than the inverter impedances (5.10). Measures of i_{CMi} and i_{CMo} simultaneously show more information about the inverter's impedance. Due to Equation (3.10) and (5.4), i_{CMi} is dependent on Z_{11} and Z_{12} ; i_{CMo} is dependent on Z_{12} and Z_{22} . The measured current spectrums (i_{CMi} , i_{CMo}) are called i_{ip-m} and i_{op-m} . The prediction results of the input and output CM current using the model extracted are called i_{ip-p} and i_{op-p} .

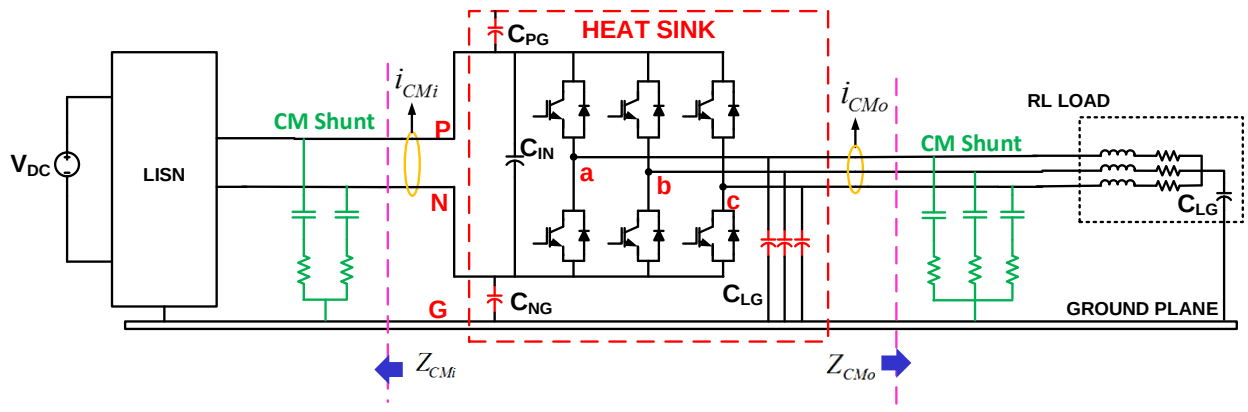

Figure 3-10 Inverter setup with CM shunts

$$\begin{aligned} Z_i &\ll Z_{11}, Z_{12} \\ Z_o &\ll Z_{22}, Z_{12} \end{aligned} \tag{3.10}$$

In the optimization, the error between the theoretical predictions (i_{ip-p} and i_{op-p}) and the experiment measurements (i_{ip-m} and i_{op-m}) are minimized with the aim function (5.11) by optimizing three inverter impedances. The optimization impedances are the final identification for the model and then UBM is ready to perform validation cases to check the feasibility and prediction capacity.

$$\min((|i_{ip-m}| - |i_{ip-p}|)^2 + (|i_{op-m}| - |i_{op-p}|)^2) \tag{3.11}$$

The UBM extraction procedure summary is:

1. Measure the CM inverter impedance in the system.
2. Experiment with CM chokes: current and impedances measurements.
3. Experiment with CM shunts: current and impedances measurements.
4. Optimization.

3.3 Model extraction based on SiC MOSFET inverter with 20 kHz switching frequency

With the procedures illustrated, the UBM for the SiC MOSFET inverter is shown in Figure 3-11. The schematic diagram is shown in Figure 3-4, and is extracted with working conditions shown in Table 3-1. The copper sheet is connected with the CM ground terminal of LISN, and then full contact is made with the steel setup. There is a 5 nF MKP capacitor connected between the neutral point of the load and the ground. In order to measure input CM noise, the positive and negative conducting wire should go through the current probe at the same time. All three output wires will flow through the output current probes (Figure 3-12). The probes are carefully calibrated before the experiments. The oscilloscope is working with the configuration shown in Table 3-2. The objective for this section is to assess the capacity of the UBM technique to capture the high frequency noise of a SiC-based power converter.

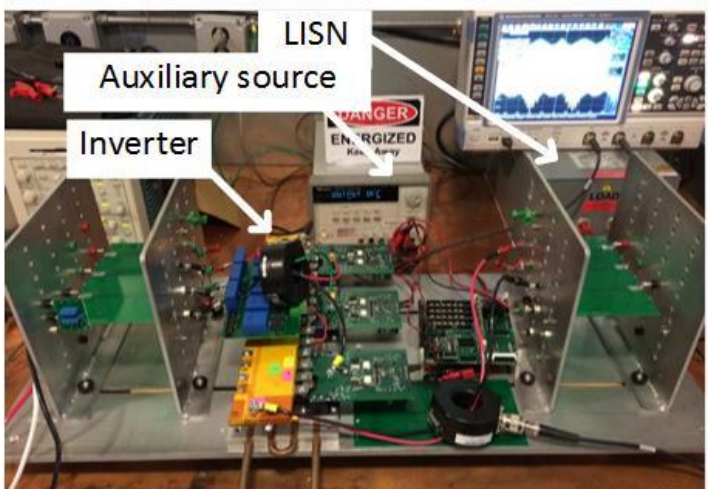

Figure 3-11 SiC inverter experimental setup

Table 3-1 SiC inverter setup configuration for 20 kHz switching frequency

Input voltage	300 Vdc
Input current	10 A
Output current	16 Arms
Resistor in the load	3.3 Ω
Inductor in the load	0.3 mH
Switching frequency	20 kHz

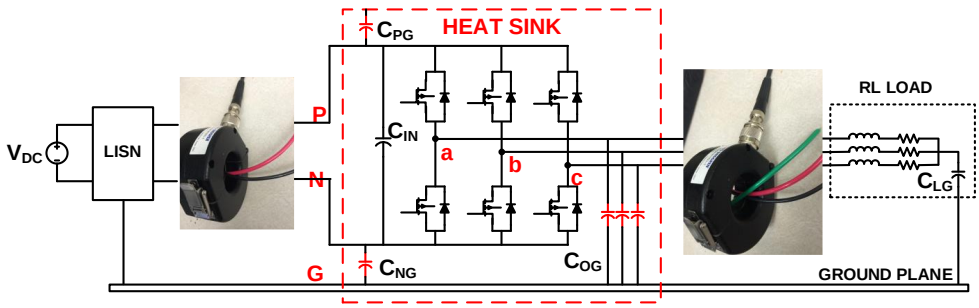

Figure 3-12 Probe placement in CM noise measurements

Table 3-2 The oscilloscope configuration

Sampling rate	500 Mp/s
Time scope	-5 ms ~ 5ms
Terminal resistance	50 Ω
Data point	5000032

3.3.1 Inverter impedance measurement

With the Agilent 4294A impedance analyzer, the inverter impedances Z_{11} and Z_{22} are first measured in the power off condition as shown in Figure 3-13. Z_{11} is the impedance between Terminal N_2 and Terminal G; Z_{22} is the impedance between Terminal N_3 and Terminal G. The two measurements as shown in Figure 3-13 have the same capacitive impedance up to MHz, in accordance with the analysis in Section 3.2.1 showing that Z_{11} is approximately equal to Z_{22}. Above 4 MHz, there is a difference between Z_{11} and Z_{22} due to the different parasitic components in the two loops.

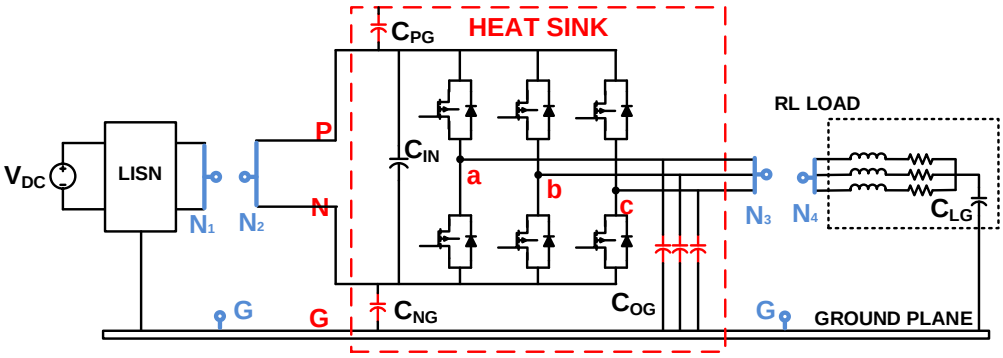

Figure 3-13 Impedance measurement method

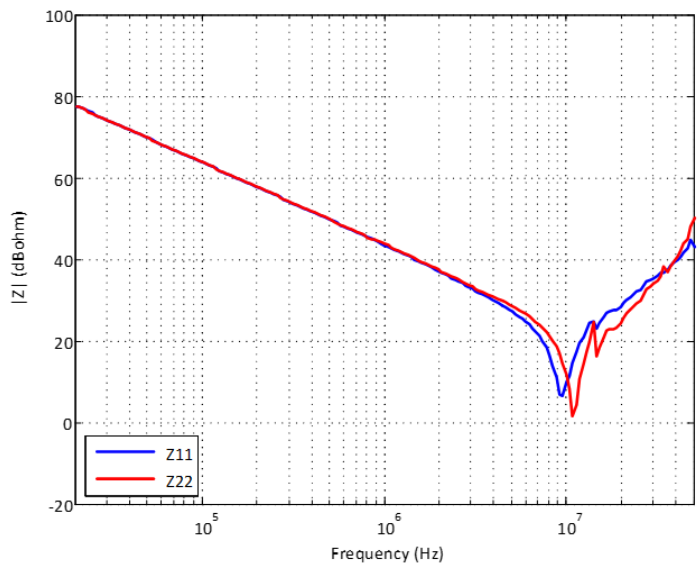

Figure 3-14 Inverter impedance measurements

The input and output impedances for one validation case are shown in Figure 3-15. The green line refers to the CM LISN impedance from Terminal N_1 to Terminal G in Figure 3-13; the black line describes the CM propagation through load (Terminal N_4) to the ground (Terminal G).

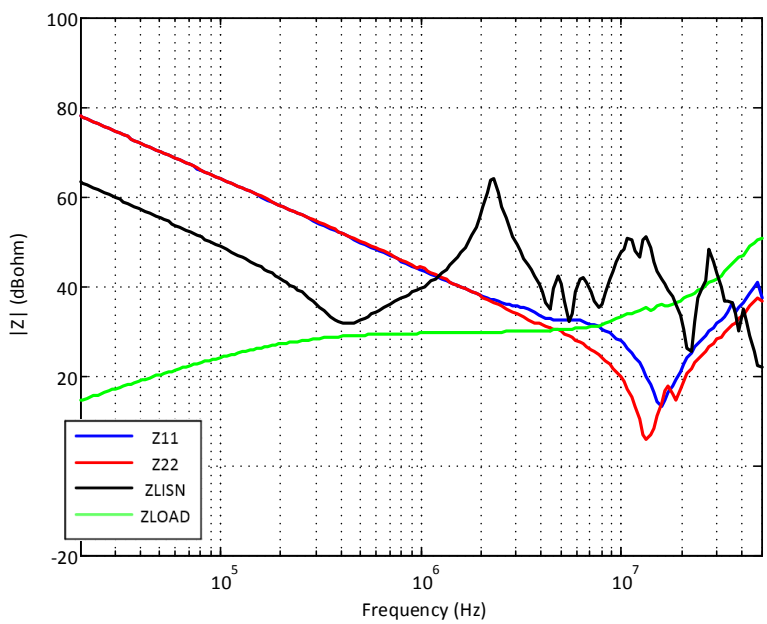

Figure 3-15 The input impedance and output impedance measurements with the inverter impedances

3.3.2 Noise sources extraction in the choke case

In order to extract the noise source with (5.9), the assumption (5.8) should be tenable. At the input side, two CM chokes in series are put between the inverter and LISN. At output, one CM three-phase choke is placed between the inverter and RL load as shown in Figure 3-16. The series

impedance measurements shown in Figure 3-17 indicate that the series impedances in the outer loop are 20 dB larger than the inverter impedances from 100 KHz to 20 MHz.

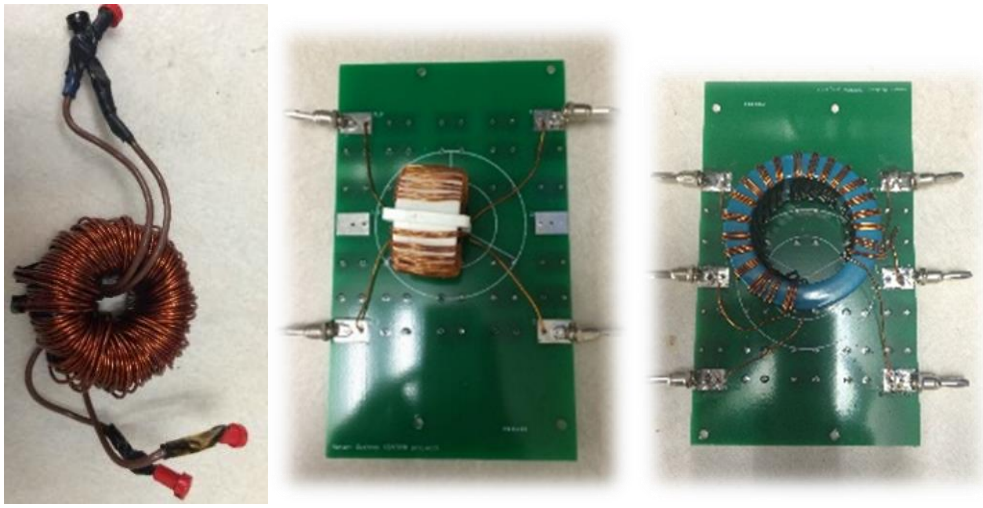

CM-input-1 CM-input-2 CM-output

Figure 3-16 CM chokes

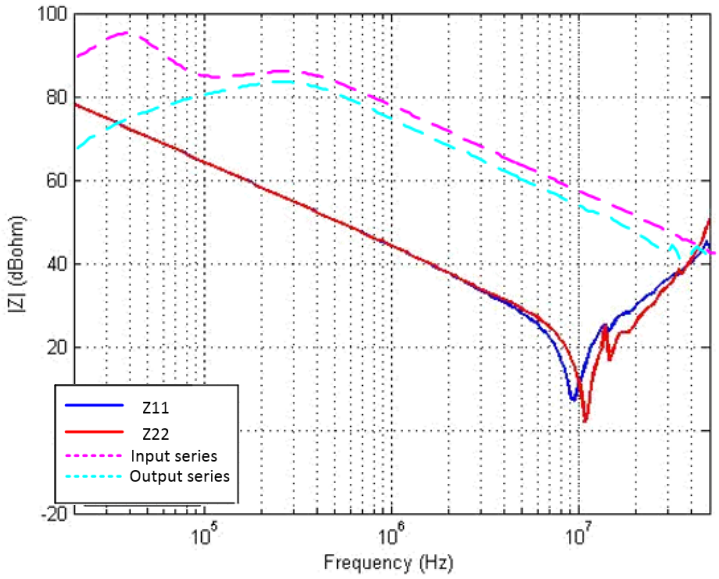

Figure 3-17 CM choke case input and output impedance with the inverter impedances

During the design of CM chokes, it is essential to make sure the inductor will not saturate in the standard working condition, and that two or three windings be twisted together in the same direction to avoid DM inductance.

Experimental current spectrums in the choke case are shown in Figure 3-18; with equation (5.8), the noise sources are calculated and exhibited in Figure 3-19.

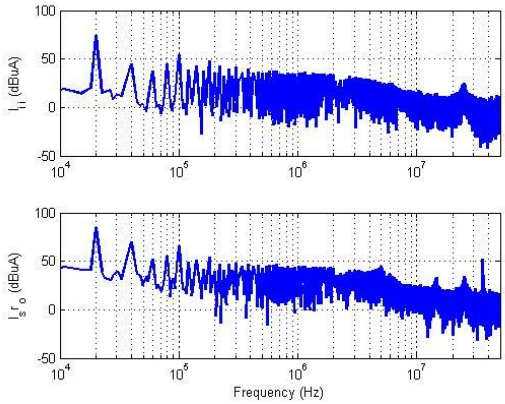

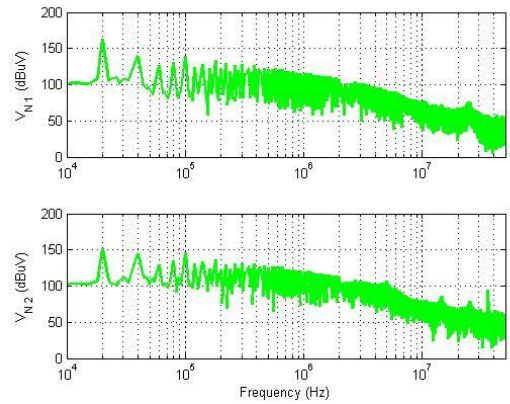

Figure 3-18 CM current spectrum in the 20kHz choke case Figure 3-19 Noise sources extracted in 20 kHz case

3.3.3 Shunt case experiments

With the noise sources and the inverter impedances, we can theoretically predict the EMI noise with different Z_i and Z_o, including the case where Z_i and Z_o are as shown in Figure 3-15. According to Equation (5.4) we can calculate i_{CMi} and i_{CMo} spectrums in this case, with results shown in Figure 3-20. There are errors above 1 MHz between the prediction and measurements. One of the reasons is the inaccurate inverter impedances. Using direct measurement with the impedance analyzer at power off condition results in the unpredictable error. Therefore, another case called 'shunt case' is performed to optimize the inverter impedances.

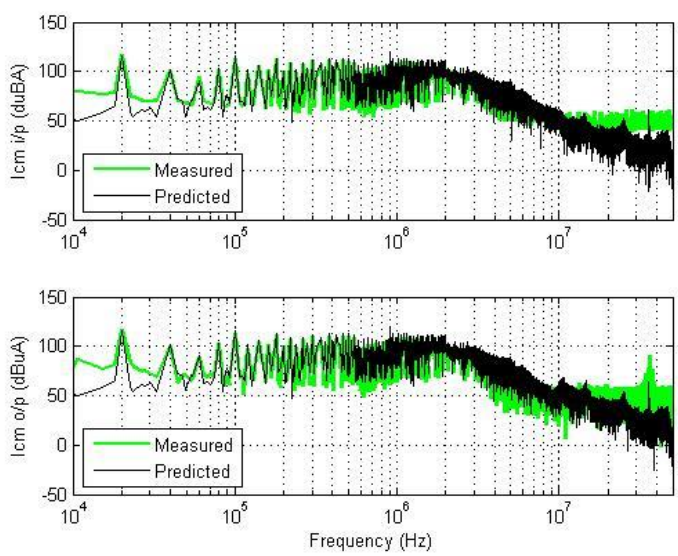

Figure 3-20 Comparison between the measurements and predictions for the validation case

Section 3.2.3 contains an explanation of how to perform a shunt case experiment. In the SiC inverter setup, the input and output shunt impedances are designed to satisfy the assumption that Z_i and Z_o are much smaller than the inverter impedances. The shunt impedance parameters and

topologies are shown in Figure 3-21. During the design, more branches are chosen for the dissipation of power and heat on the resistors. The capacitances also need careful design. If the capacitances are too small, the shunt impedance may not be smaller than the inverter impedances. On the other hand, if the CM noises are too large, the resistors cannot bear them. The measurement for the total input and output impedances are shown in Figure 3-22, where Z_i and Z_o are smaller than Z_{11} and Z_{22} below 7 MHz.

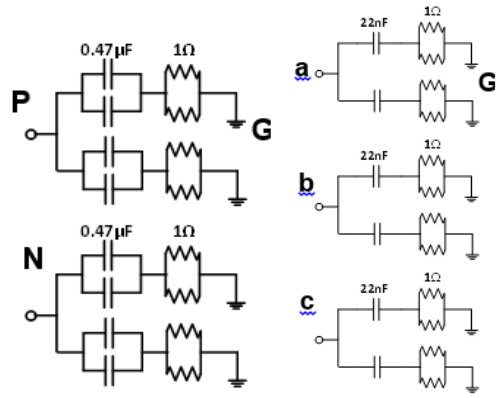

Figure 3-21 Input shunt (left) and output shunt (right) impedance parameters and topologies

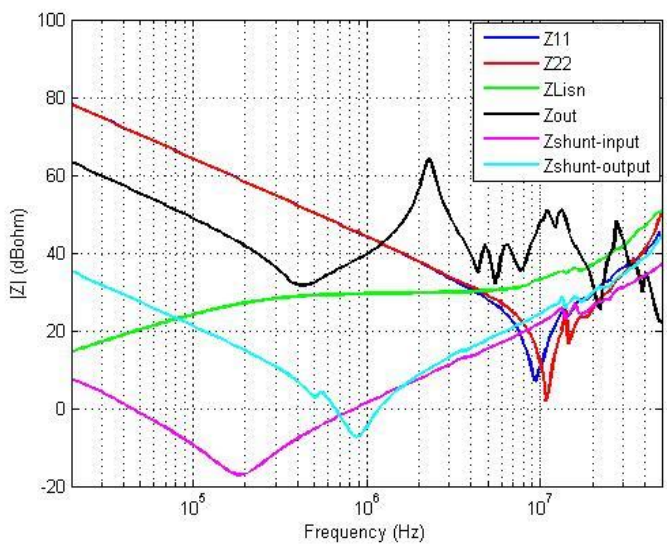

Figure 3-22 Total input and output impedances in the shunt case

The experimental current spectrums are measured and compared with the model prediction in Figure 3-23, where large errors exist in the whole EMI range and need optimization of minimization.

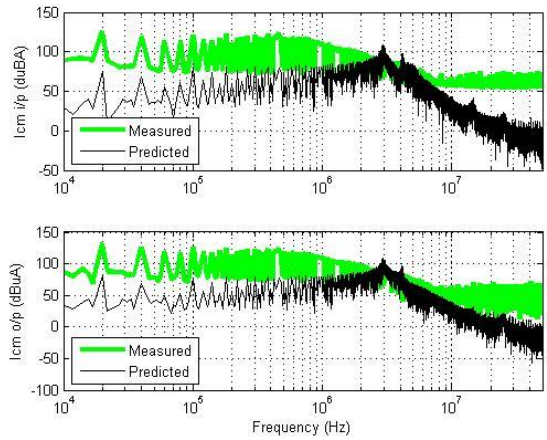

Figure 3-23 Comparison between the measurements and predictions for the shunt case

3.3.4 Optimization

Optimization is performed by Matlab with the optimization function 'fminsearch' focusing on the minimum value $((|i_{ip-m}|-|i_{ip-p}|)^2+(|i_{op-m}|-|i_{op-p}|)^2)$ search with several variables of the inverter's impedances. i_{ip-m} and i_{op-m} are the shunt case current measurements. i_{ip-p} and i_{op-p} are predictions from the UBM. The process of 'fminsearch' follows the diagram shown in Figure 3-24. From the figure of the inverter impedances (Figure 3-14), we can see that below the resonant frequency, Z_{11} and Z_{22} are capacitive, and above the resonant point they increase due to the ESL, the physical form of which are capacitors. Therefore the frequency-constant Z_{11} and Z_{22} can be simplified by branches of resistors, capacitors and inductors. In the optimization, Z_{11}, Z_{12} and Z_{22} are expressed in (5.12), where R_i reflects the resistor, L_i the inductors and C_i the capacitors. R_i, L_i and C_i are the real optimized variables in the 'fminsearch'.

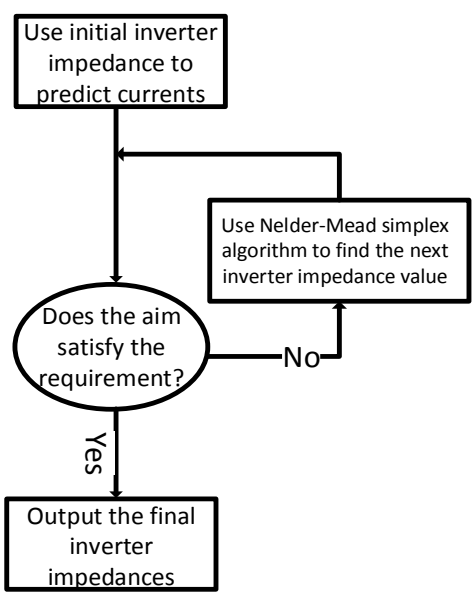

Figure 3-24 Diagram for the optimization procedures

The impedance-optimized results are shown in Figure 3-25 with new prediction current spectrums as shown in Figure 3-26. Compared with Figure 3-23, the error between the measurements and the predictions are smaller. And in the model validation case in Figure 3-27, with Z_i and Z_o measured in Figure 3-15, the UBM can predict the CM EMI noise up to 5 MHz. In practice, it is better to count the frequency error before the noise floor; this will be explained in a later section.

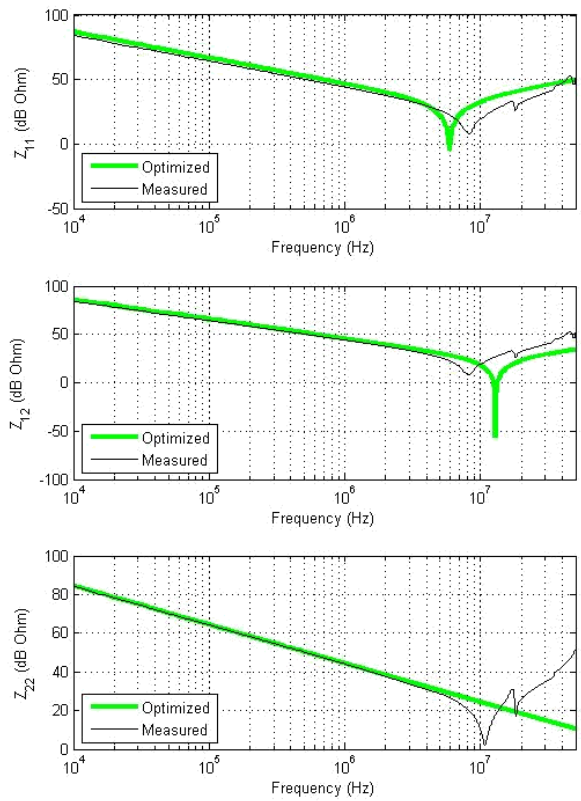

Figure 3-25 Comparison of the measured and optimized impedance in 20 kHz case

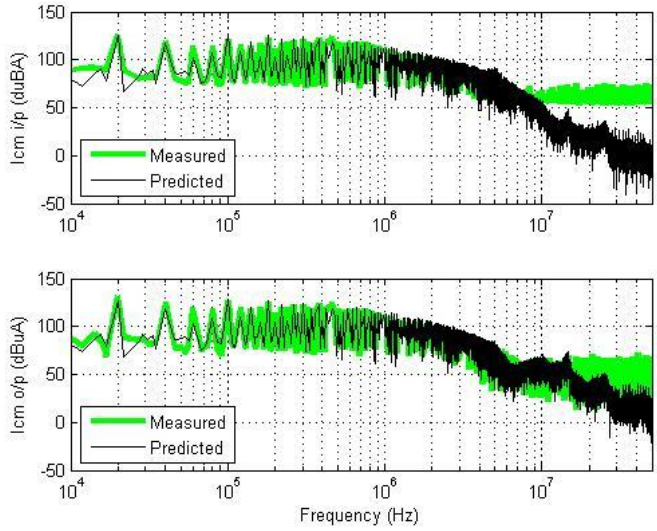

Figure 3-26 Comparison between the measurements and the predictions with the optimized inverter impedance in 20 kHz shunt case

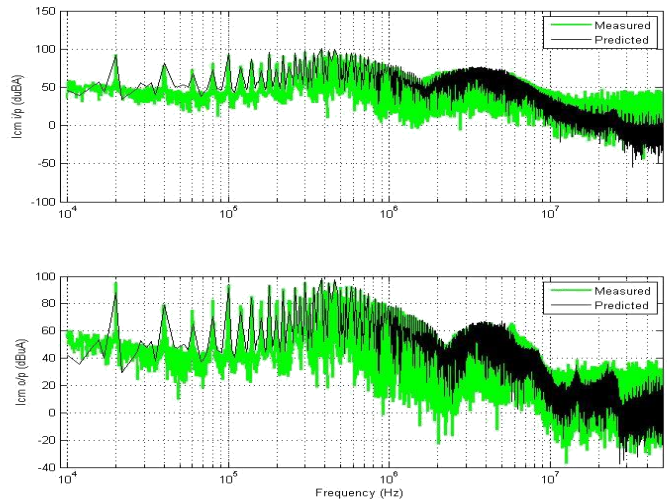

Figure 3-27 Comparison between the measurements and the predictions with the optimized inverter impedance in the 20 kHz validation case

One of the benefits of the Nelder-Mead simplex algorithm is that it can always converge to a non-stationary point, which means it can always find a minimum point. However it's not clear whether the simplex converges to the same point and it's confusing when and if the optimization is completely finished. As the Nelder-Mead simplex algorithm is implemented in the function of 'fminsearch,' the detailed optimization process is out of human control. This results in the possibility that the optimization does not minimize the error to the minimum due to the fact that the configuration parameters are not perfect.

With several trials in the optimization with different configuration parameters, the function evaluation/iteration number is ideally 5000/5000. This larger number may hold for much longer, which is not comparable with the contribution it makes.

3.4 Model extraction based on SiC MOSFET inverter with 70 kHz switching frequency

3.4.1 Model extraction in the 70 kHz switching frequency case

In this section, the SiC MOSFET inverter is working with 70 kHz switching frequency. When the EMI noise is compared with different switching frequencies, the faster the switching speed is, the larger the EMI noise is. So the objective here is to find the prediction capacity of the UBM working with higher switching frequency. The standard working condition in this case is listed in Table 3-3, where the power is somewhat reduced. Because the two switching frequency cases are sharing the same dead time setting circuit, the dead time is the same. Therefore the duty cycle range of the 70 kHz case will be smaller, causing larger harmonics at the output. The space vector pulse width modulation centered 3-Φ-C is adapted for the two cases.

Table 3-3 SiC inverter setup configuration for 70 kHz switching frequency

Input voltage	300 Vdc
Input current	8 A
Output current	10 Arms
Resistor in the load	3.3 Ω
Inductor in the load	0.3 mH
Switching frequency	70 kHz

In order to extract the model, the inverter impedances, which are dependent on the parasitic capacitors from the inverter to the ground, are measured first. In the 70 kHz case, the setup placement is the same as that of the 20 kHz case. Therefore Z_{11}, Z_{12} and Z_{22} measured at power-off condition are always the same for the different switching frequency cases, as are Z_i and Z_o in any cases with or without extra impedance inserted. This is because the impedances are independent of the switching behavior and rely on the parasitic distribution. As a result, in this section, all the measured impedances used are the same as in the 20 kHz case.

However, the real inverter impedance in the power-on condition should be different from the ones in the 20 kHz case due to their reliance on the switching actions; the same is true for the noise sources in the 70 kHz UBM. As a result, in the choke case, the experiment to calculate the sources, and the shunt case, the experiment related to the real inverter impedances should be performed again in the 70 kHz standard working condition.

Figure 3-28 shows the current spectrums in the choke case, and with Equation (5.8), the equivalent noise sources are calculated and shown in Figure 3-28. With these sources and with

measured inverter impedances, the shunt case current spectrum can be predicted again and compared with the measurements in Figure 3-30. The same optimization process is performed based on the error between the measurements and predictions in the 70 kHz shunt case. With the optimized impedance in Figure 3-32, the shunt case current spectrum can be predicted again in Figure 3-31. Furthermore, the 70 kHz validation case spectrums are predicted with the new model in Figure 3-33. In this model, the UBM implies a good prediction up to 5 MHz.

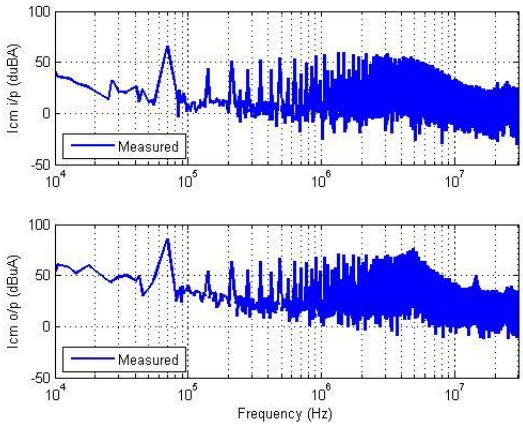

Figure 3-28 CM current spectrum in the 70 kHz choke case

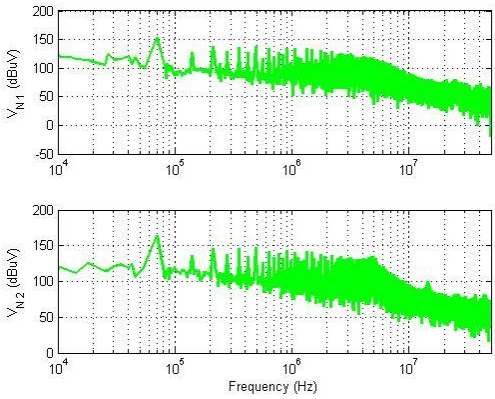

Figure 3-29 Noise sources extracted in 70 kHz case

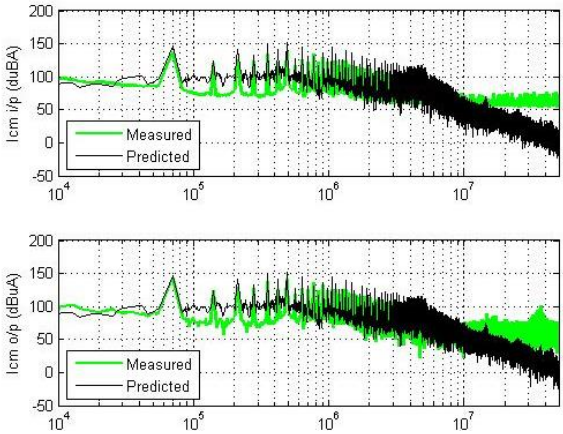

Figure 3-30 Comparison between the measurements and the predictions with the measured inverter impedance in 70 kHz shunt case

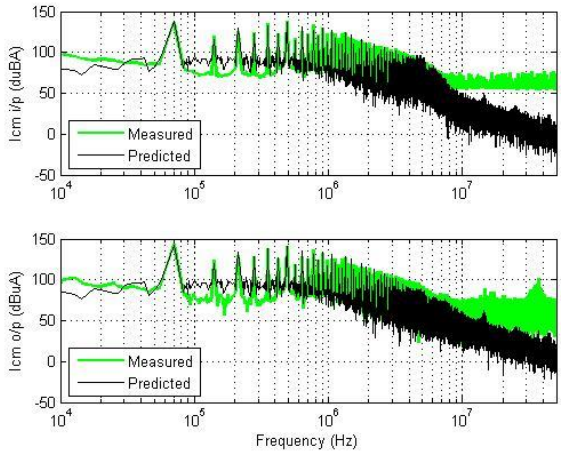

Figure 3-31 Comparison between the measurements and the predictions with the optimized inverter impedance in 70 kHz shunt case

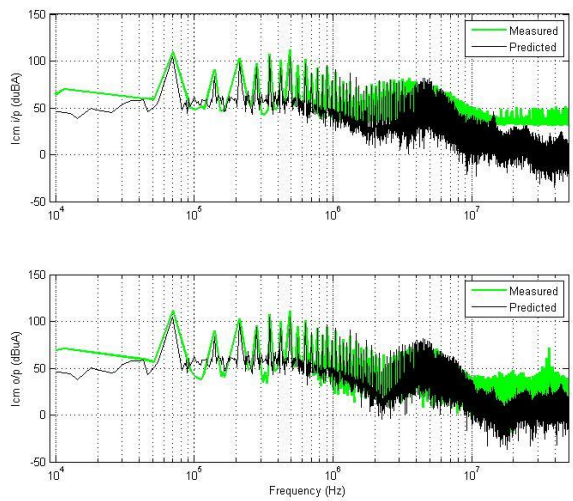

Figure 3-33 Comparison between the measurements and the predictions with the optimized inverter impedance in 70 kHz validation case

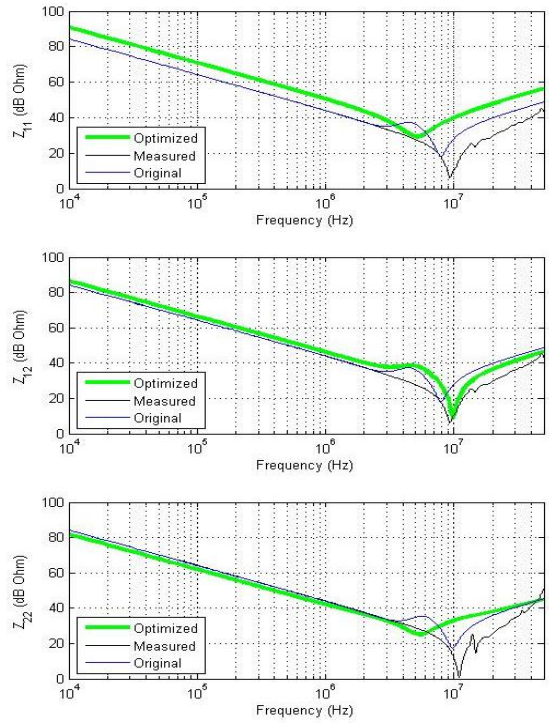

Figure 3-32 Comparison of the measured and optimized impedance in 70 kHz case

In the 70 kHz case optimization process, the two RCL branches in parallel are used to describe the inverter impedances Z_{11}, Z_{12} and Z_{22}. As this in accordance with the physical structure, this means that they are related to $Z_{C_{IG}}$ and $Z_{C_{OG}}$. Therefore, there will be six parameters to describe one impedance as seen in (5.13).

$$\tilde{Z}_{11} = \tilde{R}_1 + s\tilde{L}_1 + \frac{1}{s\tilde{C}_1}, \hat{Z}_{11} = \hat{R}_1 + \hat{s}L_1 + \frac{1}{s\hat{C}_1}, Z_{11} = \frac{\tilde{Z}_{11}\hat{Z}_{11}}{\tilde{Z}_{11} + \hat{Z}_{11}}$$
$$\tilde{Z}_{12} = \tilde{R}_2 + s\tilde{L}_2 + \frac{1}{s\tilde{C}_2}, \hat{Z}_{12} = \hat{R}_2 + \hat{s}L_2 + \frac{1}{s\hat{C}_2}, Z_{12} = \frac{\tilde{Z}_{12}\hat{Z}_{12}}{\tilde{Z}_{12} + \hat{Z}_{12}} \tag{3.12}$$
$$\tilde{Z}_{22} = \tilde{R}_3 + s\tilde{L}_3 + \frac{1}{s\tilde{C}_3}, \hat{Z}_{22} = \hat{R}_3 + \hat{s}L_3 + \frac{1}{s\hat{C}_3}, Z_{22} = \frac{\tilde{Z}_{22}\hat{Z}_{22}}{\tilde{Z}_{22} + \hat{Z}_{22}}$$

3.4.2 Evaluation of the EMI emission in different switching frequency based on UBM

In Section 2.2, the increased EMI emission caused by the higher switching frequency is analyzed. With the UBM of the 20 kHz and 70 kHz switching frequency cases, we can find the reason for the increase from the model.

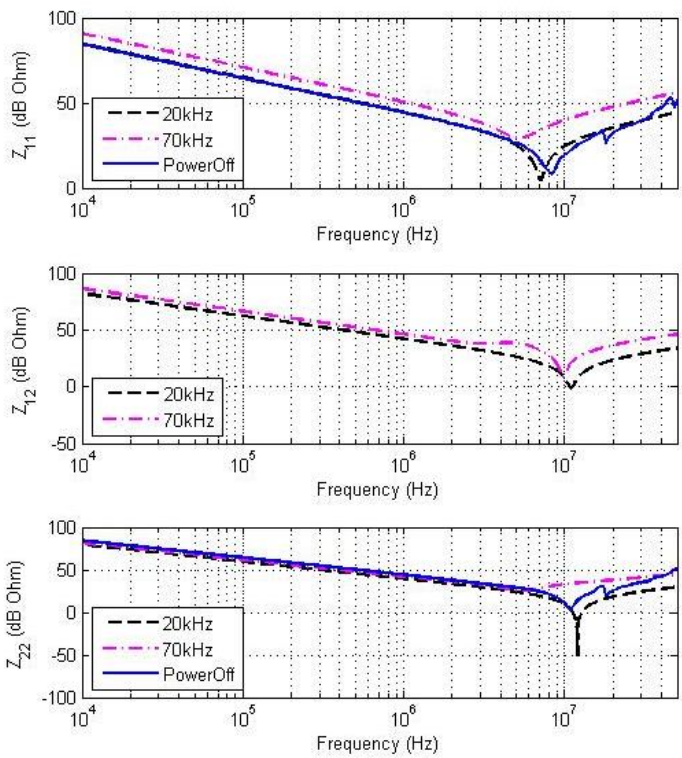

Figure 3-34 Z-matrix result after model extraction of 20 kHz and 70 kHz switching frequency cases.

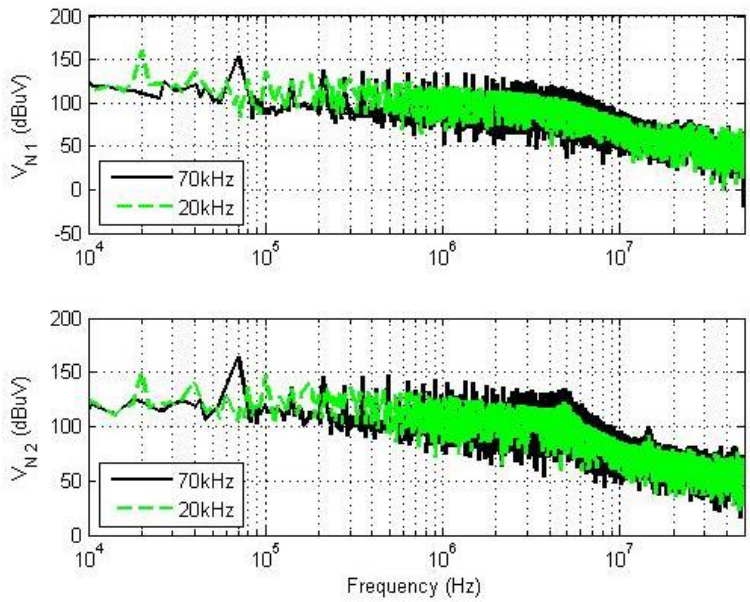

Figure 3-35 Noise source results after model extraction of 20 kHz and 70 kHz switching frequency cases.

3.5 Re-designed shunt impedance and improved measurement fixture

In the validation case in the 20 kHz and 70 kHz cases, the predicted spectrums can only match the measured spectrums up to 5 MHz. The main reason is the ineligible shunt impedance in the shunt case experiment. Recall that the measured input and output impedances in the shunt case in Figure 3-22, Z_i and Z_o do not satisfy the assumption (5.10) ($\begin{matrix} Z_i \ll Z_{11}, Z_{12} \\ Z_o \ll Z_{22}, Z_{12} \end{matrix}$) above 5MHz. Above 5 MHz, Z_i and Z_o are comparable with Z_{11} and Z_{22}. Therefore, the information about Z_{11}, Z_{12} and Z_{22} above 5 MHz is lost in the optimization. In order to expand the prediction capacity, better shunt impedances are needed with smaller high frequency impedances.

One general way to reduce shunt impedance is by adopting larger capacitance. As a result, the CM noise or current will increase, and so series resistors with more power should be chosen. Or more resistors with larger resistance in parallel could be used. It is also beneficial to use components in parallel rather than in series, because the series connection causes extra equivalent series inductance (ESL), which is the main component above the resonant frequency. The series resistors are used here to make the impedance flat in case the impedance at the pit of the resonant frequency is too small.

3.5.1 Improving the capacitance and the series resistance in the shunts

In Table 3-1, different shunt topologies for the output side are listed, and corresponding impedances inserted into the setup are measured in Figure 3-36. Results show that with larger capacitance, the impedance at low frequency is reduced. However, above the resonant frequency point, the impedance is smaller with the smaller capacitance. The tendency of the impedance to

change above resonant frequency is in accordance with the series resistance. Hence, the smaller resistance is chosen to see whether the high frequency impedance will be reduced or not.

Table 3-4 Different output shunt topologies with different capacitances

No.	C/nF	R/Ω	Circuit for one terminal
1	45	0.25 THR	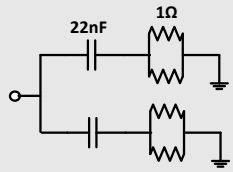
2	22	1.5 chip	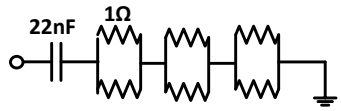
3	9.5	2 chip	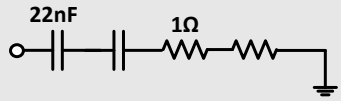

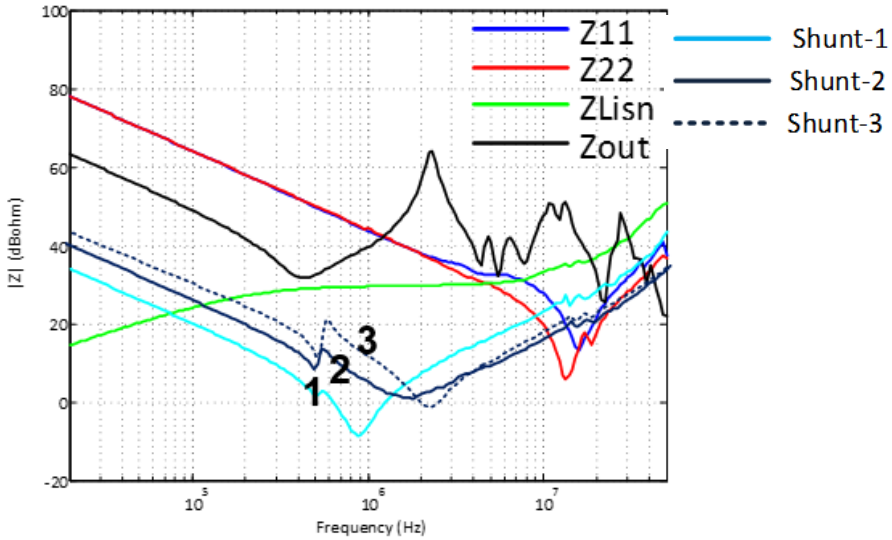

Figure 3-36 Output shunt impedances for the different output shunt topologies

At the input sides, the series impedances change with the constant capacitance, which are listed in Table 3-5. Their corresponding input shunt impedances are drawn in Figure 3-37, where Case 2 and 3 have the same ESL. As noted, the impedance above 6 MHz cannot be further reduced. This indicates that the main ESL above 5 MHz is integrated in the setup or measurement fixture, and therefore needs reduction.

Table 3-5 Different input shunt topologies with different resistance

No.	C/μF	R/Ω	Circuit for one terminal
1	1.9	0.25	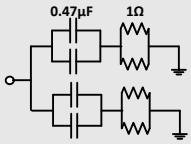
2	1.9	0.5	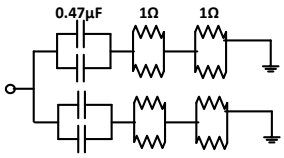
3	1.9	1	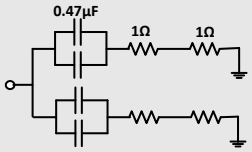

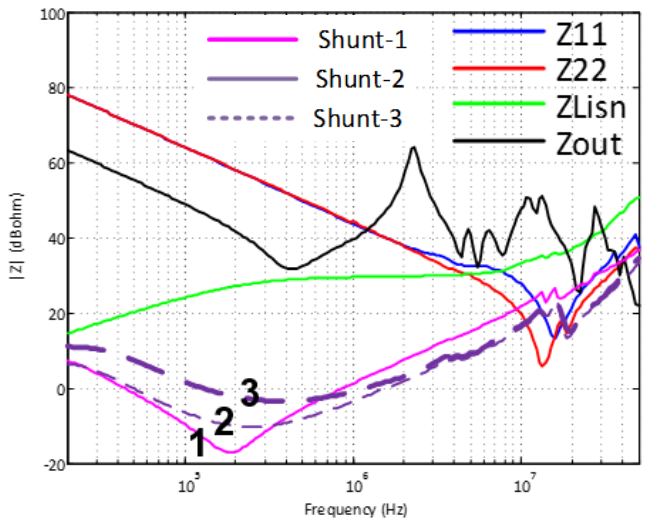

Figure 3-37 Input shunt impedances for the different input shunt topologies

3.5.2 Measurement fixture improvement

Figure 3-38 shows the measuring moment of the input shunt, which corresponds with Figure 3-39. The input shunt is surrounded in both green frames in the two figures. The orange squares are trapping the measurement fixture (two banana conducting wires), with which the positive and negative terminal of input can be short-circuited to one point (green banana socket in Figure 3-39). The impedance analyzer will measure from the green banana socket to the steel plate (ground) as Z_i in the shunt case. However, the banana conducting wires have large ESL themselves, as shown in Figure 3-40, where the impedance is 4.69 Ω at 10 MHz. Compared with the total impedance at 10 MHz, which is 7.05 Ω, the conducting wires cause too much ESL and need replacement.

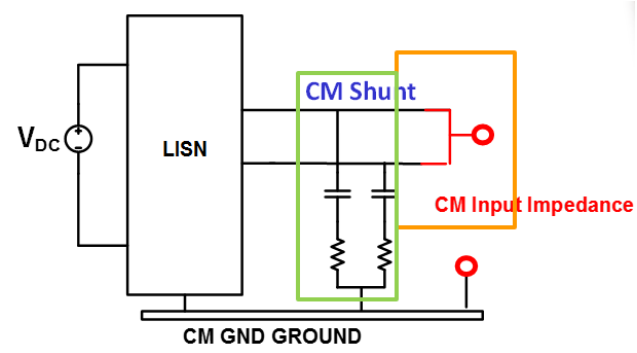

Figure 3-38 Input shunt measurement fixture schematic diagram

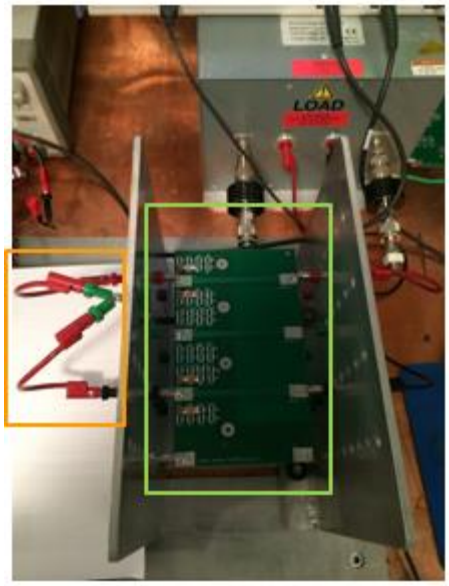

Figure 3-39 Input shunt measurement fixture

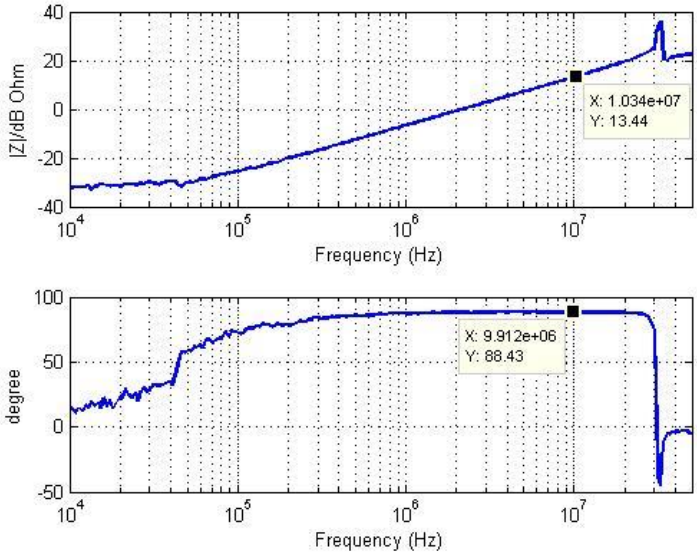

Figure 3-40 Banana conducting wire impedance

A three-terminal connection fixture is fabricated with smaller ESL, as shown in Figure 3-41, with its impedance measured from any two terminals in Figure 3-42, where the impedance is 0.58 Ω at 10 MHz, 10 times smaller than the original method. The fixture can be placed at the input or output side instead of the banana conducting wires.

Figure 3-41 Designed short-circuit fixture

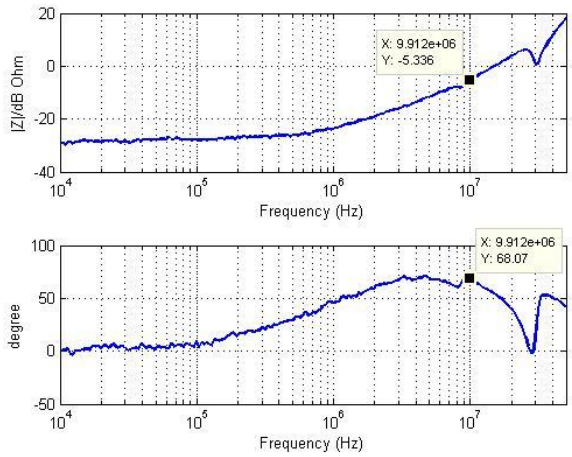

Figure 3-42 Designed short-circuit fixture impedance

3.5.3 Shunt PCB improvement

In addition, the connections to the shunt boards are tested. Figure 3-43 shows an amplification of one corner of the input shunt PCB board, where the (right) banana connector is wielded on the one joint sheet on the PCB (GND copper sheet in the Figure 3-44). This joint is connected to the back of the board through a via hole, which is the ground of the PCB. Generally, the via hole will contribute extra ESL in the loop. This phenomenon is verified with the measurement performed as shown in Figure 3-44. The input shunt will be taken into several parts, each of which is measured to find the biggest ESL contributor.

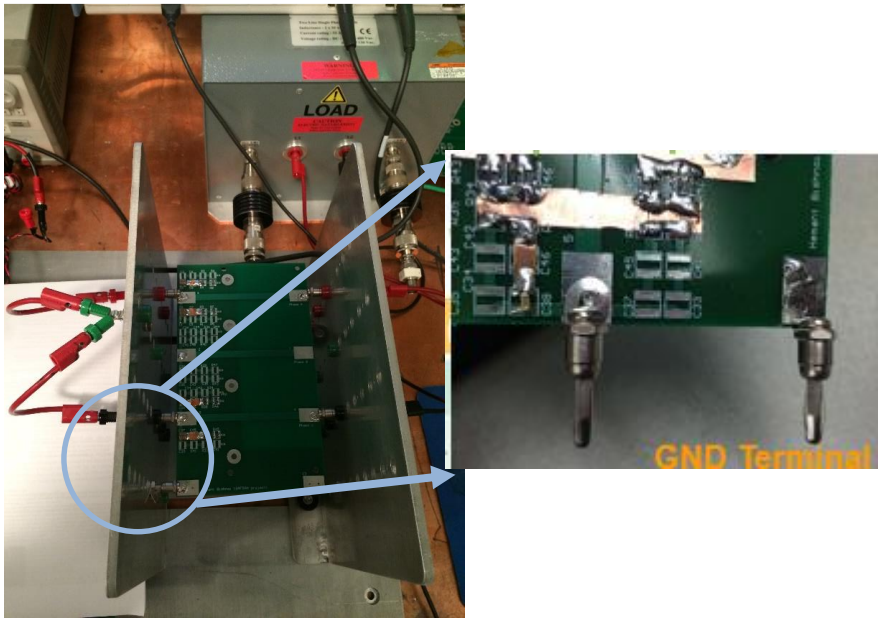

Figure 3-43 Detailed input shunt PCB connection

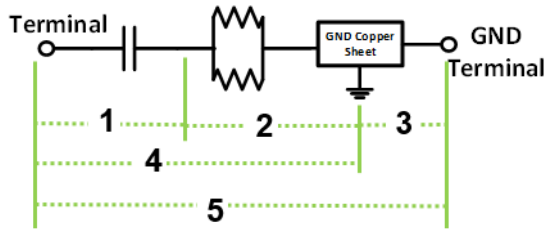

Figure 3-44 Separation of the input shunt in one branch

Table 3-6 lists the measurement of the separate parts in the input shunt PCB. Obviously Case 2 has the biggest real part. However, the ESL part is integrated in Case 3 where the impedance degree is close to 90 with quite a large magnitude. Therefore, the via hole connection needs to provide avoidance. Finally, the banana connection for GND is directly welded on the back of the shunt PCB. The same improvements are made for the output shunt PCB.

Table 3-6 Comparison of the measurement for different parts of the input shunt in one branch

@10MHz	Magnitude (Ω)	ϑ(Degree)	Real part (Ω)
1	1.84671	-85.8278	0.248
2	1.37918	7.119926	1.368
3	1.51067	76.2766	0.494
4	1.52772	-0.3717377	1.52
5	5.71314	82.5155	0.74

3.5.4 Improved shunt impedance and the updated UBM results

With the improvement in the shunt PCB and the measurement fixture, the new shunt impedances measurements are exhibited in Figure 3-45 for comparison with the original shunt impedances. In this way, the shunt impedances are smaller than the inverter impedances more than 10 dB apart from the 10 MHz point, and 20 dB smaller below 8 MHz. With this new shunt measurement and the shunt case measured spectrums, the optimization can be performed and the validation is predicted to assess the positive effect from this developer.

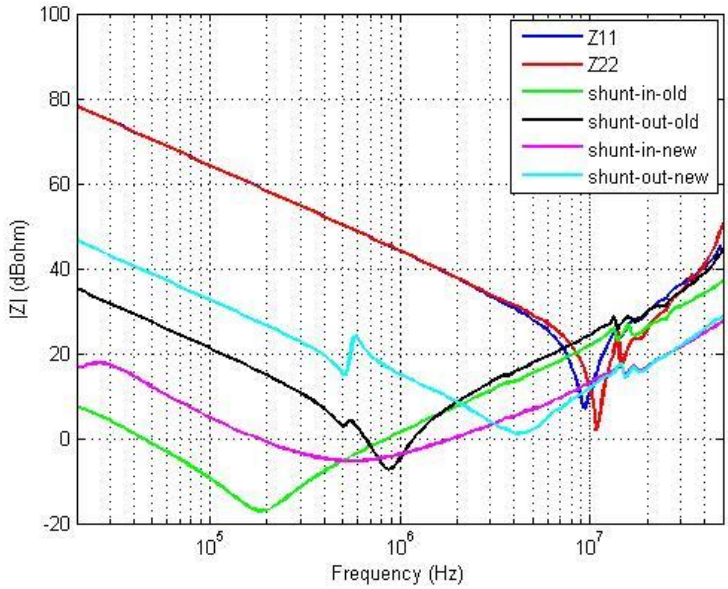

Figure 3-45 Comparison between the original and new shunt impedance measurements

First, compare the new prediction before optimization in Figure 3-46 with the original in the shunt case shown in Figure 3-23. The new result gets a better match thanks to the clarified shunt impedance measurement. The original shunt impedances used in the prediction are larger than the real ones. Actually, the clarified shunt case can give a pretty good prediction already, relieving the pressure on the optimization. Comparing the new prediction in the shunt case shown in Figure 3-47 with the original one shown in Figure 3-26, the new prediction results match the measurements better. Take the validation as the final comparison: the new results (Figure 3-48) for the 20 KHz case imply good prediction to 10 MHz and the results for the 70 kHz case (Figure 3-49) expands the UBM prediction capacity to 10 MHz, as opposed to the original prediction capacity, which was 5 MHz.

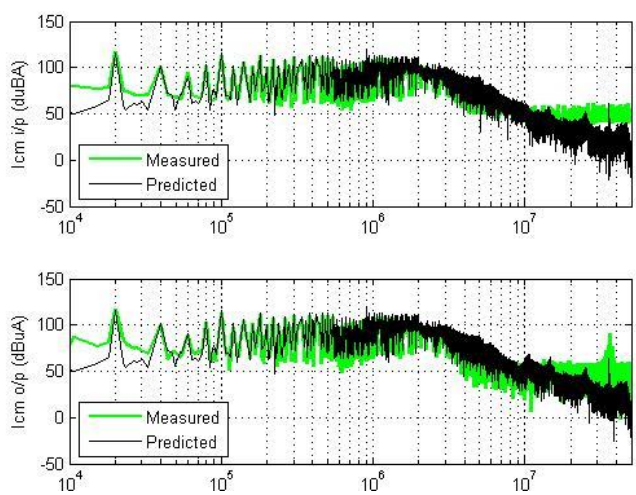

Figure 3-46 Comparison between the measurements and predictions for the 20 kHz shunt case with clarified shunt impedances

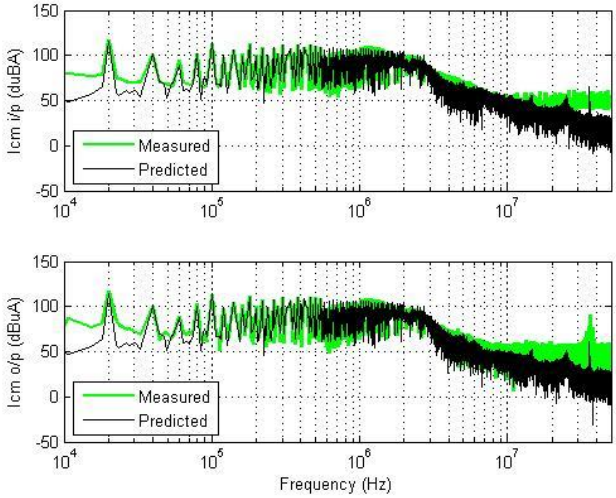

Figure 3-47 Comparison between the measurements and predictions after optimization for the 20 kHz shunt case with clarified shunt impedances

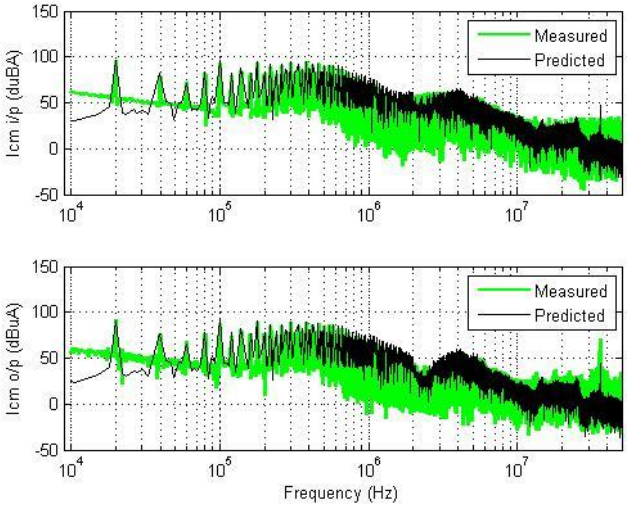

Figure 3-48 Comparison between the measurements and predictions for the 20 kHz validation case with clarified shunt impedances

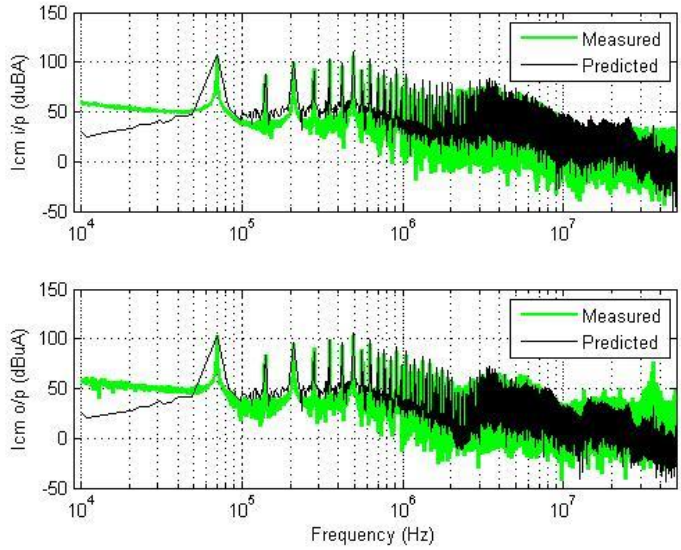

Figure 3-49 Comparison between the measurements and predictions for the 70 kHz validation case with clarified shunt impedances

3.6 Noise floor issue and its developer

3.6.1 Origin of the noise floor issue and its effect on the UBM

For now, the UBM prediction capacity is limited to 10 MHz. The limitation to further improvement is called the noise floor. Focusing on the spectrums above 10 MHz from Figure 3-47 to Figure 3-49, we can see that they are flat as a floor, which is caused by the limited vertical resolution of the oscilloscope.

The general method to perform an EMI behavioral model is based on some measured current or voltage spectrums. The oscilloscope is needed to capture the time domain waveform with high sampling frequency (100 MHz at least). During the experiment, the vertical resolution is adjusted to trap the waveform in the oscilloscope screen as the system can only restore the data within the screen. The smaller vertical resolution is determined by the largest peak in the waveform. The smallest signal captured is limited by the chosen vertical resolution. For example, the oscilloscope working with the experiment — RTO 1014 from Rohde & Schwartz — has a single-core architecture for AD (analog to digital) transformation with more than seven effective bits (128) (Figure 3-50[48]), which is fairly high compared to the oscilloscope currently on the market, which has a 1G sampling frequency. (The higher sampling frequency oscilloscope has smaller effective bits in the AD.) Figure 3-51 from the scope manual also shows the claim that the noise floor, the smallest signal the scope can capture, will increase with the increased vertical sensitivity (also as vertical scale). Moreover, if the sensitivity increases to 10 times larger, the noise floor will increase 10 times (20 dB), which is experimentally verified in Figure 3-52 by taking measurements with different vertical scales on the same signal.

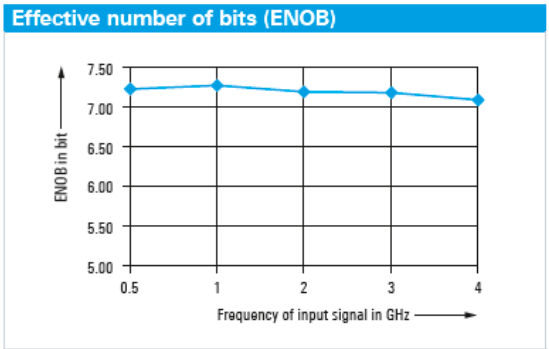

Figure 3-50 RTO 1014 effective bits with input frequency [48]

RMS noise floor at 50 Ω (typ.)	input sensitivity	R&S®RTO1002, R&S®RTO1004	R&S®RTO1012, R&S®RTO1014
	1 mV/div	0.08 mV	0.10 mV
	2 mV/div	0.08 mV	0.10 mV
	5 mV/div	0.11 mV	0.12 mV
	10 mV/div	0.17 mV	0.20 mV
	20 mV/div	0.28 mV	0.36 mV
	50 mV/div	0.70 mV	0.85 mV
	100 mV/div	1.30 mV	1.65 mV
	200 mV/div	2.70 mV	3.30 mV
	500 mV/div	7.00 mV	8.70 mV
	1 V/div	13.7 mV	17.0 mV
	input sensitivity	R&S®RTO1022, R&S®RTO1024	R&S®RTO1044 (meas.)
	1 mV/div	0.15 mV	0.24 mV
	2 mV/div	0.15 mV	0.25 mV
	5 mV/div	0.18 mV	0.28 mV
	10 mV/div	0.28 mV	0.42 mV
	20 mV/div	0.50 mV	0.72 mV
	50 mV/div	1.22 mV	1.80 mV
	100 mV/div	2.39 mV	3.60 mV
	200 mV/div	4.80 mV	7.20 mV
	500 mV/div	12.0 mV	18.0 mV
	1 V/div	23.9 mV	36.0 mV

Figure 3-51 Vertical system noise floor of RTO oscilloscope

In Figure 3-52, the spectrums in ‘1 V/div’ are 20 dB higher than those in ‘100 mV/div’ at one fixed frequency point. The larger the vertical scale, the larger the smallest measured signal is and the higher the noise floor is. In the shunt case with the largest CM spectrum of all the cases, the noise floor issue is more serious. Figure 3-53 compares the CM current spectrums in the 20 kHz and 70 kHz shunt case. For the 20 kHz case, the spectrum decreasew with the increased frequency up to 6 MHz, where the spectrum touches the noise floor and tends to be flat. The real spectrum above 6 MHz is hidden by the noise floor. As for the 70 kHz case, where the spectrum is higher than that of 20 kHz case, the noise floor starts at 8 MHz at the input side. However, the noise floors in the 20 kHz and 70 kHz input spectrums all start at around 70 dBμA, owing to the same scale during the two experiments. At 6 MHz, the 20 kHz input spectrum reaches 70 dBμA. However, at the same point, the 70 kHz input spectrum has a larger magnitude and touches 70 dBμA when it goes to 8 MHz. As for the output spectrum, the noise floor of the 70 kHz case also starts from 6 MHz, which is the same as that of the 20 kHz case, due to the larger vertical scale it uses compared that of the 20 kHz case. The 20 kHz output spectrum touches the noise floor with a magnitude around 70 dBμA. Though the 70 kHz case has a larger spectrum in the whole range, the noise floor

for the 70 kHz output spectrum starts with a magnitude around 80 dBμA, as the larger the scale it uses, the higher the noise floor will be.

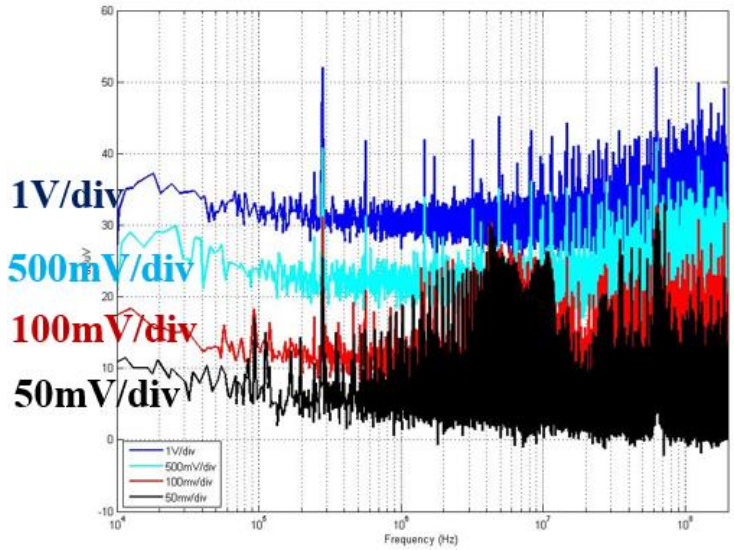

Figure 3-52 Comparison the spectrum measurements with different vertical scales on the same signal

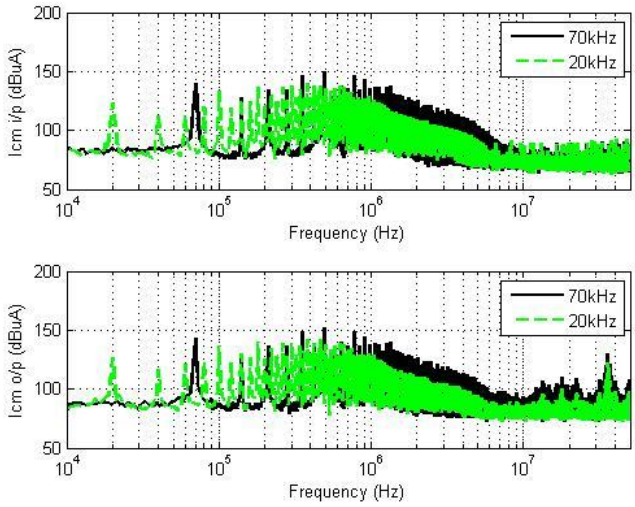

Figure 3-53 Comparison of CM current spectrums in 20 kHz and 70 kHz shunt case

A similar issue also exists in the validation case but not in the series case. Recalling the series case spectrum in Figure 3-18 (20 kHz case), and Figure 3-28 (70 kHz case), the noise floor starts above 30 MHz. As a result, in the shunt and validation case, or any other case with the noise floor issue below 30 MHz, there exists the need for an effective solution.

3.6.2 Developer: segmented frequency range measurement with high-pass filter

In order to find the spectrum below the noise floor, one possible solution is to use a smaller vertical scale to measure the spectrum, which is determined by the highest peak of the spectrum. If a high-pass filter is connected between the current probe and the oscilloscope, the spectrum with the highest peak can be effective to a higher frequency with the lower noise floor using a smaller vertical scale.

A. Spectrum measured with high pass filter

In order to certify the feasibility of the filter as a solution to the noise floor issue, several experiments are performed with a 5 MHz high-pass filter and a 10 MHz high-pass filter. The C-L-C high-pass filters are designed with simulation software called Filter Free 2014 from Nuhertz Technologies, whose topologies and parameters are shown in Figure 3-54 and Figure 3-55, along with some design characteristics in Table 3-7. The transfer gain measured with a network analyzer for the fabricated filters are shown in Figure 3-56, in accordance with the simulation results.

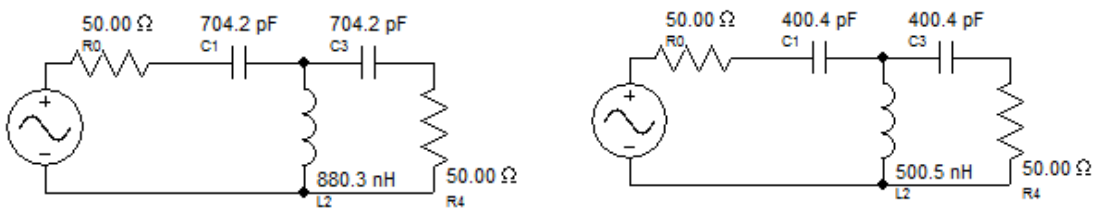

Figure 3-54 Topologies and parameters of 5 MHz (left) and 10 MHz (right) high-pass filter

Figure 3-55 Fabricated filters of 5 MHz (left) and 10 MHz (right) high-pass filter

Table 3-7 Design characteristics of the high-pass filter

High-pass Filter Design	5 MHz	10 MHz
Pass band frequency	4.52MHz	10.2MHz
Pass band Attenuation	3.01 dB	3.01 dB
Impedance	50 Ohm	50 Ohm
Topology order	3rd	3rd

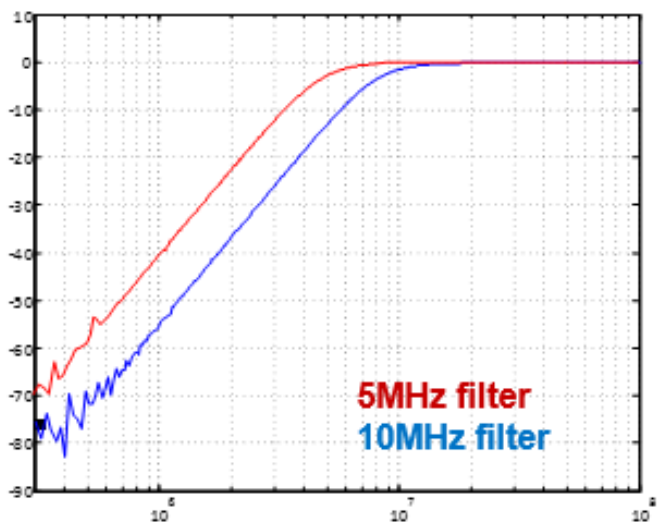

Figure 3-56 Measured transfer gain for the high-pass filters

Two filters are then inserted between the current probe and the oscilloscope separately in the experiments. Figure 3-57 and Figure 3-58 show the spectrum without filters and with filters in the shunt cases, with the vertical scale chosen for the different conditions in Table 3-8. Take the output 20 kHz shunt case spectrum as an example. The noise floor of the spectrum without filter starts from 6 MHz with the vertical scale of 1 V/div, and the highest peak in the spectrum reaches 120 dBμA. When the 5 MHz filter is inserted, the highest peak drops to 90 dBμA. As a result, a smaller scale as 100 mV/div is chosen and the noise floor is pushed 20 dB lower, starting from 15 MHz. In the 10 MHz filter case, the highest peak is further reduced to 70 dBμA and the noise floor is pushed above 30 MHz with the vertical scale of 50 mV/div. In conclusion, the high-pass filter will help push the noise floor to a higher frequency with the smaller vertical scale in the chosen compatible oscilloscope.

In addition to the spectrum analyzer results shown in the two figures above, above 6 MHz, the 5 MHz filter results match with the results without a filter up to 10 MHz, where the noise floor starts. The 10 MHz filter helps to find the spectrum above 15 MHz up to 30MHz, where the spectrum matches that of the 5 MHz filter around 20 MHz. Hence the whole frequency range can be separated into three segments: 10 kHz ~ 6 MHz, 6 MHz ~ 15 MHz and 15 MHz ~ 30 MHz,

corresponding to the following conditions: without filter, 5 MHz high-pass filter, and 10 MHz high-pass filter.

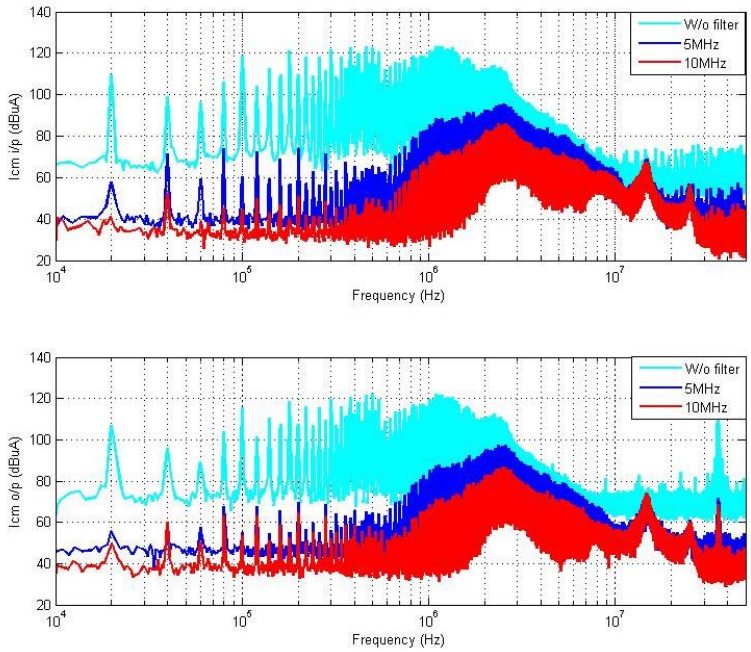

Figure 3-57 Comparison among the spectrum without filter, with 5 MHz and 10 MHz high-pass filter in the 20 kHz shunt case

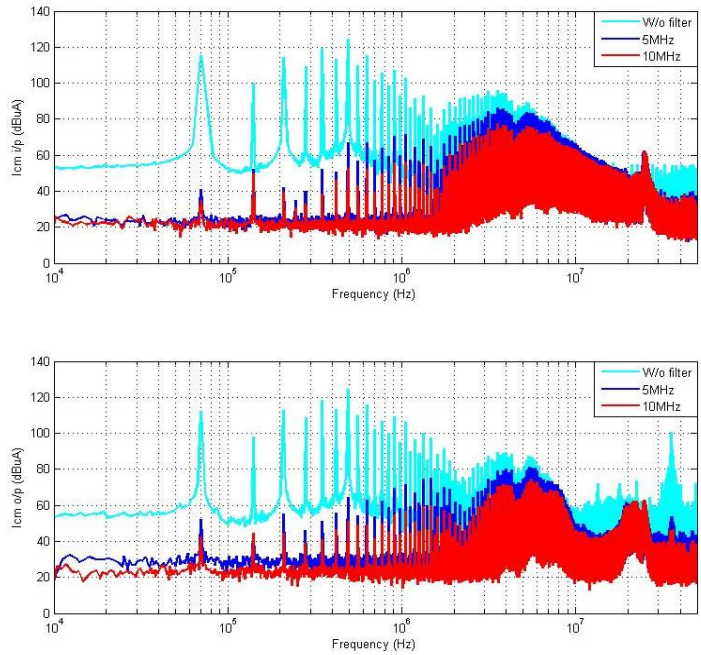

Figure 3-58 Comparison among the spectrum without filter, with 5 MHz and 10 MHz high-pass filter in the 70 kHz shunt case

Table 3-8 Vertical scale in the oscilloscope during different experiments

V/div		Validation		Shunt (*30dB)	
		input	output	input	output
20k	w/o	50m*30dB	100m*30dB	1	1
	5MHz	500m	400m	100m	100m
	10MHz	400m	200m	40m	50m
70k	w/o	100m*30dB	100m*30dB	1	1
	5MHz	500m	400m	200m	200m
	10MHz	400m	200m	50m	50m

** *30dB: 30 dB attenuation is added at the oscilloscope terminal to trap the whole waveform in the screen

B. High-pass filter cooperation with UBM

It is already verified that the spectrum can cover the whole EMI range with the help of filters if the spectrums under the three conditions can connect as one. At any rate, the filter can change the input signal magnitude and phase of both. If the phase information in the three conditions can be ignored, considering only the magnitude of the spectrum, the connection can be completed by chopping the spectrum and putting it in order after the experiments. However, the assumption that the phase can be ignored needs verification before using the segmented spectrum in UBM.

Firstly in the choke case, though there is no noise floor issue, the assumption is challenged. For example, in the choke case, the experiment without filters is performed first where the input and output currents are measured simultaneously. Then, in the same case, the input and output currents are measured separately in two experiments. The noise sources extracted in the first condition are calculated as (5.14) (or 5.4). The phases of V_{N1} and V_{N2} are aligned with those of i_{CMi} and i_{CMo} , which are aligned with each other due to the simultaneous measurement. In the second measurement, where the input and output currents are not measured at the same time, there are some unpredictable phases between the two currents. Because of this unpredictability, the two measurements are performed at the same phase point. As a result, there will be some phase delay in the calculated noise sources in (5.15).

$$\begin{bmatrix} -Z_{SRi} i_{CMi} \\ -Z_{SRo} i_{CMo} \end{bmatrix} = \begin{bmatrix} V_{N1} \\ V_{N2} \end{bmatrix} \tag{3.13}$$

$$\begin{bmatrix} -Z_{SRi} \tilde{i}_{CMi} \\ -Z_{SRo} \tilde{i}_{CMo} \end{bmatrix} = \begin{bmatrix} V_{N1} \\ V_{N2} \cdot 1\angle\theta \end{bmatrix} \tag{3.14}$$

Using (5.14) and (5.15) to predict the current's spectrum, and in some cases separately as (5.16) and (5.17), the second spectrum magnitude will not match the same prediction as the first condition due to the unaligned phase in the noise sources. In conclusion, in the choke case, all measured spectrums should have aligned phases or be measured simultaneously. As stated, the phase information cannot be ignored here. The filter method used to overcome the noise floor in the choke case is not available.

$$\begin{bmatrix} i_{CMi} \\ i_{CMo} \end{bmatrix} = -\frac{\begin{bmatrix} (Z_{11}+Z_{SHi})V_{N1} - Z_{12}V_{N2} \\ (Z_{22}+Z_{SHo})V_{N2} - Z_{21}V_{N1} \end{bmatrix}}{\left((Z_{11}+Z_{SHi})(Z_{22}+Z_{SHo}) - Z_{12}Z_{21}\right)} \tag{3.15}$$

$$\begin{bmatrix} \tilde{i}_{CMi} \\ \tilde{i}_{CMo} \end{bmatrix} = -\frac{\begin{bmatrix} (Z_{11}+Z_{SHi})V_{N1} - Z_{12}V_{N2}\cdot 1\angle\theta \\ (Z_{22}+Z_{SHo})V_{N2}\cdot 1\angle\theta - Z_{21}V_{N1} \end{bmatrix}}{\left((Z_{11}+Z_{SHi})(Z_{22}+Z_{SHo}) - Z_{12}Z_{21}\right)} \tag{3.16}$$

In the second experiment in UBM, the shunt cases with larger CM noise are chosen, and the noise floor issue is most serious in the shunt case, owing to fact that it has the largest noises. In the UBM extraction procedures, the shunt case spectrums are used to perform optimization where the aim is minimizing the error between the spectrum magnitude square in measurements and predictions as (5.11). The effective information from the experiment to the model is the current spectrum magnitude. No phase information is relevant here. If the input and output current are not measured at the same time, there may be some unpredictable phase delay between them. However, this does affect the model and the optimization process.

For the validation case, a comparison between the measurements and predictions is performed, where the topic is spectrum magnitude. The phase information remains insignificant. Consequently, the filter method can apply to the shunt and validation cases.

Figure 3-59 and Figure 3-60 exhibit the connected and assembled spectrum in the 20 kHz shunt and validation cases, which are adapted to the optimization process and validation comparison. The 20 kHz predictions for the shunt case (Figure 3-61) and the validation case (Figure 3-62) with new optimized inverter impedances match the measurement to almost 30 MHz. For the 70 kHz case, the connected spectrum in the shunts in Figure 3-63 is adapted into the optimization and its results for the shunt prediction in Figure 3-64 and for the validation case in Figure 3-65 implies that the UBM can also give good predictions over the whole EMI range. Focusing on the spectrum above 10 MHz in Figure 3-61 to Figure 3-65, there is still some mismatch. For example, in the shunt 70 kHz case, the measurement shows some peak between 20 MHz and 30 MHz, which the prediction cannot capture clearly. This illustrates an existing weakness in the UBM reliability prediction.

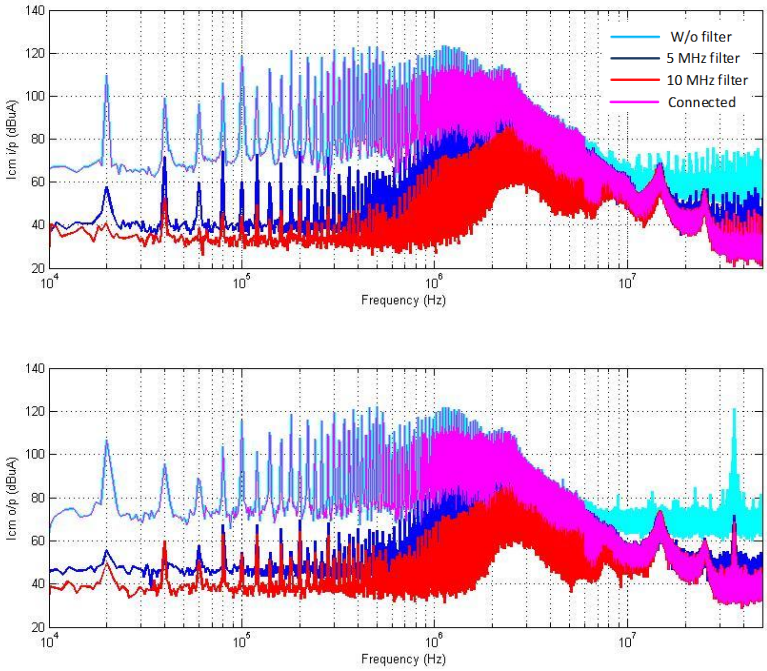

Figure 3-59 The connected spectrum based on the spectrum without filter, with 5 MHz and 10 MHz high-pass filter in the 20 kHz shunt case

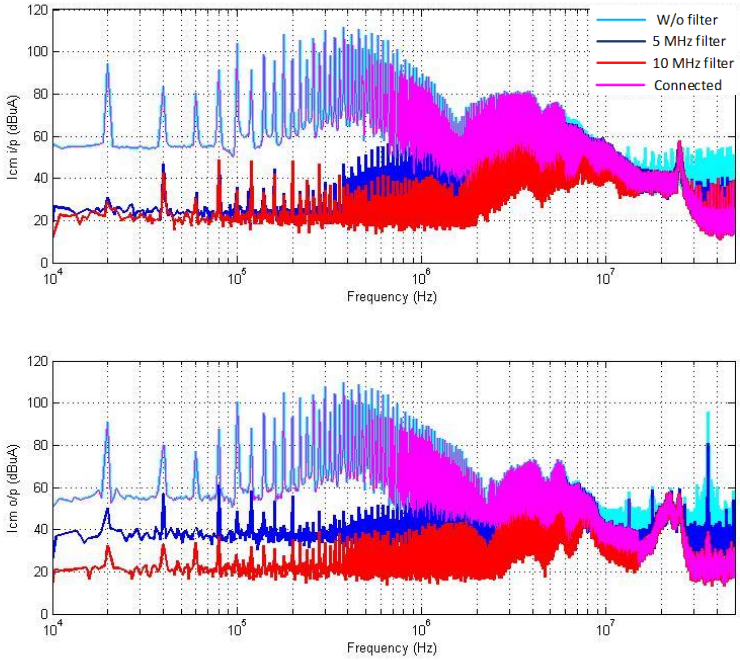

Figure 3-60 The connected spectrum based on the spectrum without filter, with 5 MHz and 10 MHz high-pass filter in the 20 kHz validation case

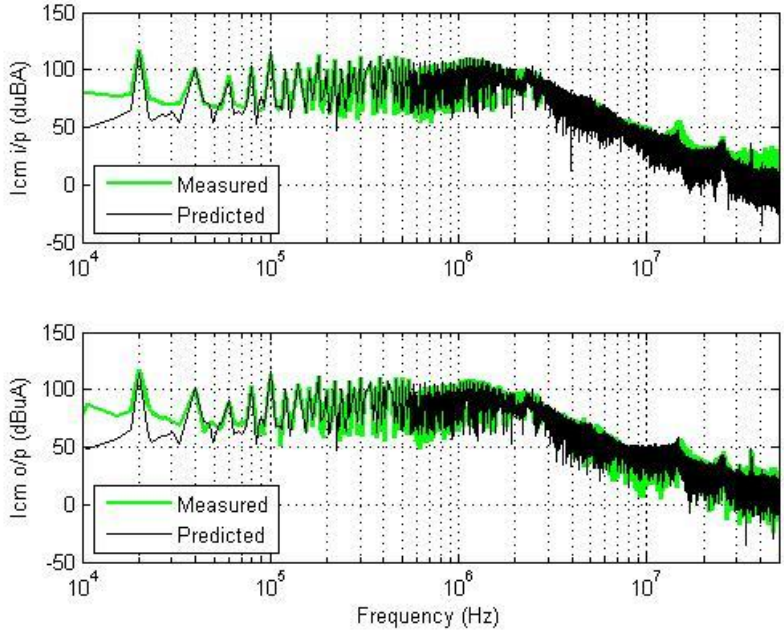

Figure 3-61 Comparison between the measurements and predictions for the 20 kHz optimized shunt case with the connected spectrum

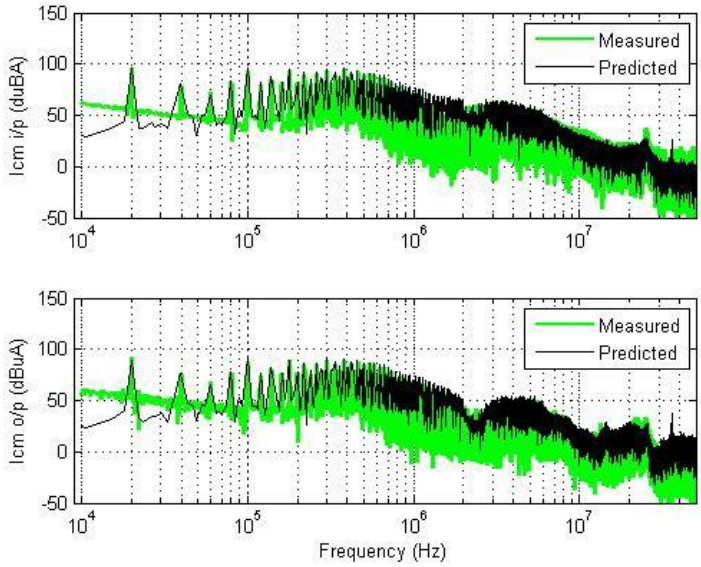

Figure 3-62 Comparison between the measurements and predictions for the 20 kHz validation case with the connected spectrum

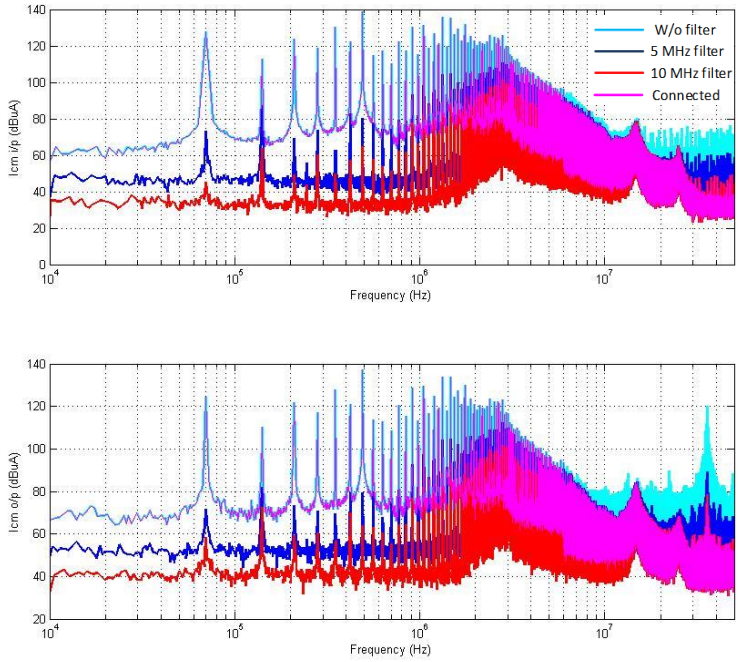

Figure 3-63 The connected spectrum based on the spectrum without filter, with 5 MHz and 10 MHz high-pass filter in the 70 kHz shunt case

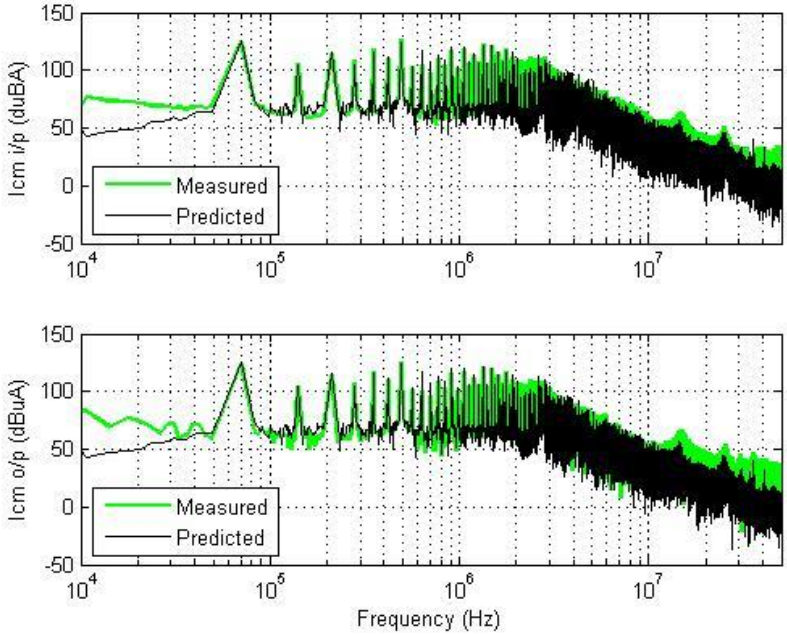

Figure 3-64 Comparison between the measurements and predictions for the 70 kHz optimized shunt case with the connected spectrum

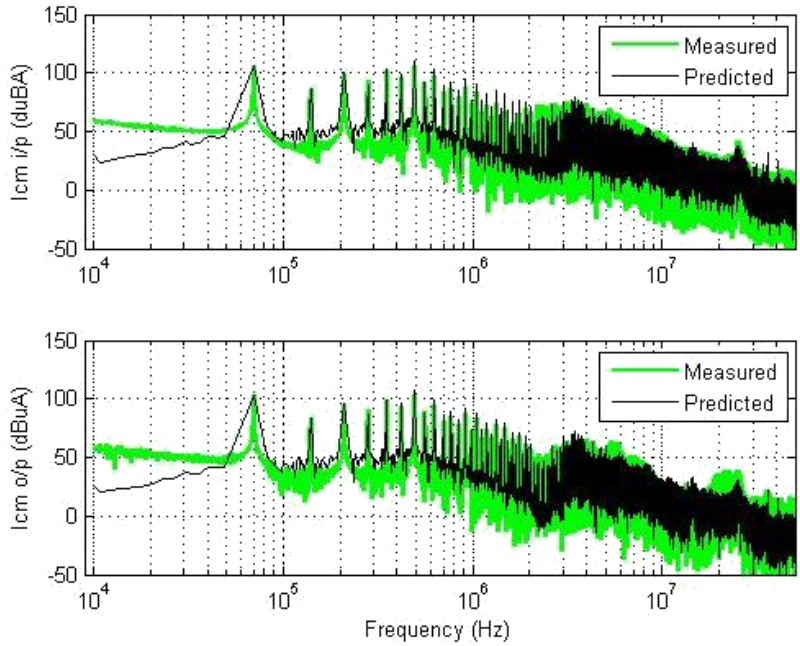

Figure 3-65 Comparison between the measurements and predictions for the 70 kHz validation case with the connected spectrum

3.7 Re-designed choke impedance in the high frequency

3.7.1 Choke design for higher impedance above 10 MHz

To improve the UBM prediction above 10 MHz, another impedance assumption in the model extraction — that the input and output impedances in the choke case should be much larger than the inverter impedances — is checked. However, the choke case curve in Figure 3-17 is 10 dB larger than the inverter impedance at 30 MHz. With this choke impedance, the noise sources are calculated in (5.4) and the inverter impedances are ignored, as they are comparable with the choke impedances. As a result, the noise sources lose accuracy above 1 MHz. Therefore, the chokes need higher impedances, and should be above 10 MHz as a whole.

In order to increase the choke impedances, a common method of increasing the inducatance by increasing the turn number is employed. However, with the turn intensive on the core, not only will the inductor core possibly be saturated, but the equivalent parallel capacitance (EPC) will also be more obvious and dominate the impedance at high frequency. As a result, the choke impedance at the lower frequency is higher, but is also lower at high frequency.

Another method to increase the inductor impedance is to put a small-value inductor in series, whose resonant frequency is located above 10 MHz and whose impedance is low at kHz but high in MHz. As a result, the total impedance of the two inductors in series will be higher above 10 MHz. Figure 3-66 lists some CM input chokes with their resonant frequency located at 800 kHz, 40 kHz, and 3 MHz, and their inductance as 15 mH, 40 mH, and 0.8 mH at 10 kHz separately.

Focusing on the impedance above 10 MHz, the third example with the smallest inductance and highest resonant frequency is the largest. The impedance above 10 MHz is mainly the EPC impedance, which is dependent on the turning intention. The more intensive the winding is, the larger the EPC and the smaller the impedance above 10 MHz.

In the choke experiments described above, the input choke is composed of Choke 1 and Choke 2. Therefore, in the input impedance curve (Figure 3-17 and Figure 3-67) in the choke case, there are two peaks rather than one. In order to increase the impedance above 10 MHz, a third choke is put in series, as shown in Figure 3-66, where the resonant frequency point is much larger than that of Choke 1 and 2. Thus, the total input impedance is increased above 10 MHz in the comparison between the old and new input choke designs (Figure 3-67).

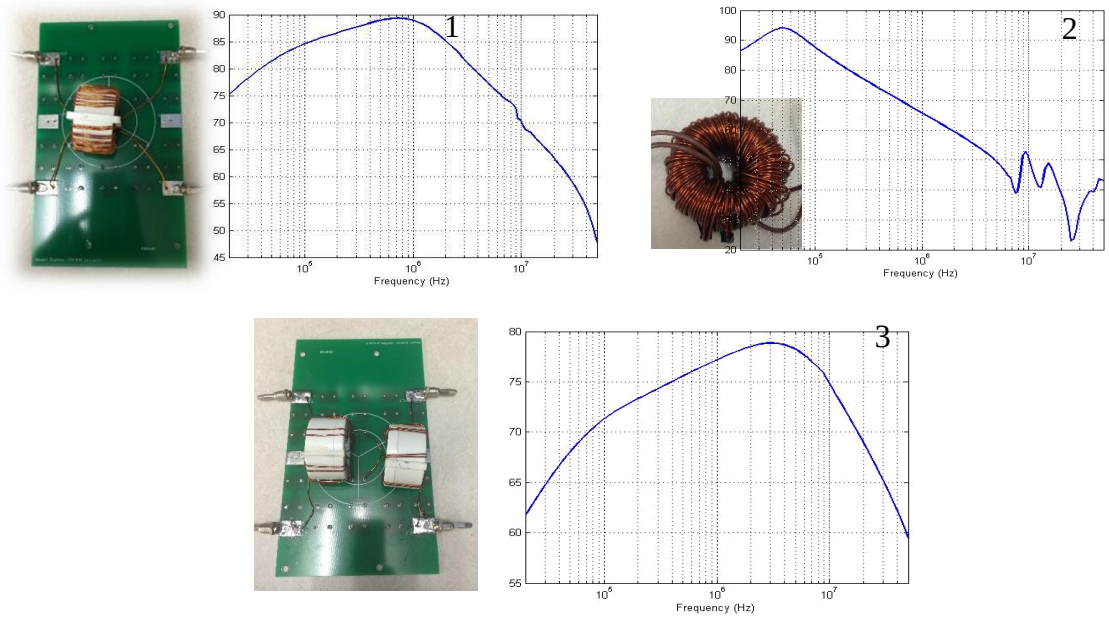

Figure 3-66 CM input chokes and their impedances-frequency curves

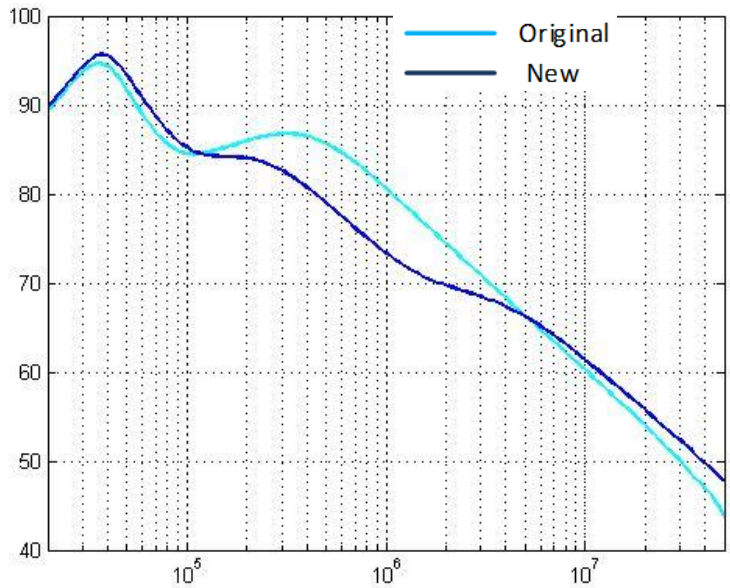

Figure 3-67 Comparison of the input impedance in the choke case between the original and new design

As for the output, a second choke (Figure 3-68 Choke 2) is put in series with the original output choke (Figure 3-68 Choke 1). Choke 2 has smaller inductance but smaller EPC as well. As a result, Choke 2 has high impedance above 10 MHz, 5 dB larger than that of Choke 1. With the second choke in series between the inverter and load, the output impedance in the choke is changed from the light blue curve in Figure 3-69 to the dark blue one.

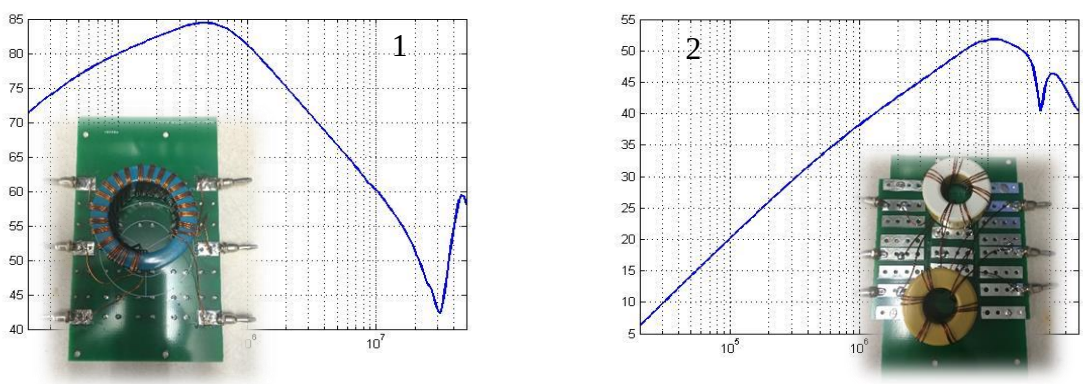

Figure 3-68 CM output chokes and their impedances-frequency curves

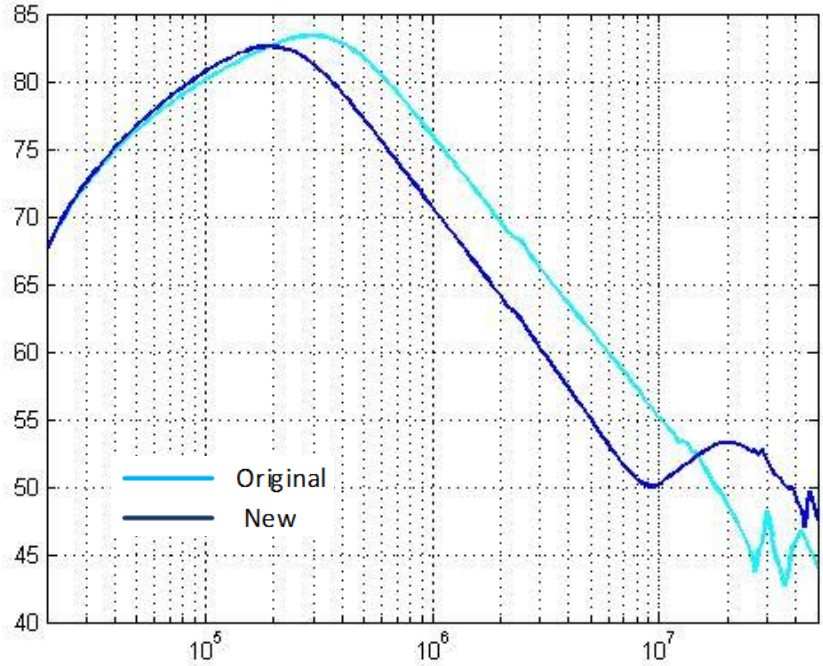

Figure 3-69 Comparison of the output impedance in the choke case between the original and new design

3.7.2 UBM re-extraction with the new choke impedances

With the new choke added, the input and output impedances of the choke case increases to 5 dB at 30 MHz compared with the original impedances in Figure 3-70.

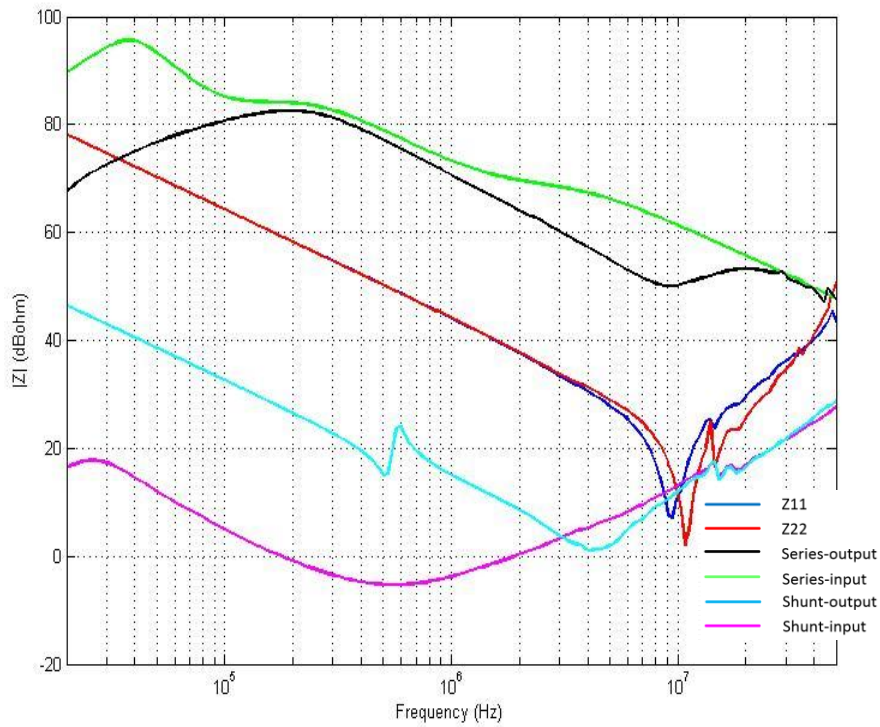

Figure 3-70 Choke case input and output impedances compared with the inverter impedances and the shunt case impedances after all improvements

With the all the impedance improvement, measurements for which are shown in Figure 3-70, the UBM extraction in the 20 kHz and 70 kHz switching frequency cases are repeated using the procedures with high-pass filters applied in Section 3.6.2. The spectrums in the shunt cases and the validation cases are connected by the segmented-frequency measurements. As a result of all improvements, the comparison between the measurement and prediction in the 20 kHz and 70 kHz switching frequency cases are exhibited in Figure 3-71 and Figure 3-72, implying the full range match. Therefore, the UBM prediction capacity can be extended to 30 MHz with almost complete matching between the measurement and UBM prediction.

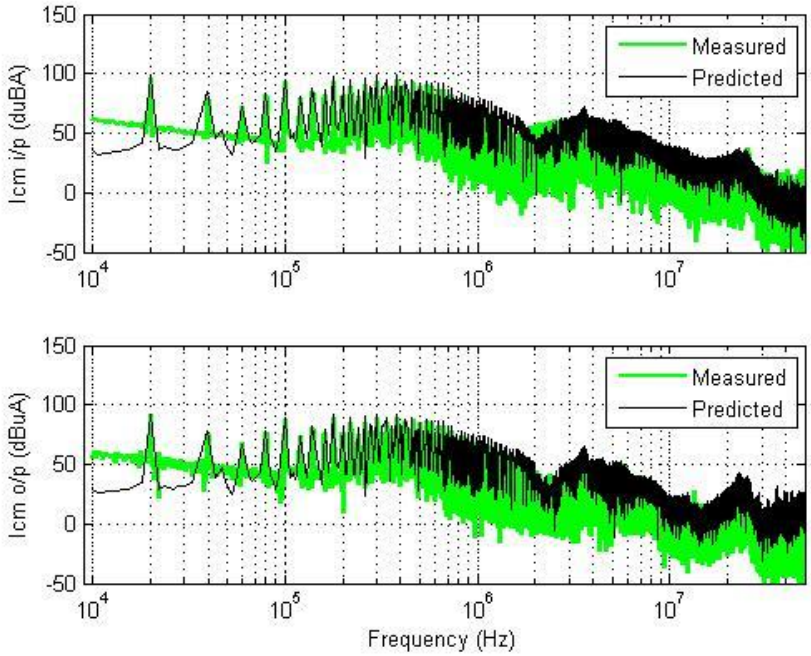

Figure 3-71 Comparison between the measurements and predictions for the 20 kHz validation case with improved choke and shunt case impedances and segmented-frequency spectrums

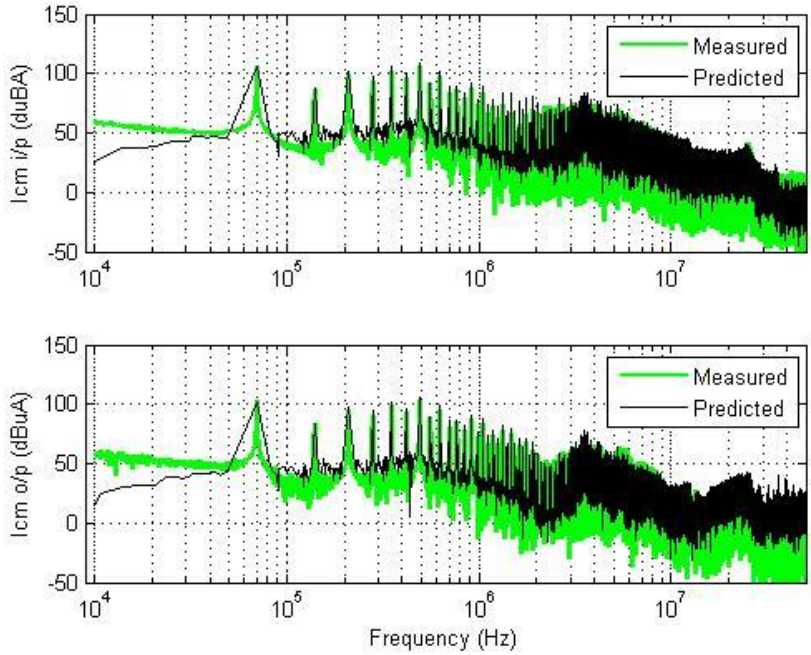

Figure 3-72 Comparison between the measurements and predictions for the 70 kHz validation case with improved choke and shunt case impedances and segmented-frequency spectrums

3.8 Improved high frequency UBM

Overall, the UBM prediction capacity is extended to the full EMI range by overcoming the noise floor issue and with better impedances design. The extraction procedures of the improved UBM for high frequency are given below with notes:

1. Inverter impedance measurement:
   - Z_{11} and Z_{22} can be measured with an impedance analyzer. Z12 can be measured with a network analyzer. Without a network analyzer, Z12 can be equal to Z11 (or Z22).
2. Choke case experiment:
   - Keep the assumption that input and output impedances should be much larger than the inverter impedance in the full EMI frequency range. A second choke with a smaller inductance can be added to push the input or output impedance larger in high frequency.
3. Shunt case experiment:
   - Keep the assumption that input and output impedances should be much smaller than the inverter impedance in the full EMI range. The better connection design in the shunt fixture with smaller ESL will help decrease the input/output impedances in the shunt case.
   - Take the shunt spectrums as the segmented-frequency connected ones with high-pass filters inserted between the currents' probes and the oscilloscope.
4. Optimization:
   - Two RCL branches in parallel as the inverter impedances will help provide a better match.
5. Validation:
   - Take the validation spectrums as the segmented-frequency connected ones with high-pass filters inserted between the currents' probes and the oscilloscope.

Chapter 4 . DM Terminated Behavioral Model of SiC Power Converter

4.1 Introduction

There are several references focusing on the terminated behavioral model for DM noise prediction. Several topologies are validated with the terminated model at the input sides, including asymmetric ones like buck converters, and symmetric ones such as three-phase inverters. Generally, the effective range — where the predictions by terminated behavioral models match the measurements — can be up to 20 MHz. In this chapter, the DM terminated behavioral model is explained in detail, and is based on the fact that the DM noise is decoupled from the CM noise. This assumption will then be checked, in detail, in the three-phase SiC MOSFET inverter. The output DM terminated model is extracted in the two switching frequency cases in order to verify the prediction capacity of the model.

4.2 DM terminated behavioral modeling

First, assume that the input side DM noise in a motor-drive system is effectively decoupled from the output side noise, provided that the dc-link capacitor keeps the ac impedance between the dc rails low enough. Then let's also assume that, due to the symmetry of the drive, there is no significant mixed-mode noise [49, 50] present. Under these assumptions, unlike the CM model discussed above, there is no need for an unterminated DM model for the motor-drive. Instead, terminated EMI models can be extracted separately for modeling the input (dc) and output (ac) side DM noise. This idea is shown in Figure 4-1. The input side model for the three-phase inverter in consideration here has positive and negative as its terminals and, owing to the symmetry, the output side model can be approximated between any two phases.

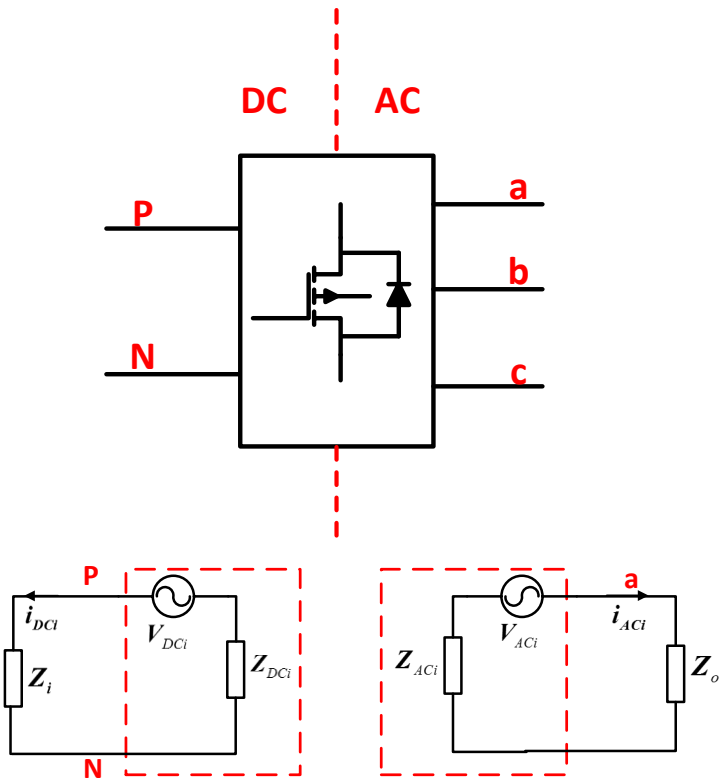

Figure 4-1 DM noise models for a three-phase inverter

The modeling procedure is similar for both input and output sides, so let's consider the input side to understand the model identification process. First, a near open-circuit condition at the terminals is created by using a large inductive filter. Fig 4.47 shows this configuration. This condition is referred to as the "choke-condition". The DM noise current i_{DCi} is then measured in time domain with a current probe and a sampling oscilloscope. The converter's input impedance Z_{DCi} and the network impedance Z_i are measured directly using an impedance analyzer. It should be noted that the probe of the impedance analyzer is often grounded and hence measuring DM impedance is difficult. Errors in the measured impedance can be minimized by either isolating the measured system from the ground or by using an RF balun (unbalanced-to-balanced).

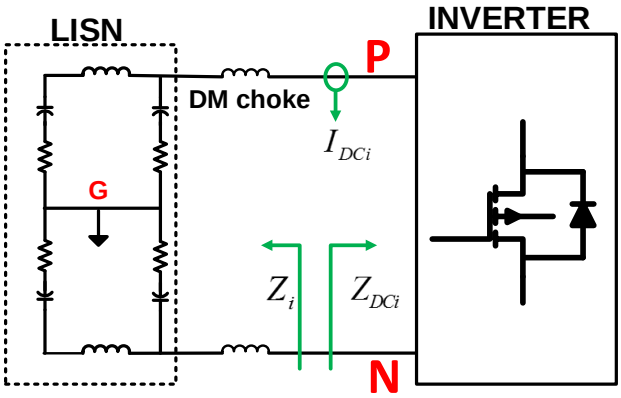

Figure 4-2 Choke-condition for input side DM model extraction

The noise source can be now extracted from the "choke-condition" as:

$$V_{DCi} = i_{DCi}(Z_{DCi} + Z_i) \tag{4.1}$$

This completes the model extraction process for the input side. Similarly, the output side model can also be extracted. The only difference is that we need a three phase DM filter comprised of high value inductors to create the series condition. The assumptions of no significant input-output side coupling and no significant mixed-mode noise must be verified experimentally before applying this procedure.

The DM current is measured as shown in Figure 4-3 where the DM current is defined as Equation (2.2).

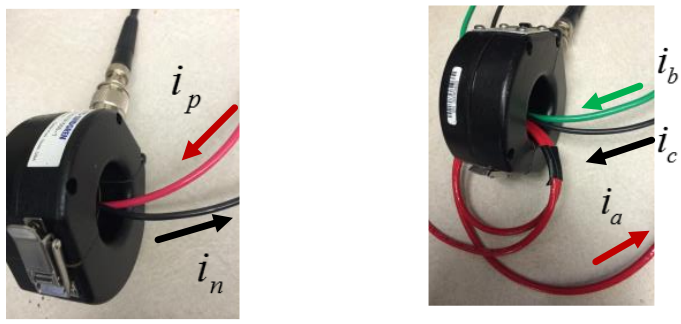

Figure 4-3 DM current measurement fixture

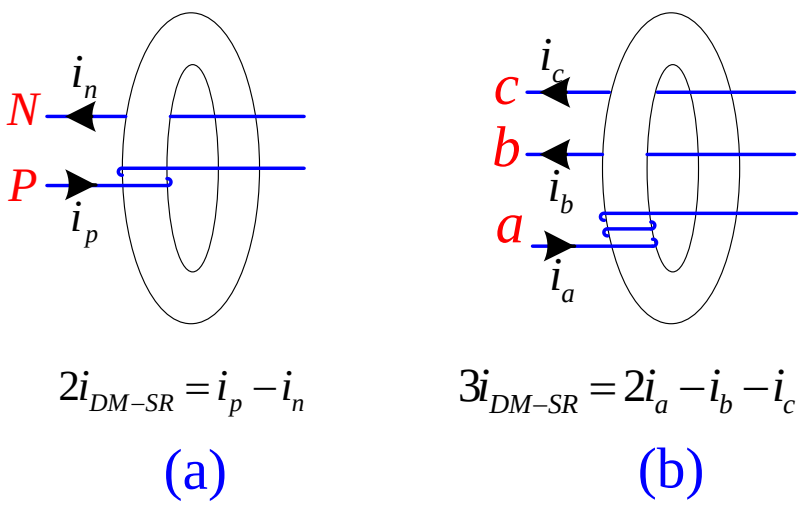

Figure 4-4 Measurement of DM currents (a) input side (b) output side

4.3 System analysis of the CM and DM emission at input and output sides

The aim of the EMI modeling is to predict the total noise on one cable and to help design a corresponding EMI filter to attenuate the total noise. In general, the noise can be separated into DM and CM, which requires separate DM and CM filters. As a result, the terminated model will be composed of CM and DM. In the DM model, only DM noise can be predicted and reduced

below the standard by DM filters. The same is true of the CM noise. The total noise is the sum of the DM and CM noise. When the DM and CM noise are reduced below the standard with some margins, the total noise will satisfy the standard, which is used by both the DM and CM noise.

The traditional method described above is available based on the assumption that the DM and CM models are both working at the same time. The DM and CM models can be separated based on the assumption that the DM and CM noise are decoupled. In theory, if the system is perfectly symmetric, including all the parasitic parameters, the DM and CM noise will be decoupled.

Then the DM models can be separated into the input and output terminated models when the DM output noise is decoupled from the DM input noise. In theory, if the DC bus capacitance is large enough, the DM input noise is independent of the DM output noise.

Here, before applying the DM input/output terminated behavioral model, it is necessary to check the relationship of the CM and DM noise at the input and output sides experimentally. The whole system can be separated into four sub-systems as Figure 4-5 illustrates. It has been verified in Chapter 3 that the input and output CM noise are coupled together. With CM chokes inserted at the output, the input CM noise will change accordingly. In this section, the other three relationships among the four sub-systems will be explored.

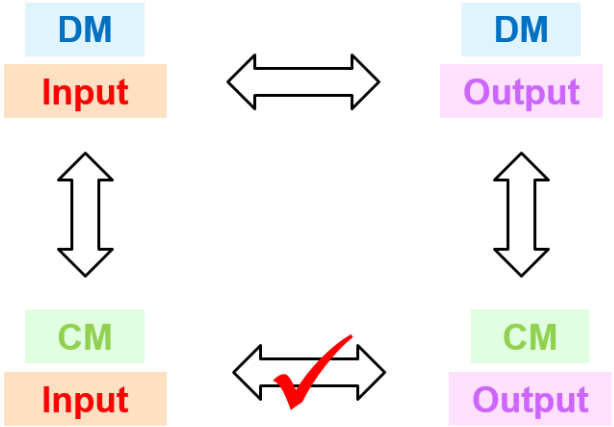

Figure 4-5 Relationship among the four sub-systems where CM input and output are coupled

As this section focuses on the exploration of the relationship among the sub-systems, there is no need to find the effects from the higher switching frequency. So in this section, all the experiments are carried out on the three-phase SiC MOSFET inverter with 20 kHz switching frequency.

4.3.1 Relationship between input and output noise in DM

With the DC bus capacitor, the input and output DM noise should, in theory, be decoupled because the larger capacitor can absorb and balance the DM noise from the input to the output side (or the output to the input side). In order to verify this in an experiment, three cases with different DM loads and the input filters are performed, as explained in Table 4-1. In Table 4-1, ‘sr’ means a DM choke inserted between the inverter and LISN at the input side, or between the inverter and the RL load; ‘nm’ refers to the direct connection from the inverter to LISN or the RL load.

Compared with the fixture setting in Case 1 and Case 2, they have the same DM input impedance, but different DM output impedance. As for Case 2 and 3, they differ in the DM input impedance but share the same DM output impedance. If the DM input and output are decoupled, then the DM input noises in Case 1 and 2 should be the same; the DM output noises in Case 2 and 3 should be the same. Accordingly, if the DM input noises in Case 1 and 2 are different, or the DM output noises in Case 2 and 3 are different, the DM input and output are coupled.

Table 4-1 Sub-system setting to find the relationship between input and output noise in DM

No.	Ip (DC)	Op (AC)
1	series	normal
2	series	series
3	normal	series

In Figure 4-6, the DM noises in Case 1 and 2 are compared. In the upper figure, the DM input noises are the same. The lower figure in Figure 4-7 illustrates that the DM output noise in Case 2 and 3 are the same. As a result of the two, it can be concluded that the DM input and output are decoupled. This relationship is added in Figure 4-8.

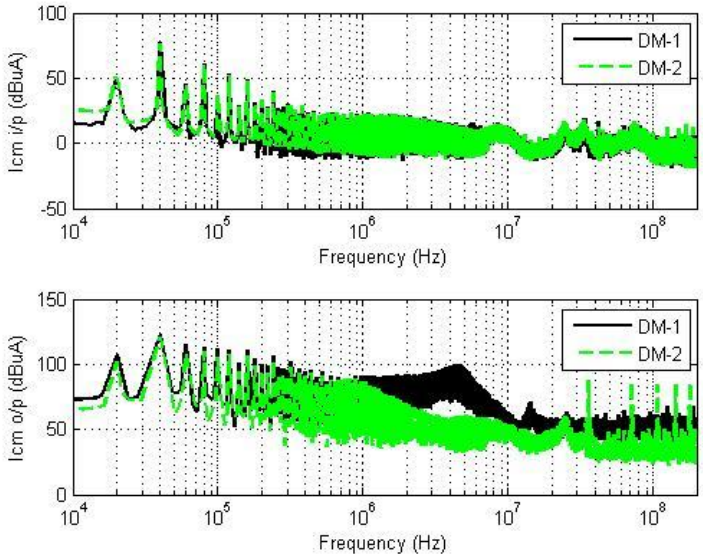

Figure 4-6 Comparison of the DM input (upper) and output (lower) noise spectrum between the Case 1 and Case 2 in Table 4-1

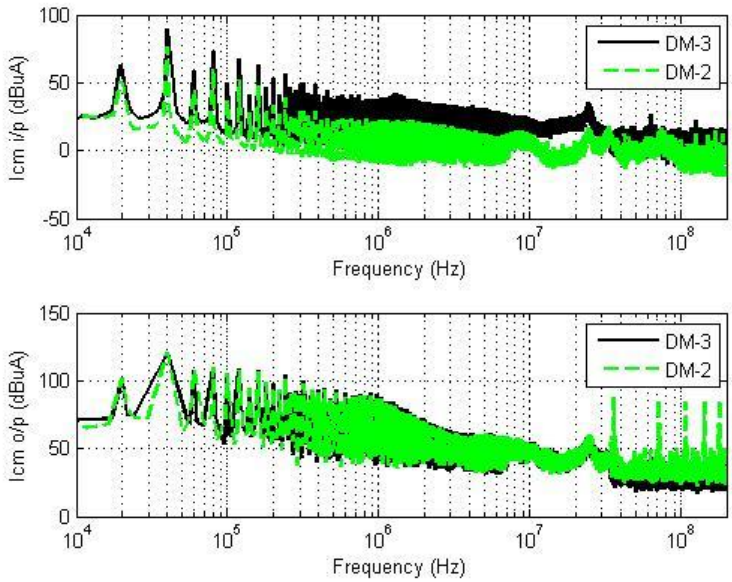

Figure 4-7 Comparison of the DM input (upper) and output (lower) noise spectrum between Case 2 and Case 3 in Table 4-1

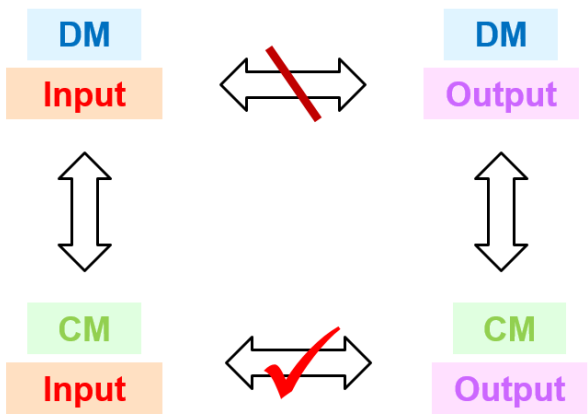

Figure 4-8 Relationship among the four sub-systems where CM input and output are coupled, DM input and output are decoupled

4.3.2 Relationship between DM and CM noise at the output side

From the reference related to the relationship between the DM and CM noise, there is no exact conclusion about the reason why CM and DM will be coupled. Generally, if the impedances in the system are symmetric from the three output terminals to the ground, there should be no coupled parts.

In order to verify this in experiment, three cases with different DM and CM filters are performed, explained in Table 4-2. In Table 4-2, 'sr' means a DM (or CM) choke inserted between the inverter and LISN at the input side, and between the inverter and the RL load; 'nm' refers to the direct connection from the inverter to LISN and the RL load.

Compared with the fixture setting in Case 1 and Case 2, they have the same DM output impedance, but different CM output impedance. As for Case 2 and 3, they differ in the DM output impedance but share the same CM output impedance. If the CM and DM output noises are decoupled, then the DM output noises in Case 1 and 2 should be the same; the CM output noises in Case 2 and 3 should be the same. As a corollary, if the DM output noises in Case 1 and 2 are different, or the CM output noises in Case 2 and 3 are different, the CM and DM output are coupled.

Table 4-2 Sub-system setting to find the relationship between DM and CM noise at the output side

No.	DM	CM
1	series	normal
2	series	series
3	normal	series

In Figure 4-9, the DM output noises in Case 1 and 2 are compared, which are almost the same in the EMI range. Figure 4-10 illustrates that the CM output noise in Case 2 and 3 are the same. As a result of the two, it can be concluded that the CM and DM noise at the output side are decoupled. This relationship is added in Figure 4-11.

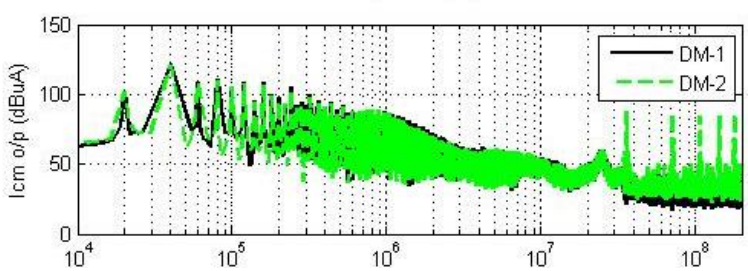

Figure 4-9 Comparison of the DM output noise spectrum between Case 1 and Case 2 in Table 4-2

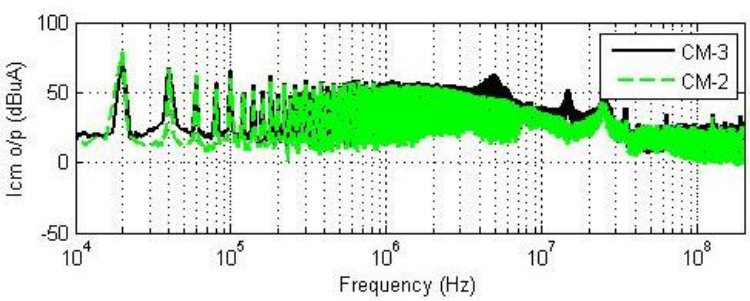

Figure 4-10 Comparison of the CM output noise spectrum between Case 2 and Case 3 in Table 4-2

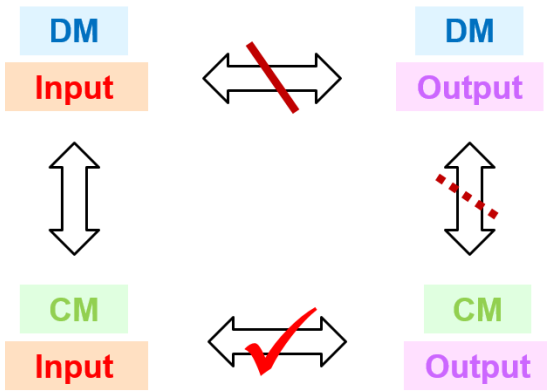

Figure 4-11 Relationship among the four sub-systems where output CM and DM are decoupled

4.3.3 Relationship between DM and CM noise at the input side

As for the relationship between the CM and DM noise at the input side, there is still no exact conclusion about the reason why CM and DM will be coupled. Generally, if the impedances in the system are symmetric from the positive and negative terminal to the ground, there should be no coupled parts.

In order to verify this in experiment, four cases with different DM and CM filters are performed, as explained in Table 4-3. In Table 4-3, 'sr' means a DM choke inserted between the inverter and LISN at the input side; 'sr1' and 'sr2' are two different CM chokes inserted between the inverter and LSN; 'nm' refers to the direct connection from the inverter to LISN. The detailed connection diagrams for these four cases are illustrated in Figure 4-12.

Compared with the fixture setting in the four cases in Table 4-3, they should have the same DM input impedance if the CM chokes do not have extra DM impedances. (However, in reality it is hard to fabricate CM chokes without any DM impedances.) Due to the different CM filters in the four cases, the CM noise will change. If the CM and DM input noises are decoupled, then the DM input noises in the four cases should be the same.

Table 4-3 Sub-system setting to find the relationship between DM and CM noise at the input side

No.	DM	CM
1	series	normal
2	series	series1
3	series	series 2
4	series	series 1+ series 2

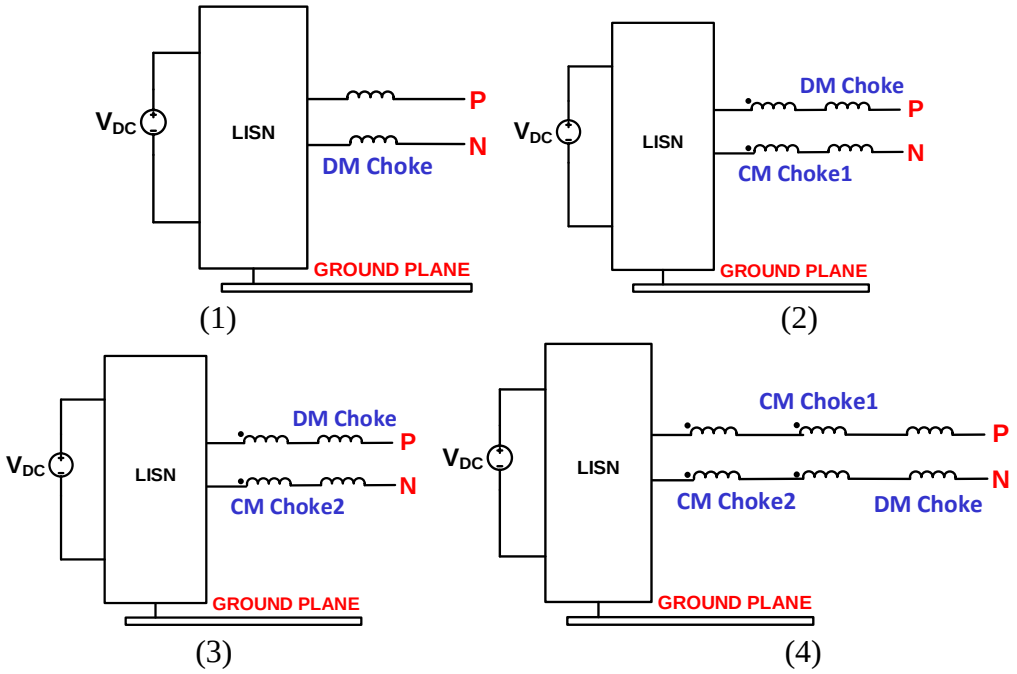

Figure 4-12 Sub-system setting to find the relationship between DM and CM noise at the input side corresponding to Table 4-3

As explained above, the CM spectrum in the experiment involving each of the four cases are different, as shown in Figure 4-13. Case 1 has the largest CM noise because there is no CM choke in this case. Then we need to see whether the DM noises are constant. First, Figure 4-14 shows the DM input impedances of the four cases. It is seen that the DM input impedance of Case 1 is 5 dB smaller than that of Case 2 and 4. This is because the CM choke 'sr1' and 'sr2' is not perfect with regard to extra DM impedance. The DM input impedances in Case 3 are almost the same as that of Case 2 (4) from 10 kHz to 1 MHz. Then the Case 3 impedance matches the impedance of Case 1 above 1.5 MHz. Therefore, if the DM and CM noises are decoupled, the DM noises will be the same when the DM impedances are the same no matter how CM noises change. As stated earlier, if the DM and CM noise are decoupled here, the Case 3 DM noise should be the same as that of Case 2 (or 4) from 10 kHz to 1 MHz, and the same as that of Case 1 above 1.5 MHz.

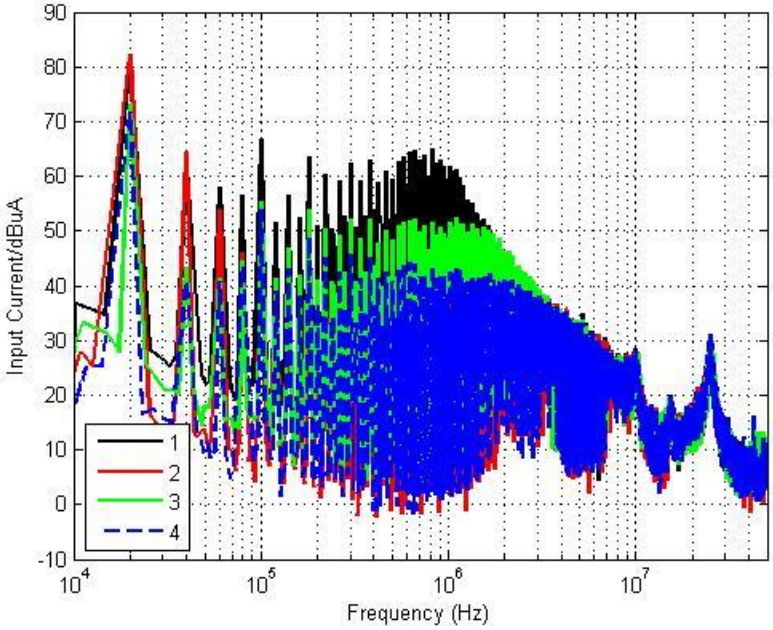

Figure 4-13 Comparison of the CM input noise spectrum among the four cases in Table 4-3

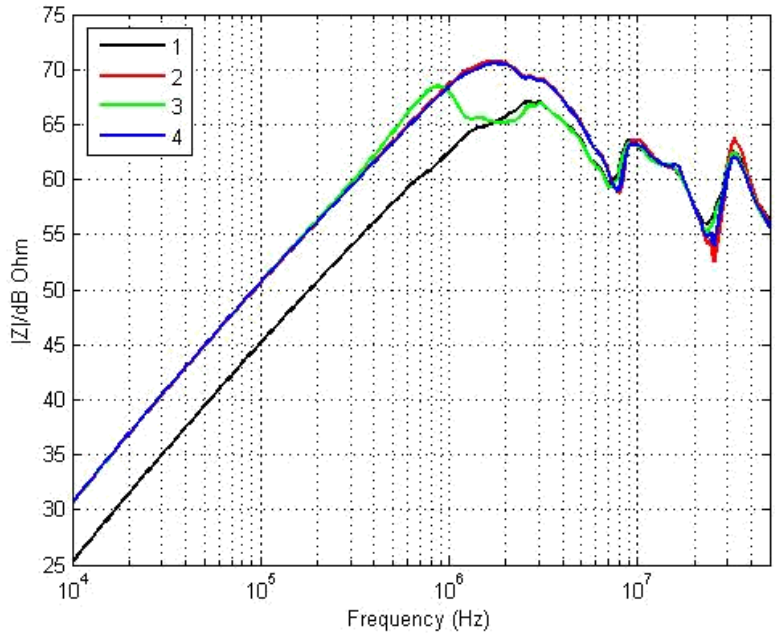

Figure 4-14 Comparison of the DM input impedances among the four cases in Table 4-3

Then, focus on Figure 4-15, which is the experimental result of the DM noise spectrum of the four cases in Table 4-3. The DM noise of Case 3 does not match with that of Case 2 from 200 kHz to 1 MHz. From 1.5 MHz to 2.5 MHz, the DM noise of Case 3 does not match that of the Case 1. As a conclusion based on the analysis, the DM noise is influenced by the changing CM noise.

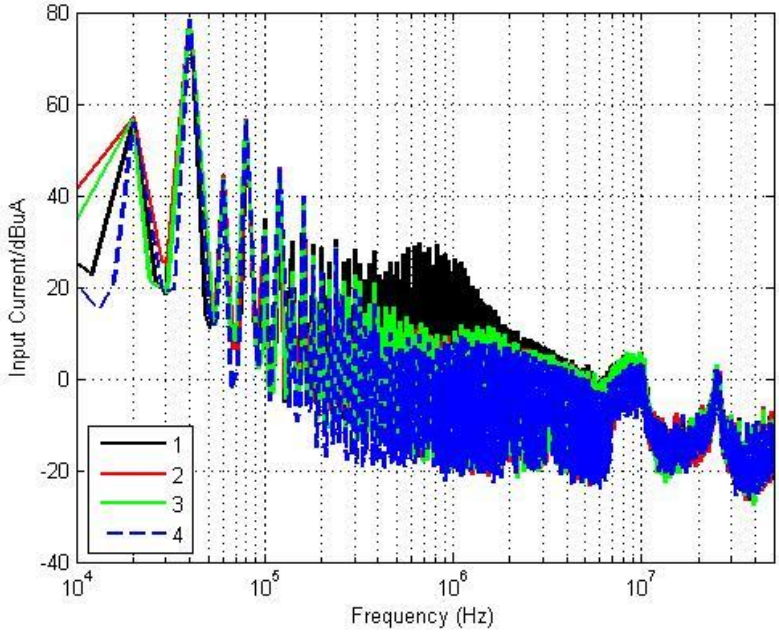

Figure 4-15 Comparison of the DM input noise spectrum among the four cases in Table 4-3

To another point, if the CM and DM are decoupled at the input side, the DM input noise will separate from the other three sub-systems and will be validated with the terminal behavioral model, which is mentioned in Section 4.2. According to the extraction procedures, the DM input noise sources can be calculated based on Equation (4.18) in the four cases. The equivalent DM input noise sources are drawn in Figure 4-16. They are quite different from each other, which means there are some extra CM effects on the model. Thus, the terminated behavioral model with the two impedances and one source is not suitable at the input side in the SiC MOSFET inverter setup.

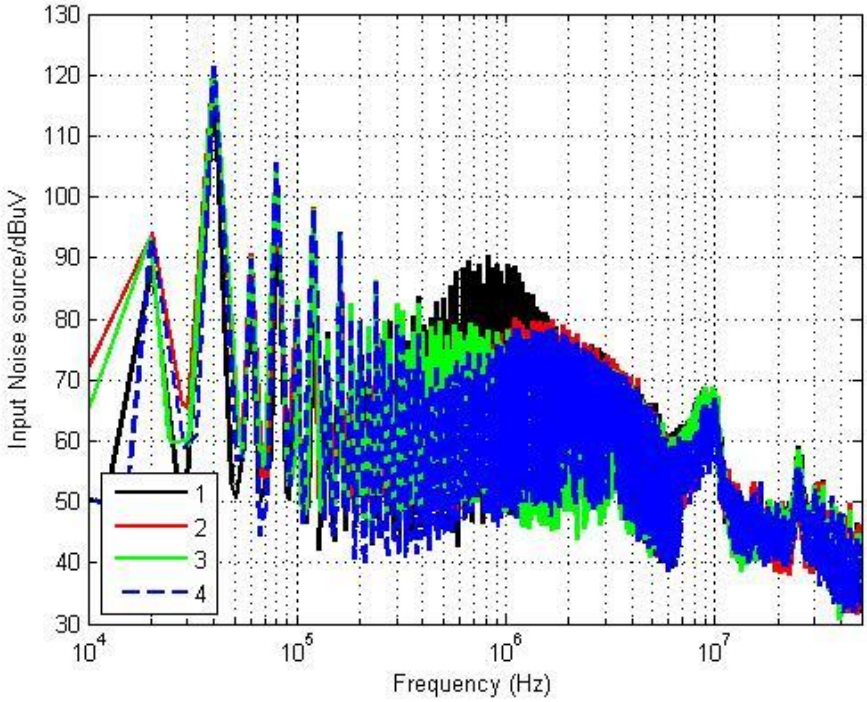

Figure 4-16 Comparison of the equivalent DM input noise sources among the four cases in Table 4-3

The analysis above focuses on constant DM noise with different CM noise. Then the influence from changing DM noise on the CM noise is assessed. Two cases with different DM and CM filters are performed, as explained in Table 4-4. The setting 'sr', 'sr1', 'sr2' and 'nm' here have the same meanings as those in Table 4-3. The detailed connection diagrams for these two cases are illustrated in Figure 4-18.

Compared with the fixture setting in the two cases in Table 4-4, they should have the same CM input impedance if the DM chokes do not have extra DM impedances, or if DM chokes inductances are much smaller than CM chokes inductances. Due to the different DM input impedance in the two cases, the DM noise will change. If the CM and DM input noises are decoupled, then the CM input noises in the four cases should be the same.

Table 4-4 Sub-system setting to find the relationship between DM and CM noise at the output side in second experiments

No.	DM	CM
1	Normal	series 1+ series 2
2	series	series 1+ series 2

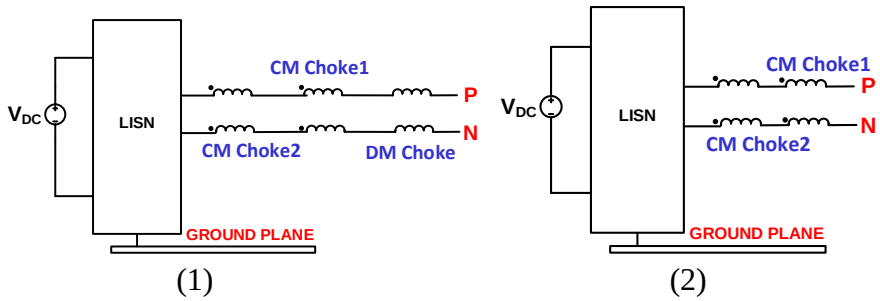

(1) (2)

Figure 4-17 Sub-system setting to find the relationship between DM and CM noise at the input side corresponding to Table 4-4

Figure 4-18 shows that the CM input noise in the two cases are almost the same, which is different from the previous analysis. We can conclude from this figure that the changing DM noises have almost no effect on the CM input noise. However, this does not conflict with the conclusion that the DM input noise is infulenced by the changing CM noise.

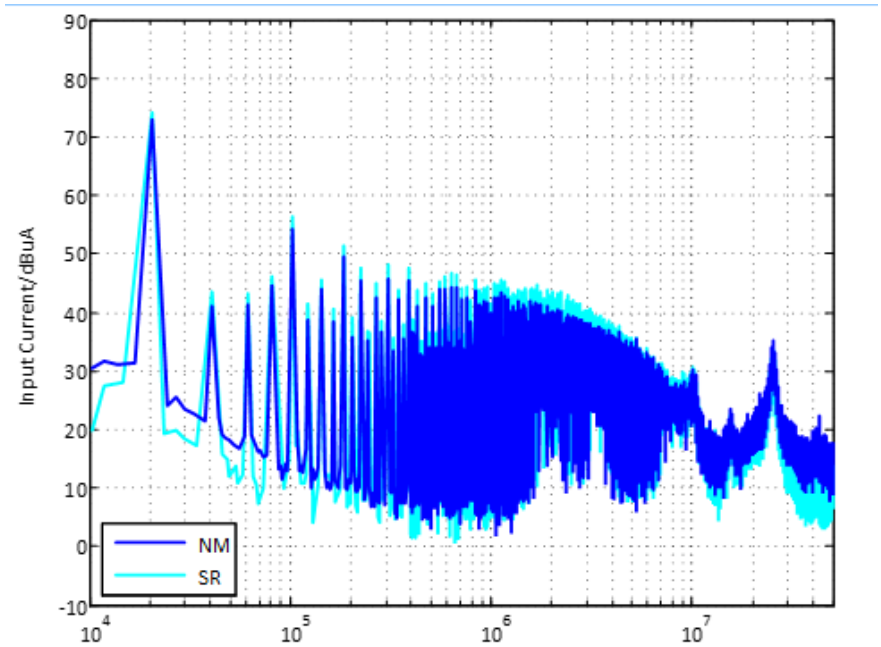

Figure 4-18 Comparison of the CM input noise spectrum among the four cases in Table 4-4

From another point of view, the equivalent DM noise can be calculated based on the terminated behavioral model with the DM spectrum (Figure 4-19) and the impedances. The noise sources are shown in Figure 4-20, where they are seen to be quite different from each other. As a result, the terminated model here does not accurately describe the DM input sub-system, which should consider the CM effects on the DM noise.

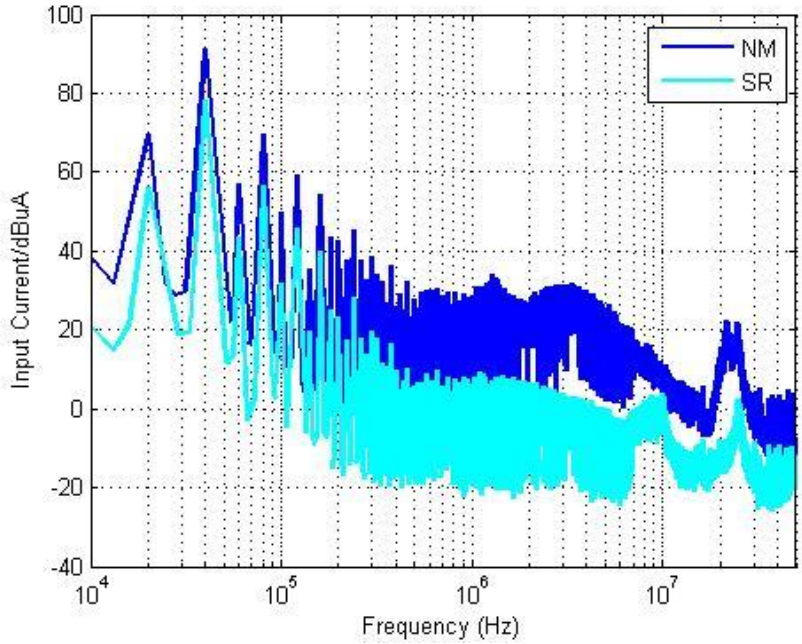

Figure 4-19 Comparison of the DM input noise spectrum among the four cases in Table 4-3

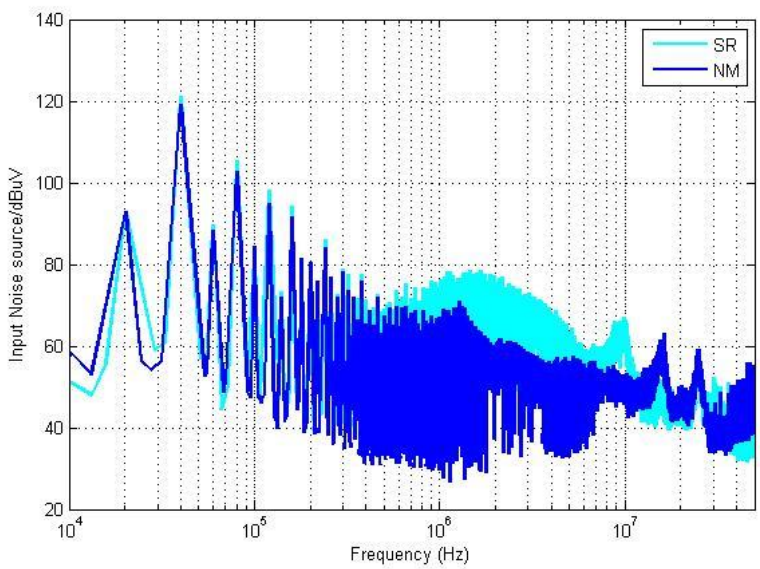

Figure 4-20 Comparison of the equivalent DM input noise sources among the four cases in Table 4-3

Overall, at the input sides, the DM and CM are coupled and the changing CM noise tends to have a larger effect on the DM noise. With this relationship in mind, Figure 4-21 includes all the relationships in the four sub-systems. The DM output is separated from the CM output and DM input. The DM input is coupled by the CM input, which requires better models than the DM terminated behavioral model.

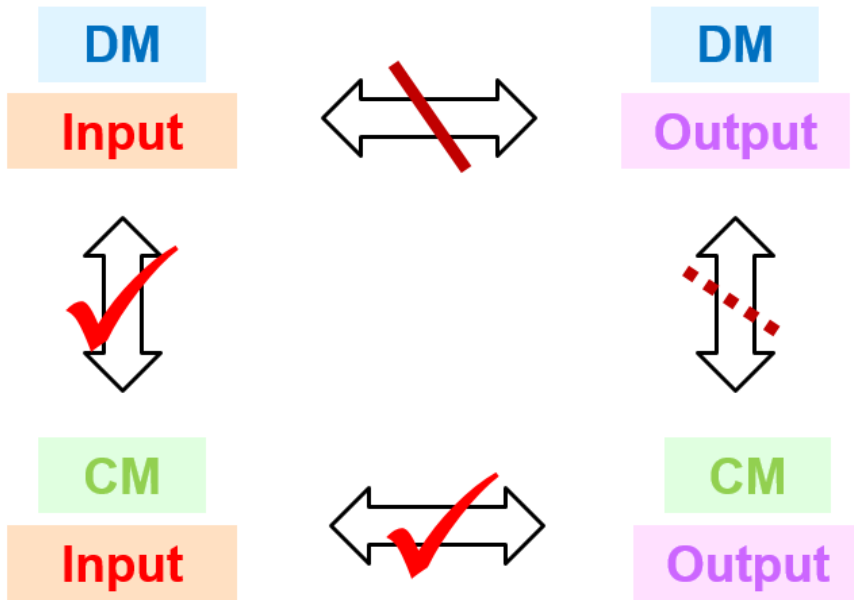

Figure 4-21 Final relationship among the four sub-systems

4.4 DM output terminated behavioral model based on SiC inverter

As the DM output is separated from the CM output and DM input, the DM output noise can be predicted with the DM terminated behavioral model. The model can also be extracted for the different switching frequencies.

4.4.1 DM output terminated behavioral model with 20 kHz switching frequency

In order to extract the model, a near 'open' condition is created with a DM choke inserted between the RL load and the inverter (Figure 4-22). Then measure Z_{ACi} , the impedance of the inverter from Terminal 'a' to 'b' in the 'power-off' condition, and Z_o , the impedance of the load part from 'a' to 'b'. The impedance measurements are shown in Figure 4-24. Then measure the DM output noise spectrum in the experiment as i_{DMo}. According to the DM output terminated behavioral model (Figure 4-23), the DM noise source can be calculated based on the equation below:

$$V_{ACi} = i_{DMo}(Z_{ACi} + Z_o) \tag{4.2}$$

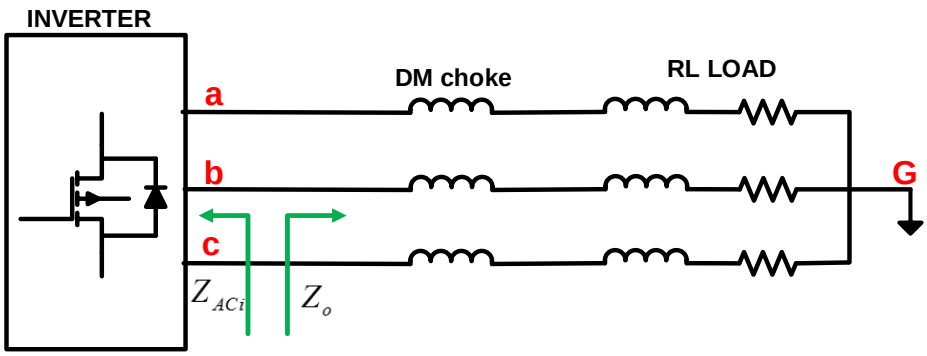

Figure 4-22 Inverter with DM chokes

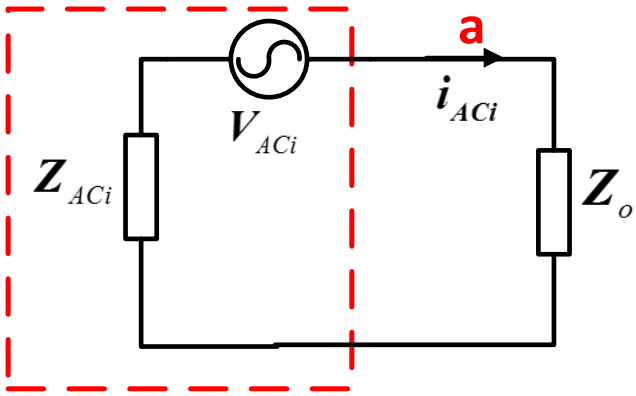

Figure 4-23 DM output terminated behavioral model

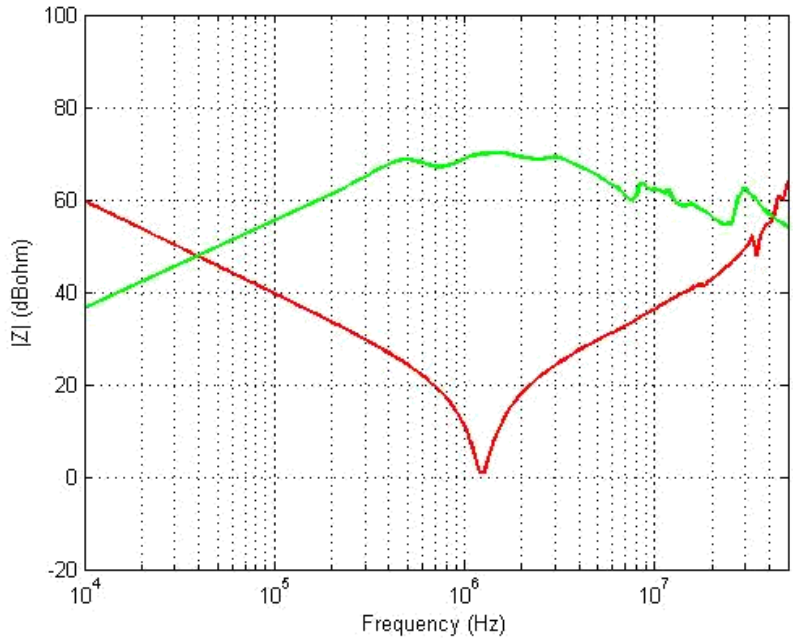

Figure 4-24 Comparison between the output impedance (green) and the output inverter impedance (red)

Then the standard working condition is chosen as a validation case to see whether the prediction from the model can match the experimental measurements. In this case, the DM noise

is quite large so that there will be a noise floor beginning at 20 MHz, which is shown as the blue line in Figure 4-25. In order to have full information in the whole EMI range, the filters, applied in the unterminated CM behavioral model, are placed between the current probes and the oscilloscope. The noise measurements with the two high-pass filters are shown in Figure 4-25. The red line, represented for the 10-MHz-pass filter measurement, has an effective range from 15 MHz to 30 MHz. So the segment-frequency spectrum is connected by the measurement without a filter in the range of 10k Hz to 15 MHz and the measurement with a 10-MHz-pass filter in the range of 15 MHz to 30 MHz. The pink line, represented as the segment-frequency spectrum, in Figure 4-26 explains this connection. We utilize this segmented-frequency spectrum to judge whether the prediction can match it up to 30 MHz. In Figure 4-27, it is seen that the prediction from the DM terminated model can match the experiment measurement in the whole EMI range. As a conclusion, the DM terminated behavioral model has full prediction capacity in the whole EMI range.

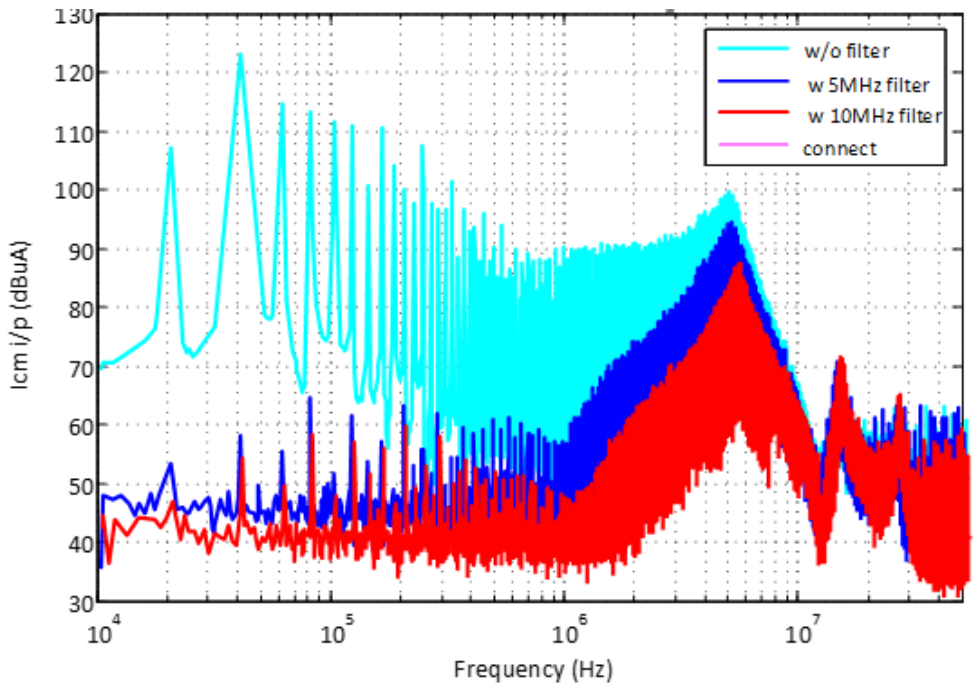

Figure 4-25 Comparison among the DM output noise spectrum without filter, with 5 MHz and 10 MHz high-pass filter in the 20 kHz validation case

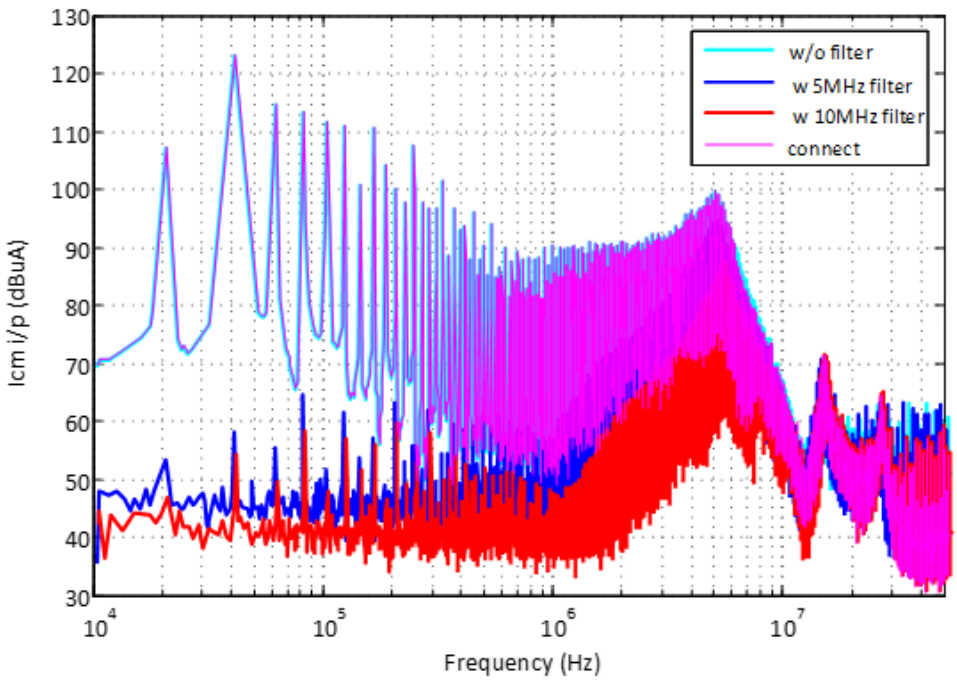

Figure 4-26 The connected segmented-frequency DM output spectrum based on the spectrum without filter, with 5 MHz and 10 MHz high-pass filter in the 20 kHz validation case

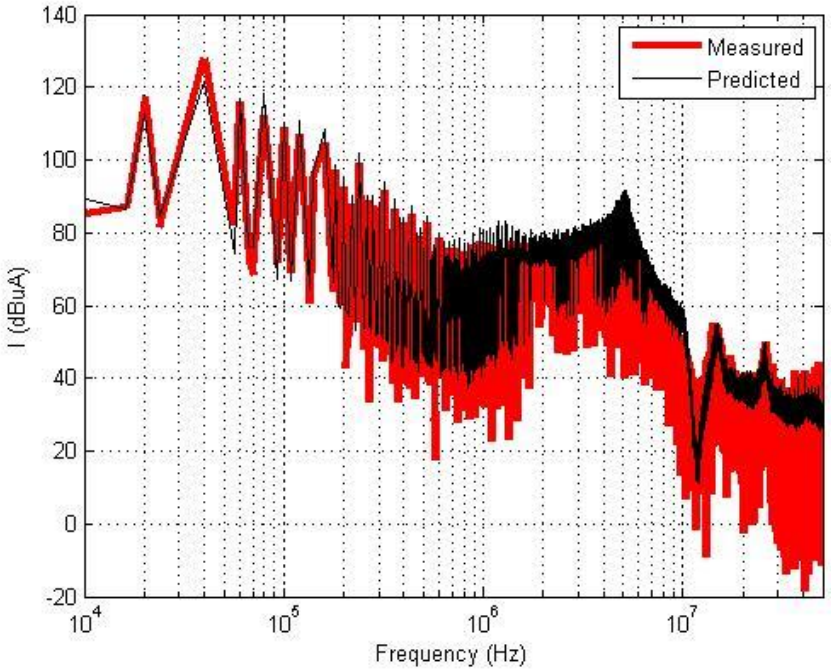

Figure 4-27 Comparison between the measurements and predictions for the 20 kHz validation case for DM output validation case

One note for the DM model extraction: care must be taken with the DM choke design. If the DM chokes inserted are saturated in the experiment, the DM noise will not reflect the DM

impedance measured. As a result, the prediction of the noise source will lose accuracy. The DM choke shown to the left of Figure 4-28 is saturated in the experiment, and accordingly, the model cannot predict the noise accurately below MHz (Figure 4-29).

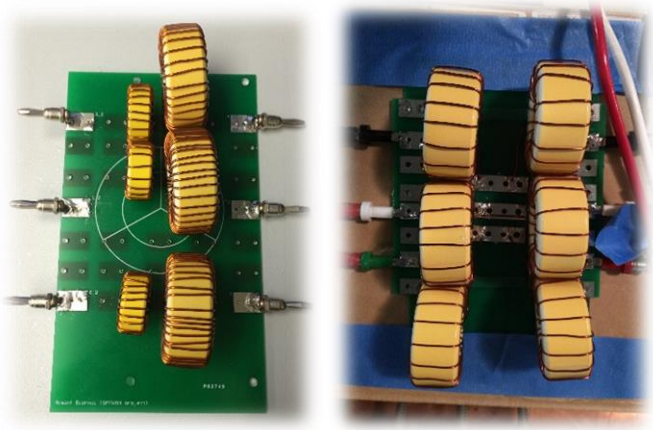

Figure 4-28 Saturated (left) and unsaturated (right) DM output chokes

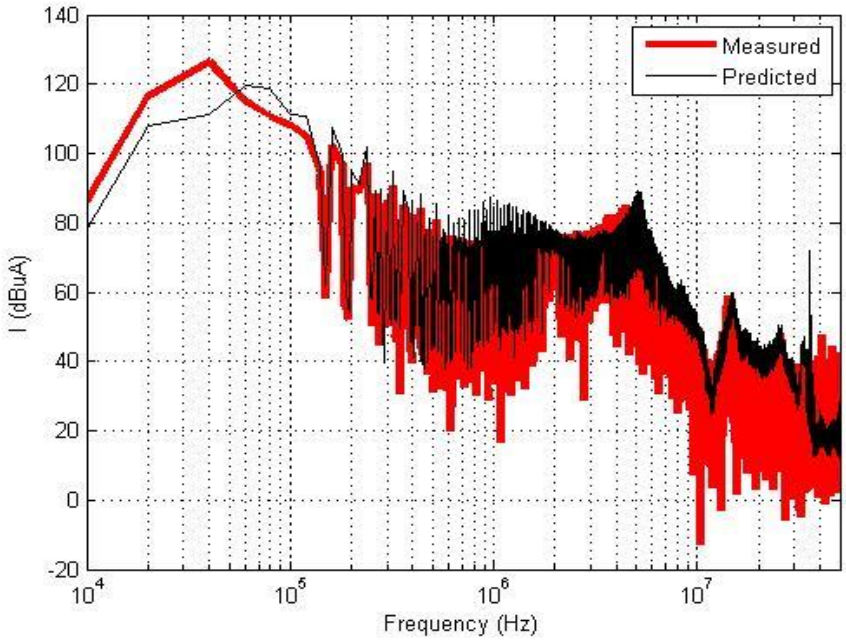

Figure 4-29 Comparison between the measurements and predictions for the 20 kHz validation case for DM output validation case when the DM chokes are saturated

4.4.2 DM output terminated behavioral model with 70 kHz switching frequency

In extraction of the DM terminated model in 70 kHz switching frequency, the difference from that of the 20 kHz case is the experiment noise. The impedance in the system does not require the second measurement because the impedances are independent of the switching behavior. Then the 'choke' case and the validation case are performed with 70 kHz switching frequency. Similar to the 20 kHz case, the validation case applies the segmented-frequency spectrum. In Figure 4-30,

the noise floor in the validation starts at 15 MHz and the 10-MHz-pass filter has an effective range from 10 MHz to 30 MHz. Then in Figure 4-31, the segmented-frequency spectrum is shown as the pink line. Then with the DM model, the prediction is compared with the measurement in the validation case in Figure 4-32. It can be concluded from Figure 4-32 that the model can still work with full prediction capacity when the switching frequency is pushed to 70 kHz.

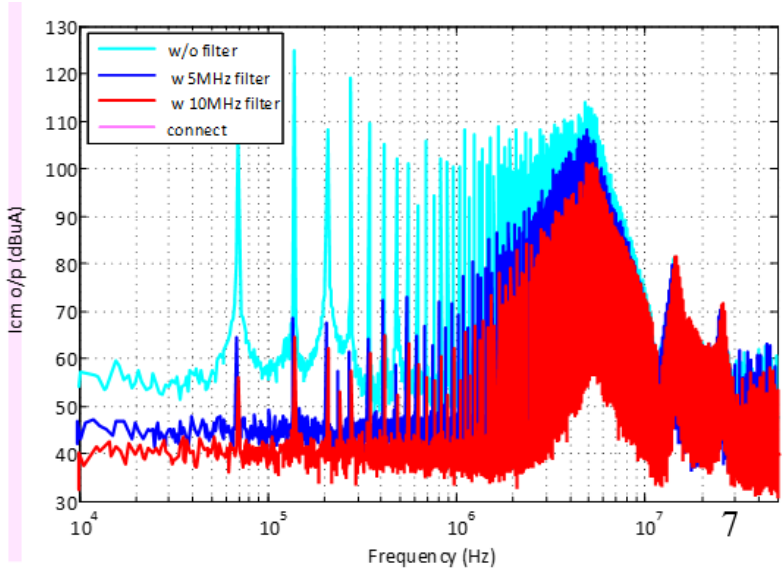

Figure 4-30 Comparison among the DM output noise spectrum without filter, with 5 MHz and 10 MHz high-pass filter in the 70 kHz validation case

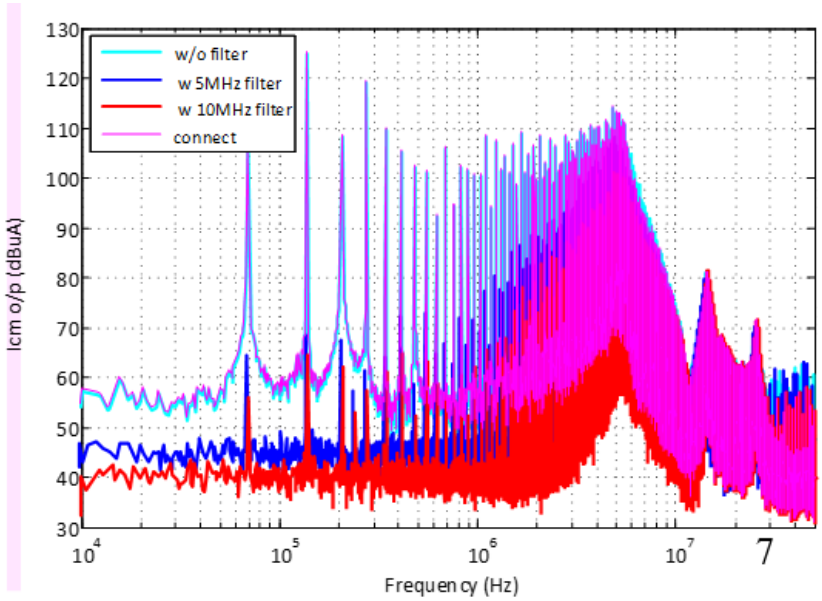

Figure 4-31 The connected segmented-frequency DM output spectrum based on the spectrum without filter, with 5 MHz and 10 MHz high-pass filter in the 70 kHz validation case

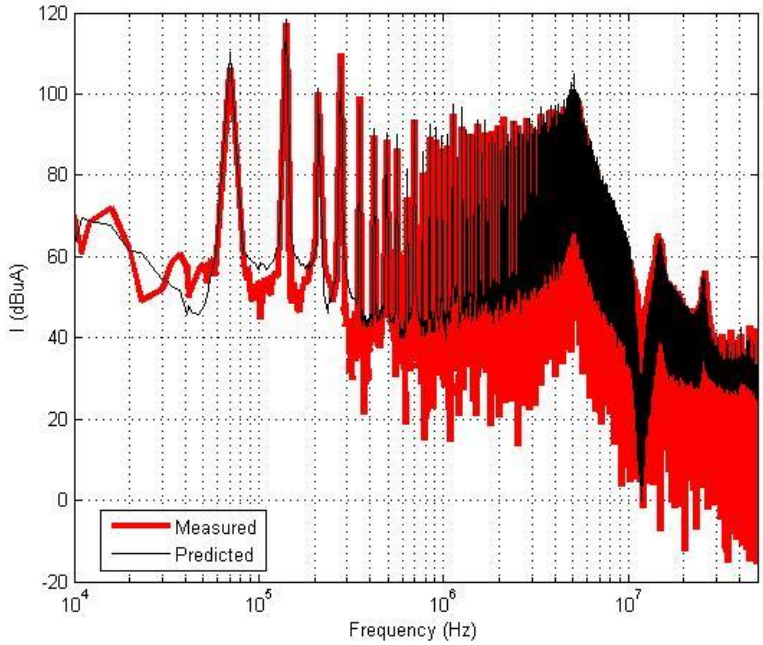

Figure 4-32 Comparison between the measurements and predictions for the 70 kHz validation case for DM output validation case

4.5 Analysis of disturbance from CM noise source on DM noise in Mix Mode Model at the inverter input side

4.5.1 Extended modular terminated behavioral model

In Section 4.3, it was found that the input CM and DM noise are coupled. As a result, the DM terminated behavior model cannot predict the DM noise precisely due to its ignorance of the CM impact. In this section, the proposed mixed mode model explains the reason of the coupling and is verified with experimental results. The newly proposed model is based on the modular-terminal-behavioral (MTB) model, which was put forward by Qian Liu in 2006. In the MTB model, two equivalent current noise sources are adopted to describe a switching module. Here we extend this theory to the three-phase inverter.

The extended MTB model, shown in Figure 4-33, characterizes the inverter input side, as shown in Figure 3-4. I_U and I_L are two equivalent current noise sources for the six switches. As in the inverter setup, shown in Figure 3-4, there exist three-phase inductors. Therefore, each switch can be seen as a current source, looking from the DC source to the switches. I_U represents the total noise sources of the three top switches, and the three bottom switch currents are included in I_L. I_U and I_L are not equal ($I_U = I_L$), or opposite ($I_U = -I_L$) to each other because the control signals of the top and bottom switches are reverse and there is some dead time duration between the two signals. In this model, the input CM and DM noise i_{CMi}, i_{CMo} are defined in (2.12) and (2.13). In Figure 4-33, Z_{IN} is the DC capacitor impedance and Z_{PG}, Z_{NG} are the impedance of C_{PG}, C_{NG} as shown in Figure 3-4. The CM impedance of LISN is defined from Terminal P to G, and N to G. Due to the symmetric structure of LISN, the impedance from P to G is equal to that from N to G, which is illustrated as Z_L in Figure 4-33.

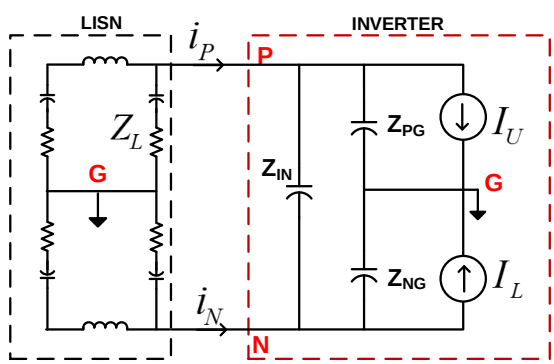

Figure 4-33 Extended modular terminated behavioral model for the inverter

With the extended MTB model, the input CM and DM noise can be predicted, which is only verified in a switch module in a two-pulse test. It is difficult to explore the relationship between the CM and DM noise, and, as a result, the mix mode (MM) terminated behavioral model is proposed in order to predict the noise in the inverter setup with high switching frequency.

4.5.2 Mix mode terminated behavioral model

Figure 4-34 illustrates the proposed mix mode terminated behavioral model. The difference between the new model and the MTB model is the noise source definition. I_{SCM} and I_{SDM} are equivalent CM and DM current noise sources. The relationship between I_{SCM}, I_{SDM} and I_U, I_L is described in (4.3). Due to the fact that I_U and I_L are not equal ($I_U = I_L$), or opposite ($I_U = -I_L$) to each other, I_{SCM} and I_{SDM} are not zero. The impedance Z_{PG}, Z_{NG} and Z_L are defined the same way as in the extended MTB model.

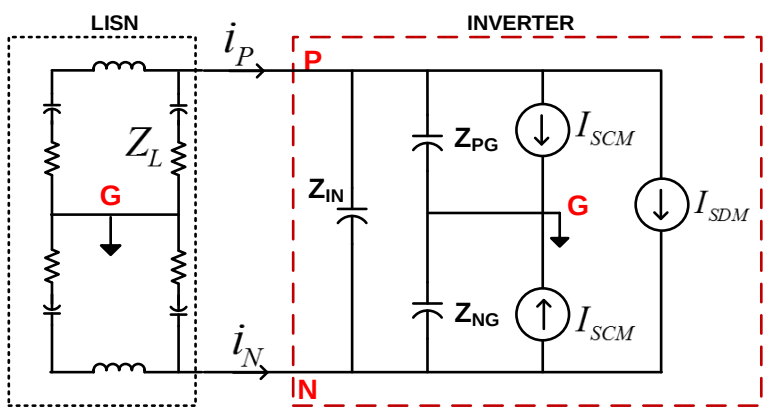

Figure 4-34 Mix-mode terminated behavioral model

$$\begin{aligned} I_{SCM} &= (I_U + I_L)/2 \\ I_{SDM} &= (I_U - I_L) \end{aligned} \tag{4.3}$$

In the MM model, the input CM and DM noise i_{CMi}, i_{CMo} can be calculated as (4.4) and (4.5). In (4.4), i_{CMi} has two parts, generated by I_{SCM} and I_{SDM} separately. i_{DMi} is also composed of the noise generated by I_{SCM} and I_{SDM} separately. Only if we have $Z_{PG} = Z_{NG}$, will i_{CMi} be generated by I_{SCM} and i_{DMi} will be generated by I_{SDM}. Once $Z_{PG} \neq Z_{NG}$, i_{CMi} will be influenced by I_{SDM} and i_{DMi} will be influenced by I_{SCM}, which means the CM and DM are coupled. As a conclusion, the necessary and sufficient condition of the decoupled CM and DM noise in the inverter setup is that Z_{PG} is equal to Z_{NG}, no matter the relationship between I_{SDM} and I_{SCM}. If the CM and DM are decoupled in the circuit, we call it a 'balanced circuit'.

$$\begin{aligned} 2i_{CM} &= i_P + i_N = \frac{Z_{IN}Z_L(Z_{NG}+Z_{PG}) + (2Z_{IN}+4Z_L)Z_{NG}Z_{PG}}{F} \cdot I_{SCM} + \frac{Z_{IN}Z_L(Z_{NG}-Z_{PG})}{F} \cdot I_{SDM}, \\ F &= Z_L Z_{IN}(Z_{PG}+Z_{NG}) + Z_L^2(Z_{IN}+Z_{PG}+Z_{NG}) + 2Z_L Z_{PG} Z_{PG} \end{aligned} \tag{4.4}$$

$$\begin{aligned} 2i_{DM} &= i_P - i_N = \frac{Z_{IN}Z_L(Z_{NG}-Z_{PG})}{F} \cdot I_{SCM} + \frac{Z_{IN}Z_L(Z_{NG}+Z_{PG}) + 2Z_{IN}Z_{NG}Z_{PG}}{F} \cdot I_{SDM}, \\ F &= Z_L Z_{IN}(Z_{PG}+Z_{NG}) + Z_L^2(Z_{IN}+Z_{PG}+Z_{NG}) + 2Z_L Z_{PG} Z_{PG} \end{aligned} \tag{4.5}$$

i_{CMi} , i_{CMo} can be further calculated when there is an EMI filter inserted between the inverter and LISN. For example, Figure 4-35 shows the diagram where the CM and DM chokes are added between the inverter and LISN. As a result, Z_L , which is the LISN impedance from Terminal P (N) to G is not the total input CM impedance, and $2Z_L$ is not the total input DM impedance. We need to figure out how to describe the input impedance in Figure 4-35. The models of CM and DM chokes are illustrated in Figure 4-36 and Figure 4-37.

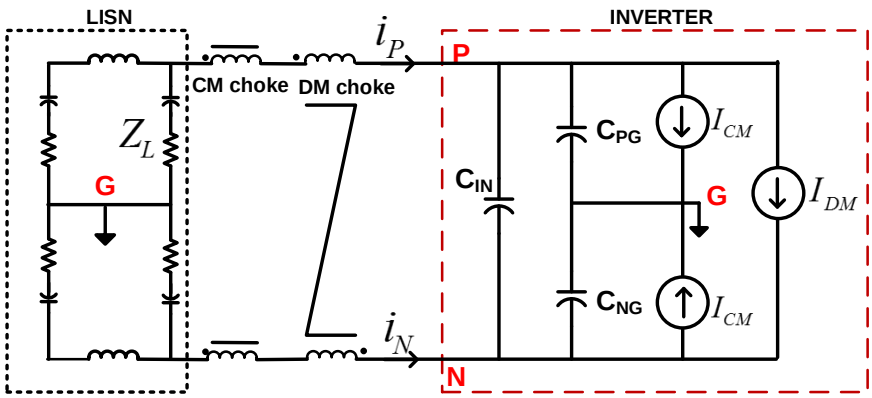

Figure 4-35 Mix-mode terminated behavioral model with CM and DM chokes

In Figure 4-36, Z_C is the CM impedance of the CM choke. The total CM voltage on the CM choke will be $Z_C(i_P + i_N)$, and each phase shares one half the total voltage. Therefore, according to the CM choke model, we can write the circuit equation in (4.6). In reality, we will connect Terminal P and N and measure the impedance from the short-circuited terminal to G when measuring the input CM impedance. So due to the short-circuited terminal and symmetric structure of the CM choke and LISN, we have $v_P = v_N, i_P = i_N$. Taken in conjunction with (4.6), we can find the input CM impedance expression in (4.7), which is the sum of the CM impedances of LISN and the CM choke.

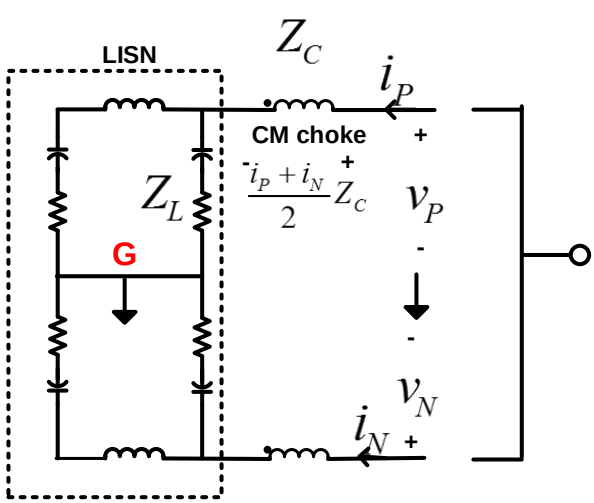

Figure 4-36 Input CM choke impedance model

$$v_P = i_P Z_L + \frac{i_P + i_N}{2} Z_C$$
$$v_N = i_N Z_L + \frac{i_P + i_N}{2} Z_C \tag{4.6}$$

$$\frac{v_P}{2i_P} = \frac{v_N}{2i_N} = Z_L + Z_C \tag{4.7}$$

As for the DM choke, it can be derived in the same way as the CM choke. In Figure 4-37, Z_D represents the DM choke impedance. The total differential voltage on the DM choke is $Z_D \frac{(i_P - i_N)}{2}$. So each branch will have $\frac{(i_P - i_N)}{2}\frac{Z_D}{2}$. The total DM impedance at the input side can be calculated to be the sum of the DM impedance of LISN and DM choke in (4.8).

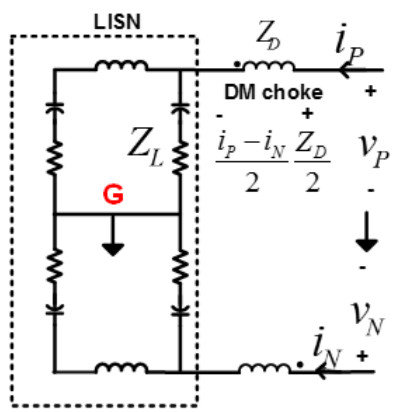

Figure 4-37 Input DM choke impedance model

$$\frac{v_P - v_N}{\frac{i_P - i_N}{2}} = 2Z_L + Z_D \tag{4.8}$$

Define Z_{LDM} and Z_{LCM} as (4.9) to help with the derivation.

$$Z_{LDM} = \frac{2Z_L + Z_D}{2}, Z_{LCM} = Z_L + Z_C \tag{4.9}$$

The circuit in Figure 4-35 is solved by (4.10) and (4.11).

$$2i_{CMi} = i_P + i_N = \frac{2Z_{IN}Z_{LDM}(Z_{NG} + Z_{PG}) + 4(Z_{IN} + 2Z_{LDM})Z_{NG}Z_{PG}}{F_o} \cdot I_{SCM} + \frac{2Z_{IN}Z_{LDM}(Z_{PG} - Z_{NG})}{F_o} \cdot I_{SDM}$$
$$F_o = 2Z_{LCM}Z_{LDM}(Z_{IN} + Z_{NG} + Z_{PG}) + Z_{IN}(Z_{LCM} + Z_{LDM})(Z_{NG} + Z_{PG}) + 2(2Z_{LDM} + Z_{IN})Z_{NG}Z_{PG} \tag{4.10}$$

$$2i_{DMi} = i_P - i_N = \frac{2Z_{IN}Z_{LCM}(Z_{NG} - Z_{PG})}{F_o} \cdot I_{SCM} + \frac{2Z_{IN}Z_{LCM}(Z_{NG} + Z_{PG}) + 4Z_{IN}Z_{NG}Z_{PG}}{F_o} \cdot I_{SDM}$$
$$F_o = 2Z_{LCM}Z_{LDM}(Z_{IN} + Z_{NG} + Z_{PG}) + Z_{IN}(Z_{LCM} + Z_{LDM})(Z_{NG} + Z_{PG}) + 2(2Z_{LDM} + Z_{IN})Z_{NG}Z_{PG} \tag{4.11}$$

We can use (4.10) and (4.11) to solve the circuit where the CM and DM chokes are inserted. The necessary and sufficient condition where the CM and DM noise are decoupled is that Z_{PG} is equal to Z_{NG}, which is in accordance with the analysis without chokes. In the SiC inverter setup, this conclusion is verified by two experiments.

The first experiment is performed with balanced impedances. C_{PG} and C_{NG} are two of the same capacitors with large capacitance to ensure that the systems are strictly balanced. In this setup, the input DM noise is measured in two cases: with and without CM choke, as shown in the curves in Figure 4-38 (a). In Figure 4-38 (a), below 2 MHz, the DM noise is independent of the CM chokes. Because the DM noise is free from the CM in the balanced case, in (4.11), given that $Z_{PG} = Z_{NG}$, the left part is zero ($\frac{2Z_{IN}Z_{LCM}(Z_{NG}-Z_{PG})}{F_o}\cdot I_{SCM}=0$) and the right part can be simplified and verified to be free from Z_{LCM} as (4.12). Above 2 MHz, there is some mismatch between the two curves, because above 2 MHz, the CM chokes have distinct DM impedance.

$$\begin{aligned}
&\frac{2Z_{IN}Z_{LCM}(Z_{NG}+Z_{PG})+4Z_{IN}Z_{NG}Z_{PG}}{2Z_{LCM}Z_{LDM}(Z_{IN}+Z_{NG}+Z_{PG})+Z_{IN}(Z_{LCM}+Z_{LDM})(Z_{NG}+Z_{PG})+2(2Z_{LDM}+Z_{IN})Z_{NG}Z_{PG}}\cdot I_{SDM}\\
&=\frac{4Z_{IN}Z_{LCM}Z_{PG}+4Z_{IN}Z^2{}_{PG}}{2Z_{LCM}Z_{LDM}(Z_{IN}+2Z_{PG})+2Z_{IN}(Z_{LCM}+Z_{LDM})Z_{PG}+2(2Z_{LDM}+Z_{IN})Z^2{}_{PG}}\cdot I_{SDM}\\
&=\frac{2Z_{IN}Z_{PG}(Z_{LCM}+Z_{PG})}{(Z_{LCM}+Z_{PG})(Z_{LDM}(Z_{IN}+2Z_{PG})+Z_{IN}Z_{PG})}\cdot I_{SDM}\\
&=\frac{2Z_{IN}Z_{PG}}{(Z_{LDM}(Z_{IN}+2Z_{PG})+Z_{IN}Z_{PG})}\cdot I_{SDM}
\end{aligned} \tag{4.12}$$

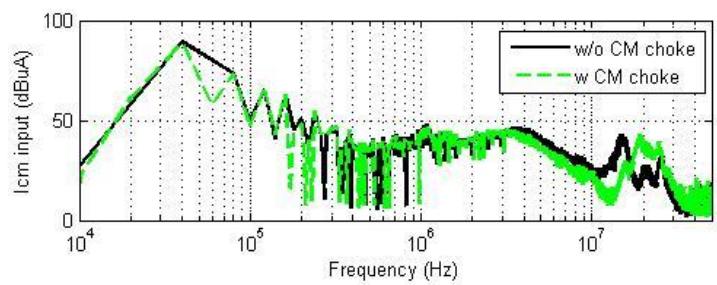

(a)

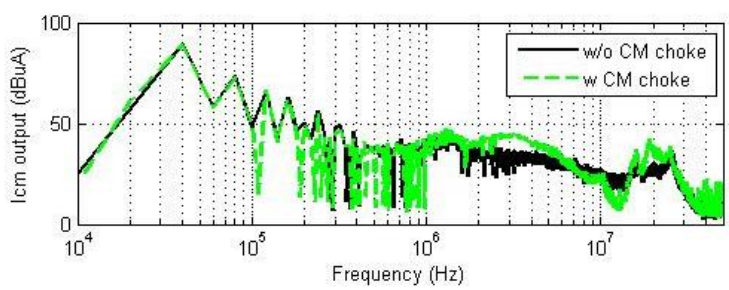

(b)

Figure 4-38 DM spectrum in cases with and without CM choke (a): balanced impedances, (b): unbalanced impedances

The second experiment is performed with unbalanced C_{PG} and C_{NG}. The DM noise in the with-choke and without-choke cases is compared in Figure 4-38 (b). In the unbalanced case, the two curves show obvious difference from 1 MHz to 6 MHz, illustrating that the CM choke has an effect on the DM noise. In this case, the DM noise prediction should consider the CM noise sources and CM propagation path (or CM impedance Z_{LCM}).

The DM terminated behavioral model is the simplified model of this MM terminated behavioral model, where it satisfies $Z_{PG} = Z_{NG}$. Once the assumption $Z_{PG} = Z_{NG}$ fails, the DM terminated behavioral model loses its accuracy.

4.6 DM noise prediction with mixed CM noise

4.6.1 Mix mode terminated behavioral model extraction procedure

The objective of the MM model extraction is to figure out the two equivalent noise sources I_{SDM}, I_{SCM} and three impedances Z_{PG}, Z_{NG} and Z_{IN} using in-circuit experiments as illustrated in Figure 4-34.

Before we get to the noise source extraction, it should be emphasized that here there are two noise sources involving the same phase-aligned problem in the unterminated behavioral model. Only the two noise sources should have aligned phases, and we can calculate i_{CMi} and i_{DMi} as shown in (4.4) and (4.5).

Only one experiment, called 'Balanced Case' is required for the two noise source extractions, illustrated in Figure 4-39. In the 'Balanced Case', there are two extra capacitors connected from Terminal P to G, Terminal N to G. The two capacitors are almost the same, with larger capacitance than the original C_{PG} or C_{NG}. As a result, no matter whether the original circuit is balanced or not, the 'Balanced case' has decoupled CM and DM noise. The relationship between the noises and the noise sources are described in (4.12). In (4.12), Z_{PG} and Z_{IN} can be measured at power-off condition with the same procedure used in the UBM extraction. Z_{LCM} and Z_{LDM} are the CM and DM impedances of the input sides, and can be measured with the impedance analyzer. Due to the fact that DC link capacitance is much larger than C_{PG} or C_{NG}, the DM equation can be further simplified. In addition, the DM equation in (4.12) is equivalent to that in the DM terminated model, if we change the current noise I_{SDM} in to the voltage source $I_{SDM} * Z_{IN}$ according to Thevenin circuit.

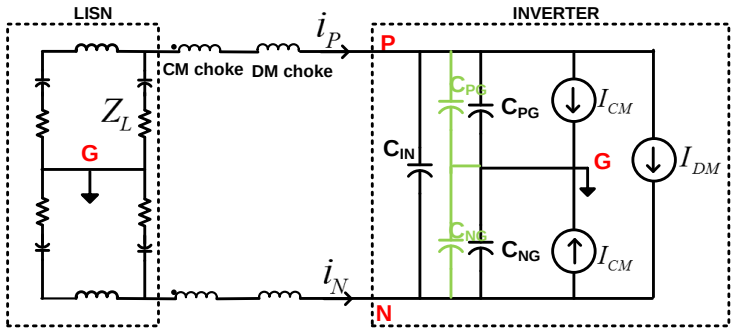

Figure 4-39 Balanced Case: Equivalent noise source extraction in the mix mode model with extra capacitor from the inverter to CM ground

$$
\begin{aligned}
I_{SCM} &= i_{CMi}\frac{Z_{PG}+Z_{LCM}}{Z_{PG}} \\
I_{SDM} &= i_{DMi}\frac{Z_{IN}\parallel(2Z_{PG})+2Z_{LDM}}{Z_{IN}\parallel(2Z_{PG})} \approx i_{DMi}\frac{Z_{IN}+2Z_{LDM}}{Z_{IN}}
\end{aligned}
\tag{4.13}
$$

In the experiment in the 'Balanced Case', i_{CMi} and i_{DMi} are measured simultaneously to ensure that i_{CMi} and i_{DMi} are phase-aligned. Then I_{SCM} and I_{SDM} can be calculated by (4.12) with aligned phase.

In order to have the full spectrum of i_{CMi} and i_{DMi}, it is better to have CM and DM chokes between the inverter and LISN so that the i_{CMi} and i_{DMi} are attenuated to push the noise floor above 30 MHz due to the large impedance of chokes.

As for the impedances, Z_{PG}, Z_{NG} and Z_{IN} use the impedance analyzer to provide measurements one by one. However, for the case where Z_{PG} and Z_{NG} are close to each other, it is hard for the impedance analyzer or the network analyzer find the difference between the two and provide an accurate measurement. Section 4.7 will focus on and develop this issue.

4.6.2 Mix mode model verification

In the SiC inverter, the mixed mode terminated behavioral model is extracted and one more experiment is carried out to validate the model.

In order to acquire the equivalent sources, two 0.47 μF capacitors are fixed from Terminal P and N to G separately. Because the original C_{PG} and C_{NG} have capacitance around 10nF, the total C_{PG} or C_{NG} is almost 0.47 μF with the two extra capacitors. As a result, the inverter system is a strictly balanced and symmetric system no matter whether the original inverter is balanced or not. Then i_{CMi} and i_{DMi} are measured in the case with CM and DM chokes, and the sources are calculated with the measured noise and impedance according to (4.13). The equivalent CM and DM noise sources are illustrated in Figure 4-40.

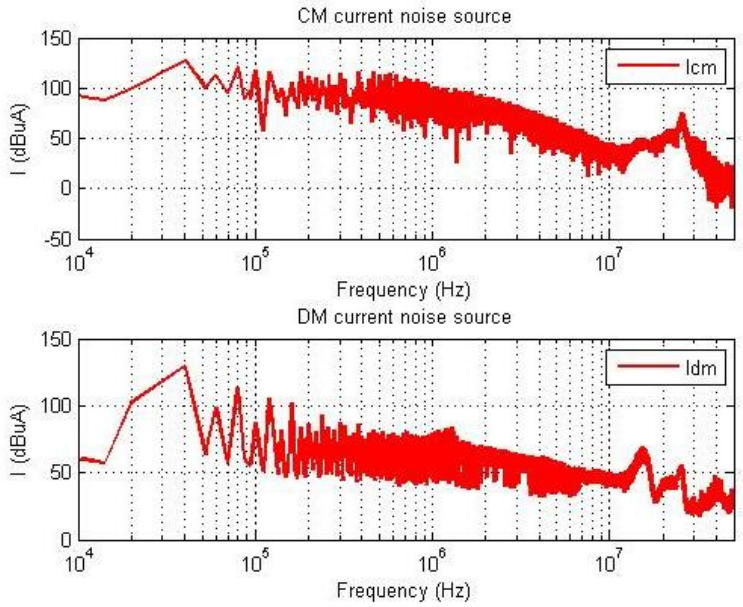

Figure 4-40 Extracted noise sources of the mix mode model

In measuring the inverter impedances, Z_{IN}, Z_{IN} can be measured from Terminal P to N by the impedance analyzer, as shown in Figure 4-41, whose measurement result is illustrated as the blue curve in Figure 4-42.

As for Z_{PG} and Z_{NG}, they are hard to measure directly using the impedance analyzer. Generally, C_{IN} is much larger than C_{PG} and C_{NG} (or $Z_{IN} << Z_{PG}$ and Z_{NG}), contributing a near short-circuit between P and N. As a result, the measurement from Terminal P to G is not Z_{PG}, but rather the paralleled impedance of Z_{PG} and Z_{NG}, which is also equal to the measurement result from Terminal N to G. This problem is further solved in Section 4.7.

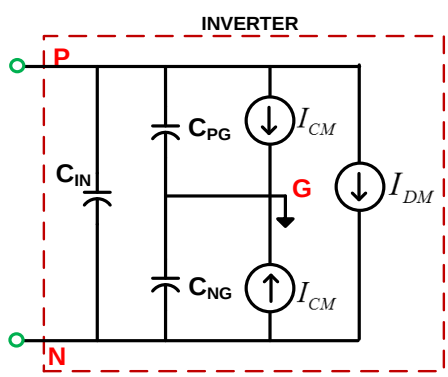

Figure 4-41 Impedance measurement in MM model

However, in this section we need to extract one MM model to see whether the model is effective. In order to do so, we need to create a new unbalanced inverter system. First we insert one 0.47 μF capacitor from Terminal P to N, and measured from P to N. The measurement result here is the total impedance of the 0.47 μF capacitor in parallel with the original C_{PG} and C_{NG}. Due

to the small capacitance of the original C_{PG} and C_{NG} (around 10 nF), the measurement can be seen as the impedance from P to N, and its result is shown as the green curve in Figure 4-42. As for Z_{NG}, another 2 μF capacitor is fixed from N to G. Following the same concept as with Z_{PG}, the measurement from N to G can be seen as the real Z_{NG}, shown as the black curve in Figure 4-42. Consequently, we have an unbalanced system, whose impedances are measured clearly in Figure 4-42.

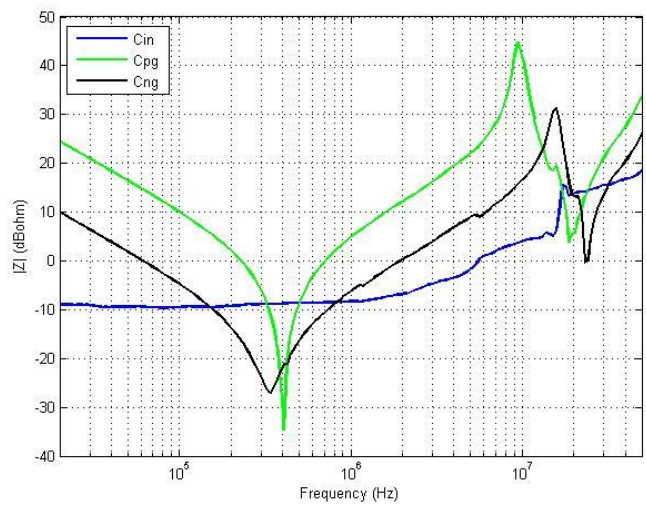

Figure 4-42 Impedance measurement result in MM model with Cpg = 0.47uF, Cng = 2uF

With the extracted noise source and the measured impedances, the DM noise for different cases can be calculated according to (4.11). Cases like the CM, or DM, or CM and DM chokes inserted are performed in the new unbalanced case. The comparison between the measurements and the MM model prediction are shown in Figure 4-44, Figure 4-46, and Figure 4-48. The predictions match the measurement almost to 30 MHz, which validates the model to be an effective tool to predict DM noise in an asymmetric system.

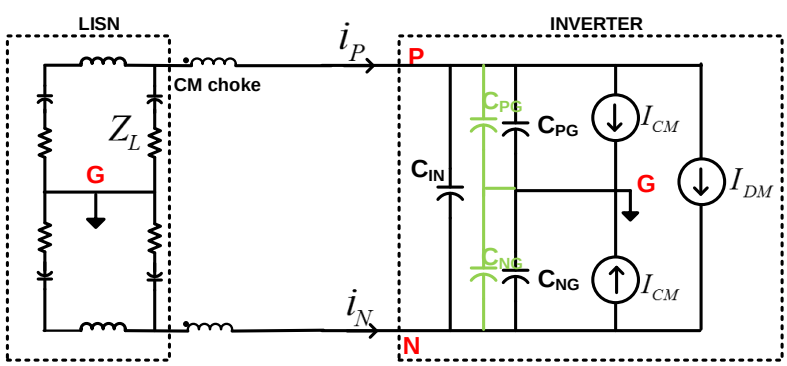

Figure 4-43 Diagram of the new unbalanced inverter with CM choke with Cpg = 0.47uF, Cng = 2uF

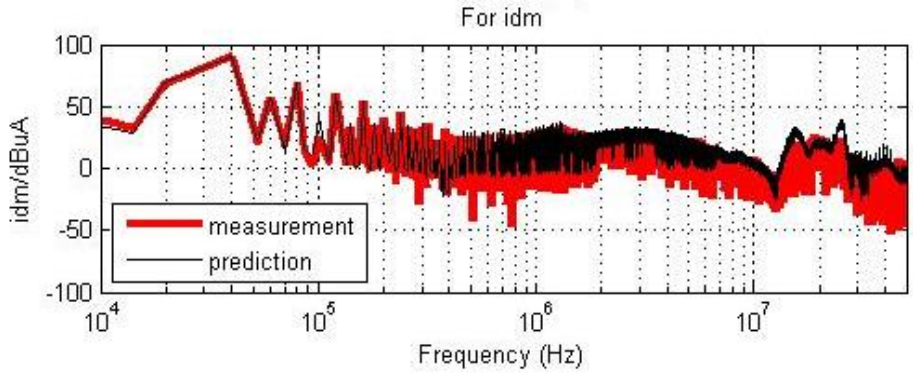

Figure 4-44 Comparison between the measurement of the case in Figure 4-43 and its prediction in MM model

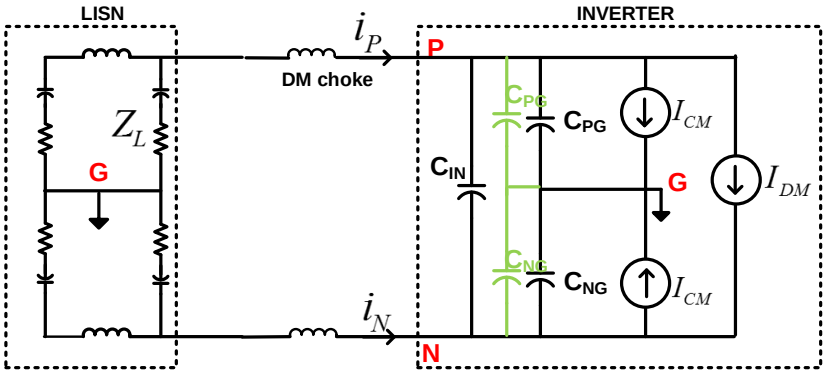

Figure 4-45 Diagram of the new unbalanced inverter with DM choke with Cpg = 0.47uF, Cng = 2uF

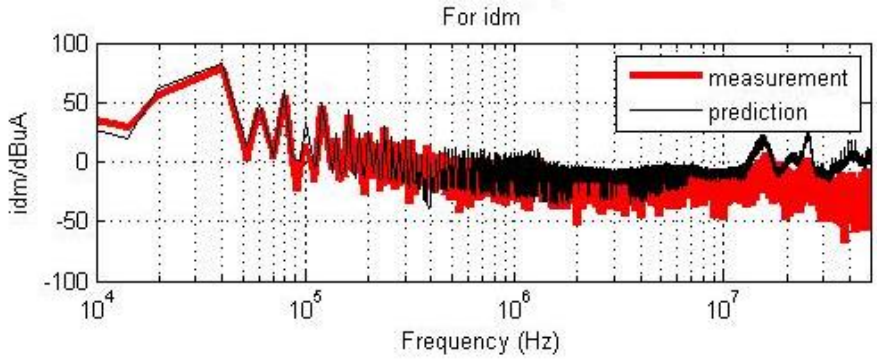

Figure 4-46 Comparison between the measurement of the case in Figure 4-45 and its prediction in MM model

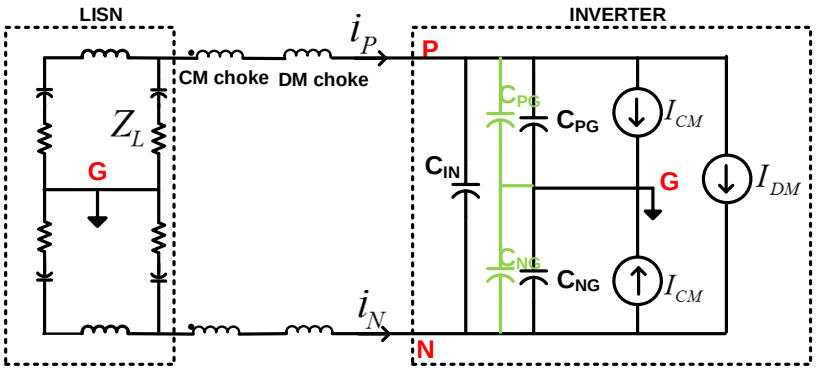

Figure 4-47 Diagram of the new unbalanced inverter with CM and DM choke with Cpg = 0.47uF, Cng = 2uF

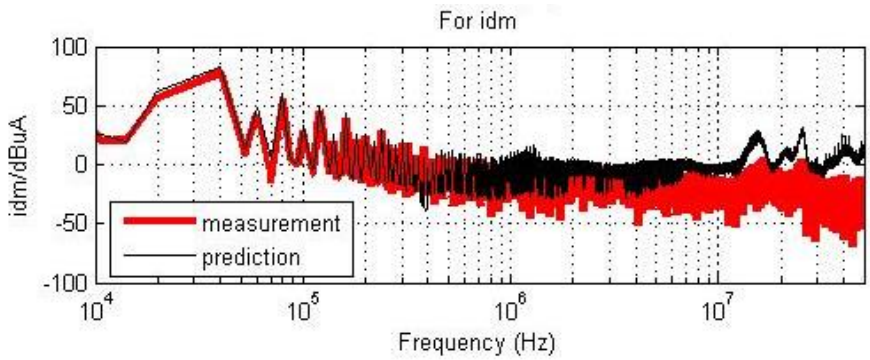

Figure 4-48 Comparison between the measurement of the case in Figure 4-47 and its prediction in MM model

4.7 Evaluation of the proposed mix-mode model

4.7.1 Issue: Unmeasurable parasitic capacitance from inverter to CM ground

When the MM model is applied to an unknown system, the propagation impedances Z_{IN}, Z_{PG}, and Z_{NG} are first measured with an impedance analyzer without connection to the input source or LISN at power-off condition. Theoretically, Z_{PG} is measured between Terminal P and N. But Z_{PG}, or Z_{NG}, usually cannot be measured directly from Terminal P to G. Instead, the measurement result is the total impedance of Z_{PG} and Z_{NG} in parallel. Generally, C_{IN} is much larger than C_{PG} and C_{NG}, and therefore Z_{IN} is much smaller than Z_{PG} and Z_{NG}, contributing a near short-circuit between P and N at the high frequency range.

An effective solution is needed here get the real Z_{PG}, and Z_{NG}, in order to have the full MM model.

4.7.2 Developer

In the UBM extraction, in the second step, a curve-fitting optimization is performed because we are not sure what the real inverter impedances Z_{11}, Z_{12}, and Z_{22} are. This method is verified to be an effective way to find the unknown parameters.

Here we find a similar problem: we do not know what the real Z_{PG}, and Z_{NG} are. The curve-fitting optimization is performed again to find the unknown parameters. In the optimization, the optimized variable is Z_{PG}, whose impedance is represented by a resistor R, an inductor L, and a capacitor C, connected in series. Z_{NG} is calculated according to (4.14), where Z_{PNG} is the impedance measurement from Terminal P (N) to G. The objective function of the method is to minimize the error between the measurement and the prediction, as expressed in (4.15), where $|i_{DM_m}|$ is the measured spectrum magnitude of one case, and $|i_{DM_p}|$ is the predicted spectrum magnitude of the case.

$$Z_{NG} = 1/(\frac{1}{Z_{PNG}} - \frac{1}{Z_{PG}}) \tag{4.14}$$

$$E = \sum_{10kHz}^{10MHz} (|i_{DM_p}| - |i_{DM_m}|)^2 \tag{4.15}$$

As the result of optimization, the optimized Z_{PG} is expressed, and is ready to be applied in the MM model.

Before the application, we can first validate this method and ensure it can give the close value of the real Z_{PG}, and Z_{NG} by using it in the '$C_{PG} = 0.47\mu F, C_{NG} = 2\mu F$' inverter setup. If the optimization can provide a close estimation of Z_{PG}, and Z_{NG}, whose impedances are shown in Figure 4-42, we can trust the optimization.

The noise sources for this validation use the results shown in Figure 4-40. Measure Z_{PNG} of the '$C_{PG} = 0.47\mu F, C_{NG} = 2\mu F$' case. Measure the DM input current i_{DM_m} of the case shown in Figure 4-49. Perform the optimization by using (4.11) to calculate i_{DM_p} in every iteration. The final optimized results of Z_{PG}, and Z_{NG} are shown as the black curves in Figure 4-50, where the optimized Z_{PG} and Z_{NG} are quite close to the measurements. In conclusion, the curve-fitting optimization is an effective way to find the real Z_{PG}, and Z_{NG}.

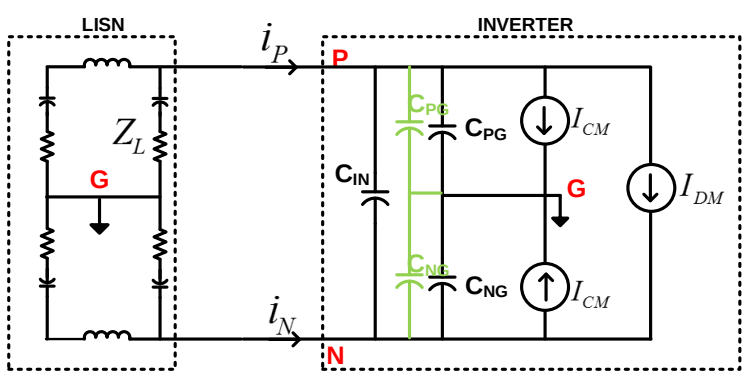

Figure 4-49 Diagram of the new unbalanced inverter without CM or DM choke with Cpg = 0.47uF, Cng = 2uF

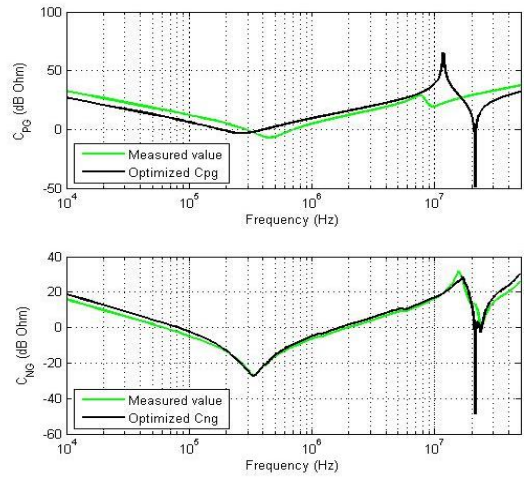

Figure 4-50 The comparison between the optimized Zpg , Zng and the measurements

We can use the optimized Z_{PG}, and Z_{NG} to perform the prediction again for cases in Figure 4-44, Figure 4-46, and Figure 4-48. The predictions of the three cases match their measurements to almost 30 MHz. The optimized impedances are accurate enough for the model, even though they are not the real impedances.

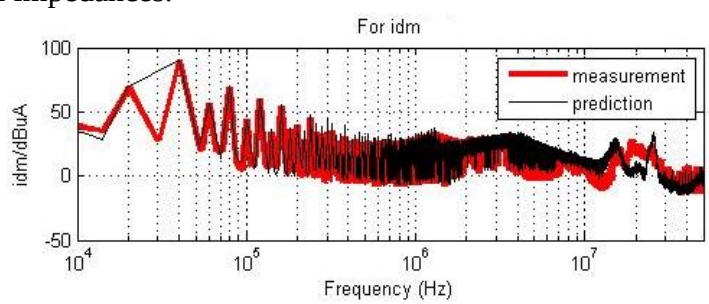

Figure 4-51 Comparison between the measurement of the case in Figure 4-43 and its prediction in MM model with the optimized Z_{pg} and Z_{ng}

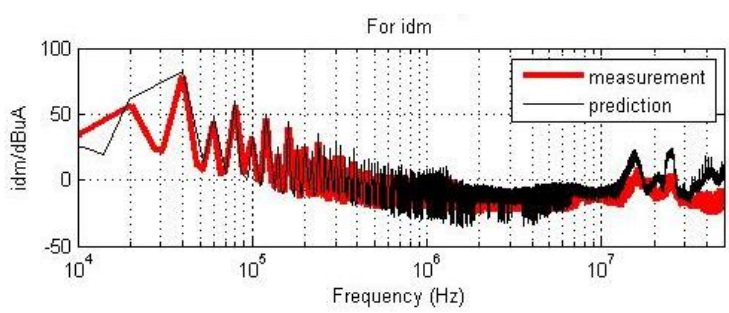

Figure 4-52 Comparison between the measurement of the case in Figure 4-45 and its prediction in MM model with the optimized Z_{pg} and Z_{ng}

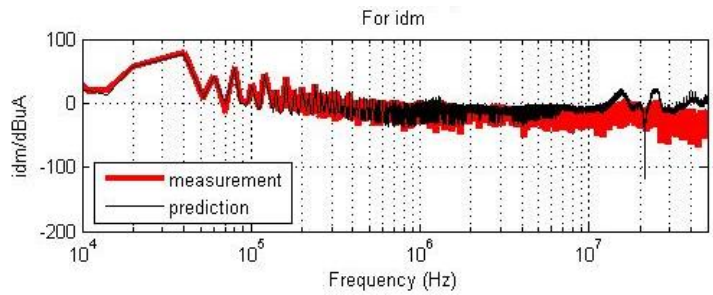

Figure 4-53 Comparison between the measurement of the case in Figure 4-47 and its prediction in MM model with the optimized Z_{pg} and Z_{ng}

4.7.3 DM noise prediction with unmeasurable parasitic capacitance

Above all, the MM model is proposed to predict the DM input noise, and the problem of the unmeasured impedances of Z_{PG}, and Z_{NG} are solved by the curve-fitting optimization. Both the model and the issue developer have been verified to be accurate and helpful. Finally the input DM noises of the SiC inverter setup are ready to predict.

First, the equivalent noise sources are extracted as Figure 4-40 shows. The optimized Z_{PG}, and Z_{NG} are shown in Figure 4-54. The upper two figures show the comparison between the initial value and the optimized results. The lower figure shows that the comparison between the optimized Z_{PG} and Z_{NG} and the two impedances are not equal to each other, resulting in the mixture between the CM and DM noise.

With the optimized impedances, the input DM noises are predicted for the following cases: without CM or DM chokes, with DM chokes, and with CM and DM chokes on the original SiC inverter setup. All the predictions show a good match with the measurement to almost 30 MHz.

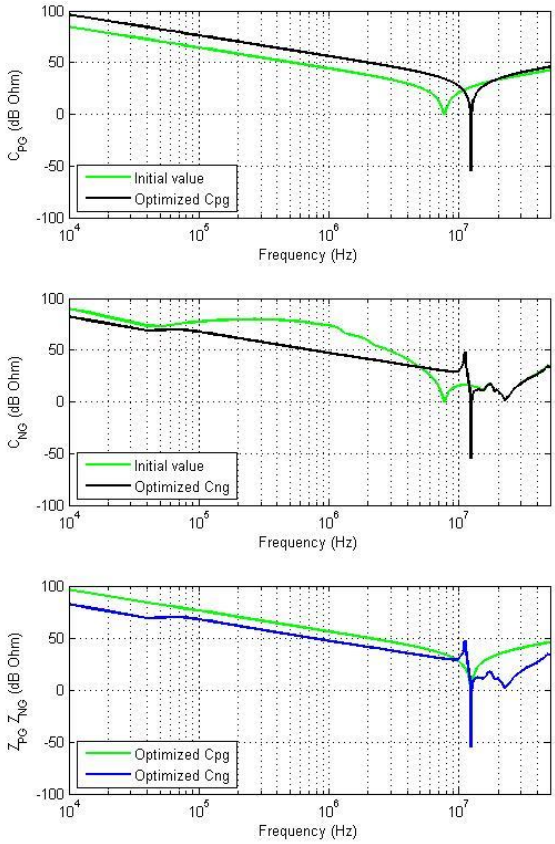

Figure 4-54 Comparison between the initial value and optimized results of C_{pg} and C_{ng}

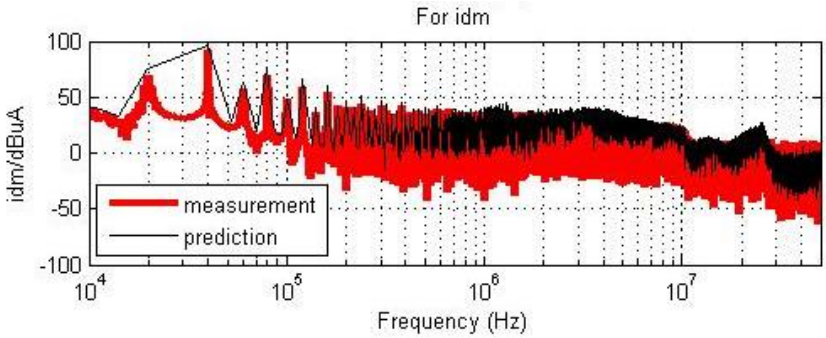

Figure 4-55 Comparison between the measurement and the prediction of the case without chokes in the original SiC inverter setup

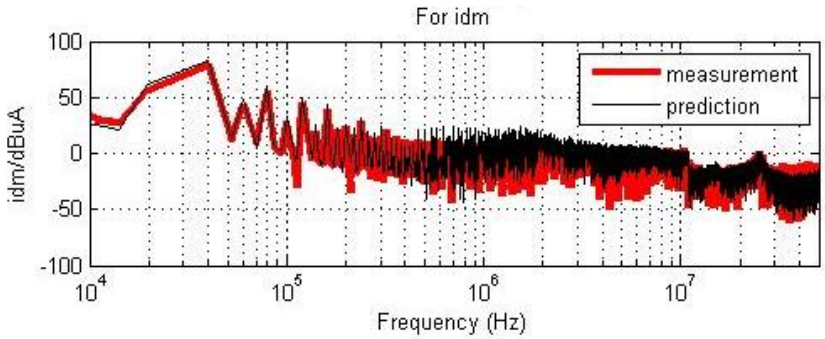

Figure 4-56 Comparison between the measurement and the prediction of the case with CM and DM chokes in the original SiC inverter setup

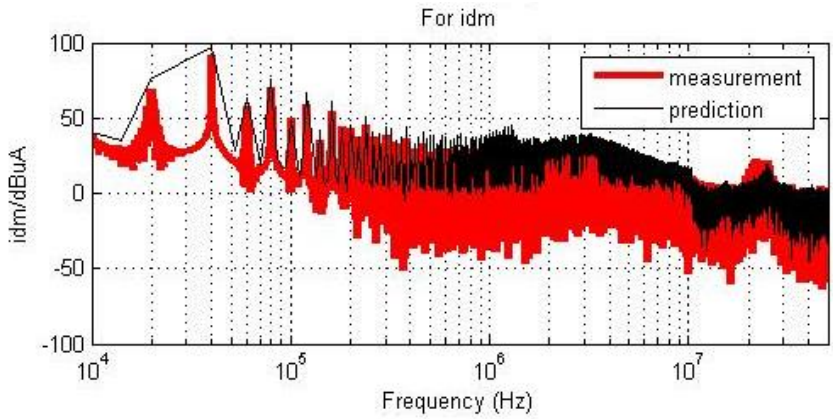

Figure 4-57 Comparison between the measurement and the prediction of the case with DM chokes in the original SiC inverter setup

4.8 Conclusions

In this chapter, the system noise distribution and relationships are analyzed. The DM output is decoupled from the CM noise and input DM noise. The DM input is always influenced by the CM input noise.

The DM output noise is finally predicted with the DM terminated behavioral model to 30 MHz by improving the DM choke and the noise floor issue.

As for the DM input side, a MM model is proposed to predict the DM input noise considering the mixed CM noise, which is caused by the asymmetric capacitors from the DC bus to the CM ground. The model is first verified on a ‘ $C_{PG} = 0.47\mu F, C_{NG} = 2\mu F$ ’ case, whose prediction matches the measurement to almost 30 MHz. Then the curve-fitting optimization is performed, helping find the real Z_{PG} , and Z_{NG} , as they cannot be directly measured by the impedance analyzer. Overall, the DM input noise of the original setup is predicted with the MM model, which agrees with the measurements to alsmot 30 MHz.

In conclusion, the DM input and output noise of the SiC inverter are fully predicted to 30 MHz with the DM terminated behavioral model and the MM model.

Chapter 5 . Summary and Future Work

In the thesis, the CM and DM EMI behavioral models are shown to have a wide frequency of applicability in EMI noise prediction of the SiC power inverter under the high switching frequency. It has been shown, with the improved high frequency UBM, that the CM noise can be captured from 10 kHz to 30 MHz. The DM terminated behavioral model can predict the DM noise to 30 MHz when the CM noise is decoupled from the DM. With the mixed mode model, the DM noise can be predicted in agreement with the measurements to 30 MHz with coupled CM noise. Such models can facilitate the EMI filter design at very high frequency at the system level.

5.1 Summary

This thesis has made significant improvements over existing behavioral EMI modeling techniques. The following are the specific contributions of this thesis:

- Assessed the switching frequency effect on the conducted EMI noise based on a three-phase SiC power inverter. Findings show that with higher switching frequency, both the CM and DM noise will be higher at the conducted EMI noise range.
- Developed a segment-frequency-range measurement to push the noise floor above 30 MHz. The noise floor is the smallest signal the oscilloscope can capture in a vertical scale, which is limited by the vertical resolution of the scope. With 5 MHz and 10 MHz high-pass filter, one spectrum is composed of three parts from the original and two high-pass filter measurements. With the segmented-frequency-range measurement, the noise floor is shifted to 30 MHz. As a result, the UBM prediction capability is further pushed to a high frequency of around 20 MHz.
- Designed sufficiently large impedance for the choke case by putting more chokes in series.
- Designed sufficiently small impedance for the shunt case by reducing the shunt PCB board ESL and applying the thick copper fixture to measure impedances. This is an effective way to decrease the shunt impedance by reducing the measurement fixture ESL, as the fixture ESL is included in the shunt impedance.
- Proposed the high frequency UBM to capture the high frequency CM noise to 30 MHz. With the high frequency UBM, the CM input and output noise of the SiC inverter can be predicted simultaneously, which matches the measurement from 10 kHz to 30 MHz.
- Proposed the high frequency DM terminated model with mixed CM noise. It is found that CM and DM noise will influence each other when the system impedances are not symmetric. The CM noise source will also generate DM noise and the DM noise will be influenced by the CM propagation path impedance. With the mixed mode model, the DM input noise of the SiC inverter is predicted and the prediction matches the measurement to almost 30 MHz.

- Applied the curve-fitting optimization to find the real impedance between the inverter and CM ground. It is verified on the SiC inverter that the curve-fitting is an effective method to find the impedance between the positive terminal to the CM ground, where the result is close to the real impedance. With the optimized impedance, the mixed mode model can still have a 30 MHz prediction capability.

5.2 Limitation

The high frequency EMI behavioral models proposed in the thesis aim to predict the CM and DM noise of the inverter setup, which is an approximately symmetric structure. This required verification of the model when the model is applied to other topologies. In addition, there are other limitations or shortages of the proposed method and model.

5.2.1 Local optimization results in the curve-fitting optimization

The curve-fitting optimization is applied in the UBM and MM model to find a close estimation of the unmeasurable impedance. The optimization is executed in Matlab with its optimization function 'fminsearch.' There are several optimization algorithm presets in Matlab; 'fminsearch' is the only one that can handle the multi-optimized-factor. 'Fminsearch' can only give the local optimization result due to its algorithm. This means that the results of 'fminsearch' are not the best of all the choices and the results are strongly dependent on the initial value. If the initial value happens to be close to the global solution, 'fminsearch' can output the local optimizer as the global optimizer. However, if the initial values are far from the global value, the result of 'fminsearch' is not very good. More trials with different initial values should be done to ensure that the local optimizer is the global result, a process that is very time-consuming.

5.2.2 Insignificant DM effect on the CM noise

In the extraction of the UBM, one of the assumptions of the mode itself is that there is insignificant DM noise effect on the CM noise. As a result, the model can't predict with confidence the CM noise when the CM noise changes due to changing DM noise. In the experimental setup, it is found that there are obvious effects from CM noise on the DM but only minor changes in the CM when DM changes. The UBM needs validation on the case with different DM noise.

The model needs to consider the effect from DM if it cannot predict the CM noise accurately when the DM changes.

5.2.3 No effective CM models for asymmetric structure

Similarly to the second limitation, the UBM may lose its accuracy when it applies to an asymmetric structure topology, where the CM and DM are coupled definitely.

5.3 Future work

Based on the existing work, there are several interesting and meaningful future works that deserve exploration.

5.3.1 Application of the mixed mode model in the asymmetric converter

The MM model is proposed to predict DM input noise for the inverter setup where impedances are not symmetric, and prediction capability is verified to be around 30 MHz. It is possible that this model can be applied on the asymmetric topology converter like buck, boost, flyback. In these converters, the CM and DM should be strongly coupled due to asymmetry. Conducting a trial to see whether the MM model can predict DM noise for these converters would be a worthwhile endeavor.

5.3.2 EMI filter modeling

The objective of this work is to predict the CM and DM input and output EMI noise of the inverter setup. However, the final target of the modeling should be to develop an effective method to design a CM and DM EMI filter.

The designed filter will not work with an improper filter model even if the converter model is good. In the EMI filter, the capacitors can be expressed as several impedance combinations. However, the inductors are not easy to simulate, as it is hard to capture their nonlinear characteristics with simple equations. There will be obvious error if we only consider the DC inductance, EPR and EPC. EPC of the inductor is also hard to define because it is dependent on the fabrication of the inductor by hand.

In conclusion, the EMI modeling of the power converter can be fully utilized only when the EMI filter has the same prediction capability as the filter impedance.

5.3.3 Effect of the switching speed on the EMI emission

Generally, the final aim of the EMI modeling is to help with EMI filter design, which will attenuate the conducted EMI noise below some standard; it is considered from the view of obstructing noise propagation. The noise can also be attenuated when the noise sources are smaller.

The noise sources usually come from the switching behavior of the switches. Usually, the noise source will be larger if the switches turn on and off faster, which requires verification. We can find an effective way to control the noise sources by some active gate controls once we find the relationship between the EMI noise and the switching speed. If the noise sources are attenuated by the switching speed control, the EMI filter will possibly have smaller volume due to the smaller attenuation ratio.

Further work can also explore how to find a good tradeoff between the EMI noise and switching loss by adjusting the switching speed.

References

[1]. A. C. Baisden, D. Boroyevich, and J. D. van Wyk, "High Frequency Modeling of a Converter with an RF-EMI Filter," in Industry Applications Conference, 2006. 41st IAS Annual Meeting. Conference Record of the 2006 IEEE, 2006, pp. 2290-2295

[2]. Z. Huibin, L. Jih-Sheng, A. R. Hefner, Jr., T. Yuqing, and C. Chingchi, "Analysis of conducted EMI emissions from PWM inverter based on empirical models and comparative experiments," in Proc. IEEE Power Electron. Spec. Conf., 1999, pp. 861-867 vol.2

[3]. M. Moreau, N. Idir, and P. Le Moigne, "Modeling of Conducted EMI in Adjustable Speed Drives," IEEE Trans. Electromagn. Compat., vol. 51, pp. 665-672, 2009

[4]. L. Qian, "Modular Approach for Characterizing and Modeling Conducted EMI Emissions in Power Converters " PhD Dissertation, Electrical and Computer Engineering, Virginia Tech, Blacksburg, 2005

[5]. L. Ran, S. Gokani, J. Clare, K. J. Bradley, and C. Christopoulos, "Conducted electromagnetic emissions in induction motor-drive systems. I. Time domain analysis and identification of dominant modes," IEEE Trans. Power Electron., vol. 13, pp. 757-767, 1998.

[6]. L. Ran, S. Gokani, J. Clare, K. J. Bradley, and C. Christopoulos, "Conducted electromagnetic emissions in induction motor-drive systems. II. Frequency domain models," IEEE Trans. Power Electron., vol. 13, pp. 768-776, 1998.

[7]. P. Xuejun, Z. Kai, K. Yong, and C. Jian, "Analytical estimation of common mode conducted EMI in PWM inverter," in Conf. Rec. IEEE IAS Annu. Meeting, 2004, pp. 2651-2656 vol.4.

[8]. F. Giezendanner, J. Biela, J. W. Kolar, and S. Zudrell-Koch, "EMI Noise Prediction for Electronic Ballasts," IEEE Trans. Power Electron., vol. 25, pp. 2133-2141, 2010.

[9]. E. Hoene, W. John, M. Michel, and H. Reichl, "Evaluation and Prediction of Conducted Electromagnetic Interference Generated by High Power Density Inverters," in Power Electronics and Applications (EPE 2001), Proceedings of the 9th European Conference on, Graz, Austria, 2001, pp. P.1-P.9.

[10]. M. Moreau, N. Idir, P. Le Moigne, and J. J. Franchaud, "Utilization of a behavioural model of motor-drive systems to predict the conducted emissions," in Power Electronics Specialists Conference, 2008. PESC 2008. IEEE, 2008, pp. 4387-4391.

[11]. D. Labrousse, B. Revol, and F. Costa, "Common-Mode Modeling of the Association of N - Switching Cells: Application to an Electric-Vehicle-Drive System," IEEE Trans. Power Electron., vol. 25, pp. 2852-2859, 2010.

[12]. J. Kotny and N. Idir, "Time domain models of the EMI sources in the variable speed drives," in Energy Conversion Congress and Exposition (ECCE), 2010 IEEE, 2010, pp. 1355-1360.

[13]. B. Revol, J. Roudet, J. L. Schanen, and P. Loizelet, "EMI Study of Three-Phase Inverter-Fed Motor-drives," IEEE Trans. Ind. Appl., vol. 47, pp. 223-231, 2011.

[14]. J. Meng and W. Ma, "Power Converter EMI Analysis Including IGBT Nonlinear Switching Transient Model," IEEE Trans. Ind. Electron., vol. 53, pp. 1577-1583, 2006.

[15]. Q. Tao, J. Graham, and S. Jian, "Characterization of IGBT modules for system EMI simulation," in IEEE Appl. Power Electron. Conf. Expo., 2010, pp. 2220-2225.

[16]. X. Lei, F. Feng, and S. Jian, "Behavioral modeling methods for motor-drive system EMI design optimization," in Proc. IEEE ECCE, 2010, pp. 947-954.

[17].C. Henglin, F. Limin, C. Wei, and Q. Zhaoming, "Modeling and measurement of the impedance of common mode noise source of switching converters," in IEEE Appl. Power Electron. Conf. Expo., 2006, p. 4 pp.
[18].Y. Koyama, M. Tanaka, and H. Akagi, "Modeling and Analysis for Simulation of Common-Mode Noises Produced by an Inverter-Driven Air Conditioner," IEEE Trans. Ind. Appl., vol. 47, pp. 2166-2174, 2011.
[19].B. Toure, J. L. Schanen, L. Gerbaud, T. Meynard, and J. P. Carayon, "EMC modeling of drives for aircraft applications: Modeling process, EMI filter optimization and technological choice," in Energy Conversion Congress and Exposition (ECCE), 2011 IEEE, 2011, pp. 1909-1916.
[20].M. F. Moad, "Two-port networks with independent sources," Proc. IEEE, vol. 54, pp. 1008-1009, 1966.
[21].H. A. Haus, W. R. Atkinson, G. M. Branch, W. B. Davenport, W. H. Fonger, W. A. Harris, et al., "Representation of Noise in Linear Twoports," Proc. IRE, vol. 48, pp. 69-74, 1960.
[22].M. Hosoya. (2000) The Simplest Equivalent Circuit of a Multi-Terminal Network. Bulletin of the College of Science - Univ. Ryukyus. 1-10.
[23].M. Hosoya. (2001) The Straightforward Expansion of Helmholtz-Thevenin Theorem to Multi-Terminal Networks. Bulletin of the College of Science - Univ. Ryukyus. 39-45.
[24].F. F. Judd and P. M. Chirlian, "The Application of the Compensation Theorem in the Proof of Thevenin's and Norton's Theorems," IEEE Trans. Educ., vol. 13, pp. 87-88, 1970.
[25].M. F. Moad, "On Thevenin's and Norton's Equivalent Circuits," IEEE Trans. Educ., vol. 25, pp. 99-102, 1982.
[26].L. Ran, J. C. Clare, K. J. Bradley, and C. Christopoulos, "Measurement of conducted electromagnetic emissions in PWM motor-drive systems without the need for an LISN," IEEE Trans. Electromagn. Compat., vol. 41, pp. 50-55, 1999.
[27].F. Costa, C. Vollaire, and R. Meuret, "Modeling of conducted common mode perturbations in variable-speed drive systems," IEEE Trans. Electromagn. Compat., vol. 47, pp. 1012-1021, 2005.
[28].C. Jettanasen, F. Costa, and C. Vollaire, "Common-Mode Emissions Measurements and Simulation in Variable-Speed Drive Systems," IEEE Trans. Power Electron., vol. 24, pp. 2456-2464, 2009.
[29].L. M. Schneider, "Noise Source Equivalent Circuit Model of Off-line Converters and Use in Input Filter Design," in Proc. POWERCON, 1982.
[30].L. Qian, W. Fei, and D. Boroyevich, "Modular-Terminal-Behavioral (MTB) Model for Characterizing Switching Module Conducted EMI Generation in Converter Systems," IEEE Trans. Power Electron., vol. 21, pp. 1804-1814, 2006.
[31].L. Qian, F. Wang, and D. Boroyevich, "Conducted EMI Noise Prediction and Characterization for Multi-phase-leg Converters Based on Modular-Terminal-Behavioral (MTB) Equivalent EMI Noise Source Model," in Power Electronics Specialists Conference, 2006. PESC '06. 37th IEEE, 2006, pp. 1-7.
[32].L. Qian, F. Wang, and D. Boroyevich, "Conducted-EMI Prediction for AC Converter Systems Using an Equivalent Modular Terminal Behavioral (MTB) Source Model," IEEE Trans. Ind. Appl., vol. 43, pp. 1360-1370, 2007.
[33].A. C. Baisden, D. Boroyevich, and F. Wang, "EMI Terminal Modeling," in Conf. Rec. IEEE IAS Annu. Meeting, 2008, pp. 1-8.

[34].A. C. Baisden, "Generalized Terminal Modeling of Electro-Magnetic Interference," PhD Dissertation, Electrical Engineering, Virginia Tech, Blacksburg, VA, 2010.
[35].A. C. Baisden, D. Boroyevich, and W. Fei, "Generalized Terminal Modeling of Electromagnetic Interference," IEEE Trans. Ind. Appl., vol. 46, pp. 2068-2079, 2010.
[36].M. Foissac, J. L. Schanen, and C. Vollaire, ""Black box" EMC model for power electronics converter," in Proc. IEEE ECCE, 2009, pp. 3609-3615.
[37].M. Foissac, J. Schanen, G. Frantz, D. Frey, and C. Vollaire, "System simulation for EMC network analysis," in IEEE Appl. Power Electron. Conf. Expo., 2011, pp. 457-462.
[38].J. Meng, W. Ma, and L. Zhang, "Determination of noise source and impedance for conducted EMI prediction of power converters by lumped circuit models," in Proc. IEEE Power Electron. Spec. Conf., 2004, pp. 3028-3033 Vol.4.
[39].M. Jin, M. Weiming, P. Qijun, Z. Zhihua, and Z. Lei, "Noise Source Lumped Circuit Modeling and Identification for Power Converters," IEEE Trans. Ind. Electron., vol. 53, pp. 1853-1861, 2006.
[40].A. Perez, J. R. Regue, M. Ribo, A. M. Sanchez, F. J. Pajares, and D. Badia, "Circuital Characterization of an Electronic Equipment for Narrow-Band Conducted Emissions," in Proc. EMC Europe Int. Symp., Barcelona, Spain, 2006, pp. 1035–1040
[41].A. Perez, A. M. Sanchez, J. R. Regue, M. Ribo, P. Rodriguez-Cepeda, and F. J. Pajares, "Characterization of Power-Line Filters and Electronic Equipment for Prediction of Conducted Emissions," IEEE Trans. Electromagn. Compat., vol. 50, pp. 577-585, 2008.
[42].H. M. Rebholz and S. Tenbohlen, "Efficient characterization of RF sources for the design of noise suppression filters," in Antennas, Propagation and EM Theory, 2008. ISAPE 2008. 8th International Symposium on, 2008, pp. 929-932.
[43].H. M. Rebholz, S. Tenbohlen, and W. Kohler, "Time-Domain Characterization of RF Sources for the Design of Noise Suppression Filters," IEEE Trans. Electromagn. Compat., vol. 51, pp. 945-952, 2009.
[44].Fang Luo; Boroyevich, D.; Mattavelli, P.; Xuning Zhang, "On discussion of switching frequency impacts on DC-fed motor drive EMI filter design," Applied Power Electronics Conference and Exposition (APEC), 2012 Twenty-Seventh Annual IEEE , vol., no., pp.623,627, 5-9 Feb. 2012
[45].DO-160G, Environmental Conditions and Test Procedures for Airborne Equipment, 7 ed.: Radio Technical Commission for Aeronautics, 2010.
[46].CPES-Project-Report-Oct2012
[47].Bishnoi, H.; Mattavelli, P.; Boroyevich, D., "Unterminated common-mode EMI model of DC-fed motor drives," Power Electronics and Motion Control Conference (EPE/PEMC), 2012 15th International , vol., no., pp.DS2a.15-1,DS2a.15-8, 4-6 Sept. 2012
[48].Bishnoi, H.; Mattavelli, P.; Burgos, R.; Boroyevich, D., "EMI terminal modelling of dc-fed motor drives," Power Electronics and Applications (EPE), 2013 15th European Conference on , vol., no., pp.1,10, 2-6 Sept. 2013
[49].Bishnoi, H., “Behavioral EMI-Models of Switched Power Converters,” Ph.D. dissertation, ECE. Dept., Virginia Tech., Blacksburg, VA, 2013.
[50].Oscilloscope manual guide RTO_bro_en_5214-2327-12_v1300
[51].RTO_dat-sw_en_5214-5155-22_v1500
[52].Meng Jin; Ma Weiming, "A new technique for modeling and analysis of mixed-mode conducted EMI noise," Power Electronics, IEEE Transactions on , vol.19, no.6, pp.1679,1687, Nov. 2004

[53].Jing Xue; Wang, F., "Mixed-mode EMI noise in three-phase DC-fed PWM motor drive system," Energy Conversion Congress and Exposition (ECCE), 2013 IEEE , vol., no., pp.4312,4317, 15-19 Sept. 2013